https://doi.org/10.15388/vu.thesis.235
https://orcid.org/0000-0002-3165-9823

VILNIUS UNIVERSITY
CENTER FOR PHYSICAL SCIENCES AND TECHNOLOGY

Saulius
PAKALKA

Theoretical study of direct and indirect single ionisation by electron impact

DOCTORAL DISSERTATION
Nature Science,
Physics (N 002)

VILNIUS 2021

Doctoral Dissertation was completed during 2016-2020 at Vilnius University, Institute of Theoretical Physics and Astronomy.

Scientific supervisor - doc. dr. Valdas Jonauskas (Vilnius University, Nature Science, Physics – N 002).

https://doi.org/10.15388/vu.thesis.235
https://orcid.org/0000-0002-3165-9823

VILNIAUS UNIVERSITETAS
FIZINIŲ IR TECHNOLOGIJOS MOKSLŲ CENTRAS

Saulius
PAKALKA

Tiesioginės ir netiesioginės viengubos jonizacijos elektronų smūgiais tyrimas

DAKTARO DISERTACIJA
Gamtos mokslai,
fizika (N 002)

VILNIUS 2021

Daktaro disertacija parengta 2016-2020 Vilniaus universiteto Fizikos fakulteto Teorinės fizikos ir astronomijos institute.

Mokslinis vadovas - doc. dr. Valdas Jonauskas (Vilniaus universitetas, gamtos mokslai, fizika – N 002).

Contents

Publications on the subject of the dissertation

Articles

A1 A. Kynienė, **S. Pakalka**, Š. Masys, and V. Jonauskas, "Electron-impact ionization of W^{25+}," J. Phys. B At. Mol. Opt. Phys., vol. 49, no. 18, p. 185001, Sep. 2016.

A2 A. Kynienė, G. Merkelis, A. Šukys, Š. Masys, **S. Pakalka**, R. Kisielius, V. Jonauskas, "Maxwellian rate coefficients for electron-impact ionization of W^{26+}," J. Phys. B At. Mol. Opt. Phys., vol. 51, no. 15, p. 155202, Aug. 2018.

A3 **S. Pakalka**, S. Kučas, Š. Masys, A. Kynienė, A. Momkauskaitė, and V. Jonauskas, "Electron-impact single ionization of the Se^{3+} ion," Phys. Rev. A, vol. 97, no. 1, p. 012708, Jan. 2018.

A4 A. Kyniene, S. Kučas, **S. Pakalka**, Š. Masys, and V. Jonauskas, "Electron-impact single ionization of Fe^{3+} from the ground and metastable states," Phys. Rev. A, vol. 100, no. 5, pp. 1–10, 2019.

A5 V. Jonauskas, A.Kynienė, S.Kučas, **S.Pakalka**, Š.Masys, A.Prancikevičius, A.Borovik Jr., M.F.Ghareibeh, S.Schippers, A.Müller, "Electron-impact ionization of W^{5+}," Phys. Rev. A, vol. 100, no. 6, pp. 1–12, 2019.

Conference Presentations

- Lithuanian National Physics Conference. Poster presentation: "Electron-impact single ionisation of the Se^{3+} ion", Vilnius, Lithuania,

2017.

- 31^{st} International Conference on Photonic, Electronic and Atomic Collisions (ICPEAC XXXI). Poster presentation: "Inner-shell ionisation of W^{25+}", Deauville, France, 2019.

- 31^{st} International Conference on Photonic, Electronic and Atomic Collisions (ICPEAC XXXI). Poster presentation: "Electron Impact ionisation of Fe^{3+}", Deauville, France, 2019.

Acknowledgements

Throughout the writing of this dissertation, I have received a great deal of support and assistance.

I want to thank my supervisor, Assoc. Prof. Dr. Valdas Jonauskas for his patience and countless hours spent on video calls with me during pandemic. Without his help and advice, this process would have been difficult to complete.

My appreciation goes out to my wife and two daughters for their encouragement and support throughout my studies.

List of the Abbreviations

BEB binary-encounter-Bethe
BED binary encounter dipole
CADW configuration average distorted wave
CE collisional excitation
CI configuration interaction
CIS configuration interaction strength
CSF configuration state function
ECR electron-cyclotron-resonance
EII electron-impact ionisation
DC dielectronic capture
DI direct ionisation
DDI direct double ionisation
DF Dirac-Fock
DFS Dirac-Fock-Slater
DW distorted wave
EA excitation autoionisation
FAC flexible atomic code
GRASP2K General-Purpose Relativistic Atomic Structure package
HF Hartree-Fock
LLDW level-to-level distorted wave
MRC Maxwell rate coefficient
$\mathbf{N}_{CSF}$ number of CSFs
NIST National Institute of Standards and Technology
PWB palne-wave Born
REDA resonant excitation-double autoionisation
SCADW subconfiguration average distorted wave
UTA unresolved transition arrays

INTRODUCTION

The plasma state is often referred to as the fourth state of matter. It might seem strange, but 99.99 % of the visible Universe is in the state of plasma. The Earth and its lower atmosphere are shielded from the charged plasma particles and radiation of solar wind. The outer layers of the Sun and stars, in general, are made up of matter in an ionised state. The ionised state of the interstellar gas is formed from winds of stars and stellar radiation [1].

Any charged gas cannot be called plasma. Plasma is a quasi-neutral gas of charged and neutral particles, which dynamics is driven by electrodynamic forces. Particles of plasma gas exhibits collective behaviour [2]. Positive or negative electrical charge can be gained by atoms and molecules of plasma. This process is called ionisation. Electromagnetic properties of gas appear on the scene at relatively modest degrees of ionisation. Interplanetary space and other cosmic plasmas show a wide range degree of ionisation: from a fraction of a per cent to totally ionised gas [1]. Furthermore, extensive temperature and density ranges that extend over many orders of magnitude can be observed in the plasma. What is more, plasma does not break or disintegrate when heated to extreme temperatures or when strong electromagnetic fields are applied.

Great interest for the development of plasma physics over the second half of the twentieth century came from research into controlled thermonuclear fusion as well as from astrophysical and space plasma phenomena. Starting in the late 1980s, a new application of plasma physics appeared – plasma processing – a critical aspect of the fabrication of the tiny, complex integrated circuits used in modern electronic devices. This application is now of great economic importance [3].

Today plasma is recognized as the vital element to understanding the generation of magnetic fields in planets, stars, and galaxies. These

phenomena occur in stellar atmospheres, in the interstellar and intergalactic media, in radio galaxies and quasars, and inside active galactic nuclei. Also, to some degree, it affects the acceleration and transport of cosmic rays [4]. The chemical composition of these objects can provide significant insight into the nucleosynthetic histories of stellar populations and chemical evolution of galaxies and universe. To derive accurate elemental abundances, ionisations stages of elements in distant objects have to be evaluated.

With the use of ultrahigh power lasers that generate high fluxes of energetic photons, electrons, protons and ions used for the study of nuclear and elementary particle physics applications, new research branches were opened. Furthermore, today, the theoretical and experimental study of the electron-impact ionisation of low charged moderately heavy atomic ions remains a demanding scientific challenge. Addressing the challenge will lead to a better understanding of many low temperature astrophysical and laboratory plasmas.

Recent ultrafast spectroscopy experiments [5, 6] show a need for highly accurate theoretical data about the atom or ion photoionisation. That data covers very accurate energy levels, absorption cross sections, excitation lifetime and Auger decay process paths, and effective lifetime for transitions.

The study of plasma from the atomic physics point of view is interested in three general topics. One of them concentrates on the influence of the plasma environments on the atomic potential, which affects bound electron wave functions and atomic structure. The other topic deals with collisional processes in plasma among particles: electron - ion, ion - ion. The charge and excited states distribution are determined by ionisation and excitation of the ions. The third topic investigates emission and absorption spectra in plasma.

Spectroscopy is one of the most powerful tools for understanding the properties of plasma. Moreover, spectral emission of the plasma can provide information about temperature and density of the emitting environment. However, it is important to understand the underlying atomic physics, that define emission spectra. The intensities of the spectral lines are determined by charge state distribution in the plasma. Electron impact-ionisation and electron-ion recombination processes define the charge state distribution for a plasma in collisional ionisation equilibrium.

There is a high demand for ionisation cross section, Maxwellian rate coefficients, and often only theoretical calculations can provide that data due to limitations of experimental techniques. By using big data tools, it is now possible to overcome the heavy calculations limit. Distributed calculation systems combine multiple hardware resources into a single logical unit and simplify usage for scientific purposes.

To understand astrophysical environments, thermonuclear plasma and its dynamics require reliable atomic data, and electron-ion collisions are among the essential processes in these environments [7]. In this work, a study of single-electron impact ionisation processes involves three different materials: iron, selenium and tungsten. We selected to study the Se^{3+} and Fe^{3+} ions and a group of tungsten ions with different ionisation degrees: W^{5+}, W^{25+} and W^{26+}.

Lines of selenium were observed in the spectra of stars [8, 9] and of astrophysical nebulae [10–12]. Selenium is used in semiconductor manufacturing, and the related properties are investigated quite well. Additionally, selenium is used for the production of glass, solar cells, batteries, etc. Recently, experimental cross sections by electron impact for the Se^{2+} and Se^{3+} ions have been observed for the first time using the dynamic-crossed-beams technique [13, 14]. Previous experimental studies of selenium ions' ionisation have been focused on interaction with photons [15–18].

First theoretical results for electron-impact single- and double-ionisation cross sections for the Se^{2+} and Se^{3+} ions were calculated using a configuration-average distorted-wave (CADW) method [19]. Essential discrepancies among theoretical and experimental cross sections for single ionisation of Se^{3+} have been obtained for lower and higher energies of the collisional electron. Later, cross sections were investigated using the level-to-level distorted-wave (LLDW) method for the ground and excited configurations [20], having an aim to explain the obtained discrepancies in the CADW calculations. Their study determined that the excited $[Ar]3d^{10}4s^24d$ configuration with 15 % of population was present in the ion beam. One of the recent theoretical works related to double- and triple-ionisation of Se^{2+} and Se^{3+} was done by Koncevičiūtė *at al.* [21, 22]. They studied the electron-impact triple ionisation process of the Se^{2+} ion by considering the Auger cascade, following the creation of the inner shell vacancy and the direct double-ionisation process with subsequent autoion-

isation. In addition, double- and triple-ionisation processes for the Se^{3+} ion were studied by performing level-to-level calculations: the influence of ionisation-autoionisation (IA), excitation double-autoionisation (EDA), DDI, and resonant- excitation triple-autoionisation (RETA) processes to DI were analysed. The provided results showed the importance to consider combination of several different processes affecting final ionisation cross sections results.

Certainly iron is widely used in numerous sectors such as electronics, construction, building, manufacturing and automotive. It is the most abundant element in Earth's core. Bright iron lines are observed in spectra of astronomical objects. Moreover, iron lines account for about 30 % of the lines in the solar spectrum. The iron ions are present as impurities in tokamak plasma. Furthermore, emissions from impurities remove energy from plasma and thus reduce the fusion field. It is important to control amount of impurities in the plasma of the thermonuclear reactors.

The configuration average distortion wave approximation was used to analyse electron impact ionisation cross sections in Fe^{3+} [23]. The cross sections for $3p \rightarrow 3d$ excitation with subsequent autoionisation were studied in their work.

The experimental cross sections for the Fe^{3+} ion were observed by employing the animated crossed-beams technique [24]. It is important to note that, other excitation-autoionisation (EA) channels corresponding to excitations to the higher shells were not considered in these calculations [23, 25].

The onset of cross sections below the single ionisation threshold demonstrated the presence of metastable fraction in the ion beam. It was suggested that contribution from the levels of the ground configuration can be associated with the metastable fraction. However, the influence of the metastable ions to the measured cross sections was not investigated previously.

The first measurements for single ionisation by electron impact of W^+ were presented by Montague and Harrison [26] using the crossed ion and electron beams technique. In addition, tungsten ions are other important impurity in plasma of tokamak devices. Tungsten, due to its low sputtering rate, is planned to be used in future large fusion devices such as ITER and DEMOnstration power plant [27–29]. However, some tungsten ions manage to reach central regions of reactor and their radi-

ation threatens to terminate the ignition reaction. Modelling in formation of spectral lines in tokamak plasma is required to determine charge state distribution. Stenke *et al.* [30] provided data for the tungsten ions from W^+ to W^{10+}. It should be noted that the measurements demonstrated the presence of the metastable fraction in ion beam. The Lotz formula [31] was used to compare with measurements. The theoretical cross sections were ∼40 % below the experimental data for the values. The difference can be explained by the missing EA contribution.

The experimental data showed good agreement with the CADW calculations [32]. These calculations determined the single ionisation cross sections for the direct and indirect processes in W^{4+}, W^{5+} and W^{6+}. However, contributions from the metastable levels of the ions to the single ionisation cross sections were not investigated.

The CADW calculations were extended for the tungsten ions in all charge states up to 73. A statistical model, based on the idea of collective excitations of atomic electrons with the local plasma frequency, was employed by Demura *et al.* [33] for tungsten ions up to W^{63+}. The Thomas-Fermi model is used to describe electron-density distribution in their calculations. However, this approach did not provide good agreement with measurements for many ions. It should be noted that this approach may be successfully used for a first estimate of cross sections over a wide range of ions. The detailed LLDW calculations of the single ionisation cross sections have been carried out for the W^{5+} ion [34]. Nonetheless, these calculations were missing contributions from the metastable fraction. It was noticed that excitations to higher shells ($n > 8$) led to overestimated values compared to the measurements. The reason of the discrepancy between theoretical data and experimental values was not identified.

It is well known that DW approach often provides overestimated values of cross sections for neutral atoms and near neutral ions. Previously, the binary-encounter-dipole (BED) and binary-encounter-Bethe (BEB) models were developed for the direct process to determine cross sections for these ionisation stages [35]. The scaled plane-wave-Born cross sections were introduced to deal with excitation process [36]. This led to good agreement with experimental data [37, 38]. The BEB model was used previously to analyze electron impact cross sections for the neutral W and the W^+ ion [39]. Later, the same ions were investigated using the Coulomb-Born method with exchange and normalisation [40]. Kwon

et al. [41] used the FAC [42] for W^+ ion by performing the LLDW calculations. The R-matrix method was employed to study EA in addition to collisional ionisation [43].

The Main Goal of this Work

This work aims to study the electron-impact single ionisation process using the DW approach and suggests accurate and effective methods to provide theoretical cross sections.

The Main Tasks of the Thesis

1. Expansion of programs to calculate single ionisation cross sections:
    - program to calculate autoionisation branching ratios for levels;
    - program to calculate cross sections for excitation autoionisation process.
2. Investigation of direct single ionisation processes:
    - study of collisional ionisation by electron impact using the DW approach;
    - study of collisional ionisation cross sections in the potentials of ionising and ionised ions;
    - study of the influence of electron-impact DDI process on the single direct ionisation cross sections.
3. Investigation of indirect single ionisation processes:
    - study of convergence for the EA cross sections;
    - study of excitations to subshells with different orbital quantum numbers;
    - study of the influence of autoionisation branching ratio;
    - study of the REDA process.
4. Analysis of the scaled DW cross sections:
    - study for collisional ionisation;
    - study for the EA process.

The Scientific Novelty

1. New data of high accuracy became available for studies of charge distribution in plasma.
2. Correlation effects were investigated for the Fe^{3+} and W^{5+} ions, and new findings were presented.
3. The experimental data for the Se^{3+}, Fe^{3+} and W^{5+} ions were explained for the first time.
4. Scaling functions were applied to explain measurements of Fe^{3+}.
5. Influence of the DDI process was demonstrated in the theoretical study of single ionisation cross sections.
6. The REDA process was studied for the Se^{3+} ion for the first time.

Statements to Defend

1. Excitations to the higher-nl shells ($9 \leq n \leq 25$) increases the EA cross sections by $\sim$40 % for W^{25+}.
2. The difference of approximately 10 % among the levels of the ground configuration of W^{26+} is obtained for MRC.
3. Correlation effects diminish electron-impact single ionisation cross sections for near-neutral ions: Fe^{3+}, W^{5+}.
4. Scaling of the DW cross sections can be used to explain the experimental data for the ionisation of Fe^{3+}.
5. DDI diminishes single ionisation cross sections by 4 % for Se^{3+} .

Personal Contribution

1. Performed research tasks.
2. Performed calculations tasked by supervisor.
3. Modified code of programs used by the research team.
4. Developed programs, database procedures to calculate ionisation cross section.
5. Implemented big data technology that allowed calculation of previously impossible ionisation cross sections.
6. Delivered ideas and roadmaps to achieve scientific goals.
7. Delivered technological roadmaps to unlock more detailed ionisation calculations.

Thesis Outline

The doctoral dissertation has the following structure. The first chapter introduces the research problem, actuality, scientific novelty, primary goal and tasks of study, and defence statements. The second chapter describes the method used to calculate ionisation cross sections, and is divided into several parts. First, the formulas to calculate total ionisation cross sections are presented, and later the deep dive is taken into the construction of wave functions, calculations of radiative and Auger transitions.

We present the DW approximation used in calculations. The REDA process is described. Later sections introduce formulas for scaling factors.

One of the sections is dedicated to correlation effects while the last one in the theory part is dedicated to the modelling of the metastable fraction. The results chapter was divided into sections according to the statements to defend. Excitations to higher-nl shells are researched in tungsten, selenium and iron ions. Afterwards we discuss correlation effects following cross section scaling. Finally, we present the results describing contribution from the DDI process to the single ionisation cross sections. The last chapter presents the main conclusions.

THEORY

Electron Impact Ionisation

Electron impact single ionisation is one of many ways for an atom or ion to lose an electron. It happens when a free electron collides with an electron bound to an atom or ion. Collision outcome can be single direct ionisation or atom/ion excitation. The first one is a complete process and the second one has multiple ways to end.

One of the major tasks in this work is to calculate ionisation cross sections. In order to do that, it is necessary to understand various theoretical cross section calculation methods, starting with a simple cross section definition.

The probability of single electron-impact ionisation is expressed as a total ionisation cross section of underlying processes. We begin with this equation, and we will go all the way down to single calculation steps. The starting point is this formula expression:

$$\sigma_i(\epsilon_0) = \sum_j \sigma_{ij}(\epsilon_0). \tag{1}$$

Here $\sigma_i(\epsilon_0)$ is the total ionisation cross section at the free electron energy ϵ_0 and $\sigma_{ij}(\epsilon_0)$ is total ionisation cross section for atom/ion ionisation process from level i to level j depended on free electron energy.

Ionisation cross section for transition from one energy level to another can be expressed as:

$$\sigma_{ij}(\epsilon_0) = \sigma_{ij}^{\mathrm{DI}}(\epsilon_0) + \sigma_{ij}^{\mathrm{II}}(\epsilon_0), \tag{2}$$

$\sigma_{ij}^{\mathrm{DI}}(\epsilon_0)$ describes DI from level i to level j and $\sigma_{ij}^{\mathrm{II}}$ includes all indirect

ionisation processes, for example, such as EA and REDA.

DI cross section by electron impact can be written in terms of the collision strength Ω [42]:

$$\sigma_{ij}^{\mathrm{DI}}(\epsilon_0) = \frac{1}{k_0^2 g_i} \int_0^{\frac{\epsilon_0 - I}{2}} \Omega_{ij}(\epsilon_0, \epsilon) d\epsilon, \tag{3}$$

where ϵ_0 and k_0 is the energy and kinetic momentum of the incident electron, respectively, ϵ is the energy of the ejected electron, I is the ionisation energy, g_i is the statistical weight of initial state. Ω includes summation over the partial waves of the incident and scattered electrons [42].

Relation for kinetic momentum of the incident electron to his energy ϵ_0 is shown by this formula:

$$k_0^2 = 2\epsilon_0 \left(1 + \frac{\alpha^2}{2}\epsilon_0\right), \tag{4}$$

where α is the fine structure constant.

There are several indirect ionisation processes studied in this work. The second part of formula (2) can be written as:

$$\sigma_{ij}^{\mathrm{II}}(\epsilon_0) = \sigma_{ij}^{\mathrm{EA}}(\epsilon_0) + \sigma_{ij}^{\mathrm{REDA}}(\epsilon_0), \tag{5}$$

where $\sigma_{ij}^{\mathrm{EA}}(\epsilon_0)$ is a cross section of the EA process from level i to level j and $\sigma_{ij}^{\mathrm{REDA}}(\epsilon_0)$ is the REDA process cross section for the same levels.

The EA process starts by excitation from level i to level k which can decay through the Auger transitions to the level j of the next ionisation stage. A cross section of this kind of process can be expressed by equation:

$$\sigma_{ij}^{\mathrm{EA}}(\epsilon_0) = \sum_k \sigma_{ik}^{\mathrm{CE}}(\epsilon_0) B_{kj}^a, \tag{6}$$

where $\sigma_{ik}^{\mathrm{CE}}(\epsilon_0)$ corresponds to the CE cross section at the electron energy ϵ_0. B_{kj}^a is the autoionisation branching ratio, which is expressed as following:

$$B_{kj}^a = \frac{A_{kj}^a}{\sum_m A_{km}^a + \sum_n A_{kn}^r}, \tag{7}$$

where A_{kj}^a is the Auger transition probability from level k to level j and A_{kn}^r is the radiative transition probability from level k to level n.

Total REDA cross section is written as:

$$\sigma_{ij}^{\mathrm{REDA}}(\epsilon_0) = \sum_{kl} \sigma_{ik}^{\mathrm{DC}}(\epsilon_0) B_{kl}^{a} B_{lj}^{a}, \tag{8}$$

where $\sigma_{ik}^{\mathrm{DC}}(\epsilon_0)$ is the cross section for the dielectronic capture (DC) to the level k of the $A^{(q+1)+}$ ion [7]. B_{kl} and B_{lj} are branching ratios for ion transition processes from level k to level l ($A^{(q)+}$) and then to level j ($A^{(q-1)+}$).

Certain plasma modeling tasks require MRC data. MRCs are calculated using the electron-impact ionisation cross sections

$$\alpha_{ij}(T_e) = \left(\frac{1}{k_B T_e}\right)^{\frac{3}{2}} \left(\frac{8}{m_e \pi}\right)^{\frac{1}{2}} \int_0^{\infty} \epsilon \, \sigma_{ij}(\epsilon) \, exp(-\frac{\epsilon}{k_B T_e}) d\epsilon. \tag{9}$$

Here, k_B is the Boltzmann constant, m_e is the electron mass and $\sigma_{ij}(\epsilon)$ is the cross section for the transition from the level i to the level j.

Wave Functions

At first we need to construct each of atom/ion state initial and final wave functions by starting with following expression [44, 45]:

$$\Psi_\alpha = \sum_{i}^{N_{\mathrm{CSF}}} c_i(\alpha) \Phi_i, \tag{10}$$

Ψ and Φ are approximate and basis ion wave functions, also known as atomic state and configuration state functions (CSFs), respectively.

CSFs are formed by taking linear combinations of the orbitals to obtain eigenfunctions of the total angular momentums operators. An orthonormal set of CSFs can be created by varying the occupation numbers in configurations and coupling schemes.

Mixing coefficients $c_i(\alpha)$ are retrieved from the Hamiltonian H diagonalisation solving equation for energy state:

$$E_\alpha = \int \Psi_\alpha^\dagger H \Psi_\alpha d\tau = \sum_{r,s} c_r^*(\alpha) \int \Phi_r^\dagger H \Phi_s d\tau \, c_s(\alpha) = c_\alpha^\dagger H c_\alpha. \tag{11}$$

We use Dirac-Fock-Slater (DFS) Hamiltonian which includes relativ-

istic effects and is written as [44]:

$$H = \sum_{i=1}^{N} H_D(i) + \sum_{\substack{i,j \\ i<j}}^{N} \frac{2}{r_{ij}}, \tag{12}$$

Here, $H_D(i)$ is the single-electron Dirac Hamiltonian, r_{ij} is the distance between two electrons, which interaction is considered.

The basis states Φ_i, referred as CFSs, are antisymmetric sums of the products of N one-electron Dirac spinors ϕ_{nkm}

$$\phi_{n\kappa m} = \frac{1}{r}\begin{pmatrix} P_{n\kappa}(r)\chi_{\kappa m}(\Theta,\Phi,\sigma) \\ iQ_{n\kappa}(r)\chi_{-\kappa m}(\Theta,\Phi,\sigma) \end{pmatrix}, \tag{13}$$

where n is the principal quantum number, κ is the relativistic angular quantum number, $P_{n\kappa}(r)$ and $Q_{n\kappa(r)}$ are the large and small components of radial wave function, respectively. Θ and Φ are spherical coordinate system's polar angle and azimuthal angles, and σ is the electron spin respectively.

Radial functions $P_{n\kappa}(r)$ and $Q_{n\kappa}(r)$ are required to be orthonormal within each κ symmetry as follows:

$$\int_0^\infty \left[P_{n'\kappa}(r)P_{n\kappa}(r) + Q_{n'\kappa}(r)Q_{n\kappa}(r)\right] dr = \rho_{n'n}. \tag{14}$$

Here, $\rho_{n'n}$ is the Kronecker delta. $\chi_{\kappa m}$ is the spinor spherical harmonic in the lsj coupling scheme:

$$\chi_{\kappa m}(r) = \sum_{m_l,m_s} \langle lm_l m_s|jm\rangle\, Y_{lm_l}(\Theta,\Phi)\xi_{m_s}(\sigma), \tag{15}$$

where $\langle lm_l m_s|jm\rangle$ is eigenstates, Y_{lm_l} is spherical harmonic function and ξ_{m_s} is a spin state function. In order to determine the $P_{n\kappa}$ and $Q_{n\kappa}$, one has to solve the coupled Dirac equation for local central field $V(r)$:

$$\begin{aligned} \left(\frac{d}{dr} + \frac{\kappa}{r}\right) P_{n\kappa} &= \alpha\left(\epsilon_{n\kappa} - V + \frac{2}{\alpha^2}\right) Q_{n\kappa} \\ \left(\frac{d}{dr} - \frac{\kappa}{r}\right) Q_{n\kappa} &= \alpha\left(-\epsilon_{n\kappa} + V\right) P_{n\kappa} \end{aligned} \tag{16}$$

here α is the fine structure constant and $\epsilon_{n\kappa}$ are the energy eigenvalues

of the radial orbitals.

Equation of the DF [45] method is rewritten to match the form and units of formula (16):

$$\begin{aligned}\left(\frac{d}{dr}+\frac{\kappa_a}{r}\right)P_a &= \alpha\left(\frac{2}{\alpha^2}-\epsilon_a+\frac{Y_a}{r}\right)Q_a-\frac{\chi_a^{(P)}}{r},\\ \left(\frac{d}{dr}-\frac{\kappa_a}{r}\right)Q_a &= \alpha\left(\epsilon_a-\frac{Y_a}{r}\right)P_a-\frac{\chi_a^{(Q)}}{r},\end{aligned} \tag{17}$$

where subscript a is a subshell occupation number and:

$$\begin{aligned}\chi_a^{(P)} &= X_a^{(P)}+\frac{\alpha r}{\bar{q}_a}\sum_{b\neq a}\epsilon_{ab}Q_b,\\ \chi_a^{(Q)} &= X_a^{(Q)}-\frac{\alpha r}{\bar{q}_a}\sum_{b\neq a}\epsilon_{ab}P_b.\end{aligned} \tag{18}$$

The direct potential is

$$Y_a(r) = -rV_{nuc}(r)-\sum_{b,k}y^k(ab)Y_k(bb;r), \tag{19}$$

$$V_{nuc}(r) = -\frac{Z}{r}, \tag{20}$$

$$y^k(ab) = \left(\frac{1+\delta_{ab}}{\bar{q}_a}\right)\sum_r d_r^2 f_r^k(ab). \tag{21}$$

Inserting (20) and (21) into (19) we get

$$Y_a(r) = Z-\sum_{b,k}\left(\frac{1+\delta_{ab}}{\bar{q}_a}\right)\sum_r d_r^2 f_r^k(ab)Y_k(bb;r) \tag{22}$$

and the exchange potentials are

$$\begin{aligned}X_a^{(P)} &= \alpha\frac{1}{\bar{q}_a}\left[\sum_{\substack{b,k\\ b\neq a}}x^k(ab)Y_k(ab;r)Q_b+\sum_k x^k(abcd)Y_k(bd;r)Q_c\right],\\ X_a^{(Q)} &= \alpha\frac{1}{\bar{q}_a}\left[\sum_{\substack{b,k\\ b\neq a}}x^k(ab)Y_k(ab;r)P_b+\sum_k x^k(abcd)Y_k(bd;r)P_c\right]\end{aligned} \tag{23}$$

with

$$x^k(ab) = \sum_r d_r^2 g_r^k(ab),$$
$$x^k(abcd) = \sum_{\substack{r,s \\ r<s}} d_{rs} V_{rs}^k(abcd) \tag{24}$$

and

$$Y_k(bd;r) = r\int_0^\infty U_k(r,s)[P_b(s)P_d(s) + Q_b(s)Q_d(s)]ds. \tag{25}$$

The DFS method is faster compared to other methods due to the choice of central potential $V(r)$ [44], which can be viewed as an average approximation of the DF method:

$$V(r) = -\frac{2Z}{r} + V_c(r) - \left(\frac{24}{\pi}\rho\right)^{\frac{1}{3}}. \tag{26}$$

The first term is a potential due to the nucleus, while second and third describe electron-electron contribution. The spherically averaged classical potential $V_c(r)$ can be written as:

$$V_c(r) = \sum_{n',\kappa'} w_{n'\kappa'} \int_0^\infty \frac{2}{r_>}\left[P_{n'\kappa'}^2(r_2) + Q_{n'\kappa'}^2(r_2)\right] dr_2. \tag{27}$$

Summation is done over all occupied subshells, where $w_{n'\kappa'}$ is the occupation of subshell $n'\kappa'$ and $r_>$ is the greater of r and r_2. The last term in equation (26) is the exchange energy of an electron in a free-electron gas of density ρ averaged over all possible momenta of the electron. The spherically averaged value for this is:

$$\rho(r) = \frac{1}{4\pi r^2}\sum_{n'\kappa'} w_{n'\kappa'}\left[P_{n'\kappa'}^{(2)}(r) + Q_{n'\kappa'}^2(r)\right]. \tag{28}$$

However, expression (26) includes the undesirable self-interaction and has incorrect asymptotic behaviour. To exclude self-interaction, the following expression was used to describe local central potential electron-electron

interaction [42]:

$$
\begin{aligned}
V^{ee}(r) = \frac{1}{r\sum_a \omega_a \rho_a(r)} \Bigg\{ & \sum_{ab} \omega_a(\omega_b - \delta_{ab}) Y^0_{bb}(r)\rho_a(r) \\
& + \sum_a \omega_a \left(\omega_a - 1\right) \sum_{k>0} f_k(a,a) Y^k_{aa}(r)\rho_a(r) \\
& + \sum_{a\neq b} \sum_k \omega_a \omega_b g_k(a,b) Y^k_{ab}(r)\rho_{ab}(r) \Bigg\},
\end{aligned}
\tag{29}
$$

where $a = n\kappa$ and $b = n'\kappa'$ are virtual indices denoting the subshells, and

$$
\begin{aligned}
\rho_{ab} &= P_a(r)P_b(r) + Q_a(r)Q_b(r), \\
Y^k_{ab}(r) &= r\int \frac{r^k_<}{r^{k+1}_>}\rho_{ab}(r')dr',
\end{aligned}
\tag{30}
$$

$r_<$ and $r_>$ notes the lesser and greater of r and r', respectively. f_k and g_k are the direct and exchange coefficients defined as:

$$
\begin{aligned}
f_k(a,b) &= -\left(1 + \frac{1}{2j_a}\right) \begin{pmatrix} j_a & k & j_b \\ -\frac{1}{2} & 0 & \frac{1}{2} \end{pmatrix}^2, \\
g_k(a,b) &= -\begin{pmatrix} j_a & k & j_b \\ -\frac{1}{2} & 0 & \frac{1}{2} \end{pmatrix}^2,
\end{aligned}
\tag{31}
$$

where $\begin{pmatrix} j_1 & j_2 & j_3 \\ m_1 & m_2 & m_3 \end{pmatrix}$ is the Wigner [46] $3j$ symbol. The equation (29) has the correct asymptotic behaviour at large r, since the self-interaction term is explicitly excluded.

Radiative Transitions

A radiative transition between the bound states of an atom occurs when an electron jumps to an upper or excited level by absorption of a photon (photo-excitation), or jumps to a lower level by the emission of a photon (de-excitation or radiative decay). The electric dipole transitions, also referred to as allowed transitions, are the strongest types of electromagnetic transitions [47]. In general, dipole transitions contribute 98.8 %

and electric quadrupoles contribute 0.6 % of all transitions. Therefore, it is sufficient to consider only electric dipole transitions in a study of branching ratios. We can define approximate transition operator [48]:

$$O_p^{(t)} = -e \sum_i r_i^t C_p^{(t)}(\theta_i, \phi_i). \tag{32}$$

Here, e is absolute value of electron charge, r_i^t is an operator of particle position and $C_p^{(t)}$ - spherical function operator. The subscript i covers the coordinates of all of an atom's electrons. The rank of a transition operator t is not zero. The case $O^{(1)}$ is called dipole operator and $O^{(2)}$ - quadrupole. Using Wigner-Eckart theorem, it can be seen that its matrix element depends on the projections of the total momentum:

$$\langle \gamma J M | O_p^{(t)} | \gamma' J' M' \rangle = (-1)^{(J-M)} \begin{pmatrix} J & t & J' \\ -M & p & M' \end{pmatrix} \langle \gamma J || O^{(t)} || \gamma' J' \rangle. \tag{33}$$

This equation reveals the selection rule for the quantum number J in a case of electric dipole transitions:

$$\Delta J = 0, \pm 1; \quad J + J' \geqslant 1. \tag{34}$$

Auger Transitions

Auger transitions are autoionising transitions from the highly excited states of atoms containing vacancies. They are part of the fundamental process in the spontaneous de-excitation of atoms having a vacancy. Since a state with a vacancy is distinguished from the final state of an ion plus free-electron system by the quantum numbers of two electrons, Auger transitions are usually defined by a basic two-electron interaction – the electrostatic interaction between electrons. One electron fills the vacancy, and this interaction transfers the transition energy to the other electron, which then escapes the atom as a free Auger electron. The probability of radiationless decay of an autoionisation state:

$$W_A(\gamma \to \gamma' \epsilon \gamma'') = \hbar^{-1} \left| \langle \gamma' \epsilon \gamma'' | H | \gamma \rangle \right|^2, \tag{35}$$

where γ notes quantum numbers of a wave function of an autoionisation state, which is in the superposition of functions from the discrete and continuous spectra. γ' notes a wave function for the discrete state of an atom, γ'' denotes the remaining quantum numbers of the electron and whole system, ϵ is an energy of a free electron. The system Hamiltonian H can be selected (one-electron, two-electron operator or relativistic) depending on a specific case. A transition can only be made between system states having the same energy, and following this reasoning ϵ can be defined as energy difference between two atomic states:

$$\epsilon = E(\gamma) - E(\gamma'). \tag{36}$$

An Auger transition is possible only when the total angular momentum of the system, J, is conserved, and the probability is independent of the projection of this angular momentum. The operator (H) is even, and system parity must be preserved.

Resonant Excitation-Double Autoionisation process

Electron and an ion impact may result in the removal of one or several electrons from the ion. This process can be analysed as a combination of several steps. The first step is the formation of an intermediate resonance state. An inner-shell electron is excited, hence the incident electron is captured to a bound state (dielectronic capture). The resulting short-lived recombined ion state is highly excited, and two electrons can be ejected during the following two steps (at least) of relaxation processes. Therefore when the ion is excited to the state where it has enough energy for two sequential Auger, Coster-Kronic or super Coster-Kronic processes.

Dielectronic capture cross section can be written as:

$$\sigma_{im}^{DC}(\epsilon_0) = 7.88 \cdot 10^{-31} cm^2 eV^2 s \frac{1}{\epsilon_0} \frac{g_m}{2g_i} \frac{A_{mi}^a \cdot \Gamma_m}{\Delta E_{mi}^2 + \Gamma_m^2/4}. \tag{37}$$

Here, index $_{im}$ denotes intermediate excited state, ϵ_0 is an electron energy and ΔE_{mi} is the resonance energy obtained as the difference from initial state i and state m. g_m and g_i are statistical weights of the excited state

m, formed by dielectronic capture and the initial state i, respectively. A^a_{mi} is an autoionisation rate of state m for a transition to state i and Γ_m is the total width of state m:

$$\Gamma_m = \hbar \left[\sum_k A^a_{mk} + \sum_f A^r_{mf} \right]. \tag{38}$$

A^r_{mf} denotes the rate for the radiative transition from state m to state f.

Many short-lived intermediate autoionising states may be involved in the double-ionisation REDA process. Although it is pretty easy to understand or visualise, it is not easy to compute, as various pathways may exist for final multiple-ionisation states. Auger processes, which involve many inner-shell transitions, lead to Auger and radiative cascades.

Distorted Wave Approximation

The DW was introduced by Massey and Mohr in 1933 [49] while solving the electron-scattering problem. However, only in the early 1970s it was resurrected, because other plane-wave approximations were unable to produce accurate results to explain experimental data [50].

The idea of DW approximation is quite simple and can be considered in two cases. The first, the incident electron is taken to be elastically scattered by the initial-state atomic potential. Then, the incident electron makes a transition to a state in which the final-state atomic potential is elastically scattering. It is a direct process. The second, the incident electron is captured into the atom's bound state, while one of the initially bound electrons is ejected into an elastic-scattering state. This is viewed as the exchange process. In both cases, initial and final states are calculated using perturbation methods.

Collision strength for excitation process can be expressed as:

$$\Omega_{ij} = 2 \sum_{\kappa_i \kappa_j} \sum_{J_T} [J_T] \left| \langle \psi_i \kappa_i, J_T M_T \left| \sum_{i<j} \frac{1}{r_{ij}} \right| \psi_j \kappa_j, J_T M_T \rangle \right|^2, \tag{39}$$

where κ_i and κ_j are relativistic angular quantum numbers of the incident and scattered electrons, respectively, J_T is the total angular momentum

when the target state is coupled to the continuum orbital, M_T is the projection of the total angular momentum, and $[J] = 2J + 1$. A distance between two electrons is labeled as $.r_{ij}$. Initial and final state wave functions of the systems for bound electrons are ψ_i and ψ_j, respectively.

The electron impact excitation collision strength is given by

$$\Omega_{ij} = 2 \sum_{\substack{\kappa, J_T \\ k, \alpha_i \beta_j}} Q^k(\alpha_i\kappa; \beta_i\kappa) \langle \psi_i || Z^k(\alpha_i, \kappa) || \psi_j, \kappa; J_T \rangle \langle \psi_i || Z^k(\beta_i, \kappa) || \psi_j, \kappa; J_T \rangle, \quad (40)$$

here, κ is the relativistic angular quantum number of the ejected electron, α and β denote single electron state, J_T is the total angular momentum of the final state coupled with the ejected electron. Radial integral Q^k is defined as:

$$Q^k(\alpha_i\alpha_j; \beta_i\beta_j) = \sum_{\kappa_i\kappa_j} [k]^{-1} P^k(\kappa_i\kappa_j; \alpha_i\alpha_j) P^k(\kappa_i\kappa_j; \beta_i\beta_j) \quad (41)$$

and

$$P^k(\kappa_i\kappa_j; \alpha_i\alpha_j) = X^k(\alpha_i\kappa_j; \alpha_j\kappa_j) + \sum_t (-1)^{k+t} [k] \begin{Bmatrix} j_{\alpha_i} & j_j & t \\ j_i & j_{\alpha_j} & k \end{Bmatrix} X^t(\alpha_i\kappa_i; \kappa_j\alpha_j), \quad (42)$$

and X^k with Z^k are tensor operators of electrostatic interaction between electrons. Wigner $6j$ symbol is expressed as $\begin{Bmatrix} j_{\alpha_i} & j_j & t \\ j_i & j_{\alpha_j} & k \end{Bmatrix}$. Using Racah decoupling formula it is possible to simplify the angular factors and by carrying out analytical reduction the following can be concluded:

$$\Omega_{ij} = 2 \sum_{k, \alpha_i\beta_i} \delta_{j_{\alpha_0} j_{\beta_i}} [j_{\alpha_i}]^{-1} \bar{Q}^k(\alpha_i, \beta_i) \langle \psi_j || \tilde{a}_{\tilde{\alpha_i}} || \psi_i \rangle \langle \psi_j || \tilde{a}_{\tilde{\beta_i}} || \psi_i \rangle, \quad (43)$$

where $\bar{Q}^k(\alpha_i, \beta_i) = \sum_\kappa Q^k(\alpha_i\kappa; \beta_i\kappa)$. Integration of the collision strength over the energy of the ejected electron ϵ gives the total ionisation cross section

$$\sigma(\epsilon_0) = \int_0^{(\epsilon_0 - I)/2} \frac{1}{k_0^2 g_0} \Omega_{ij} d\epsilon, \quad (44)$$

where I is defined as ionisation energy, ϵ_0 and k_0 are the energy and kinetic momentum of the incident electron, ϵ is the energy of the ejected electron and g_0 is a statistical weight of the initial state.

Scaled Distorted Wave Cross Sections

The basic principle of scaling for ionisation cross sections was implemented in Lotz formula [31]. Later, scaling rules were expanded by Aichele *et al.* [51]. Furthermore, after that, multiple attempts have been made. None of the proposed scaling rules can claim to provide reliable cross section data for electron-impact single and multiple ionisations.

A recent comprehensive overview of multiple ionisations by electron impact and the application of scaling formulas has been provided by Hahn and Savin for atoms and ions of He through Zn [52]. It could be argued that this is not a new idea. However, it was never applied before to the DW method. During our investigation of ionisation processes, we noticed that some theoretical and experimental cross sections have differences that can be mitigated using scaling factors. Generally, single-ionisation cross sections for neutral atoms and near-neutral ions calculated using the DW approach are overestimated, which is one of the reasons to use the scaling factor.

Scaling has a meaning of corrections to the chosen calculation model. Those corrections were identified by Kim [36] :

- account for electron exchange effect;
- distortion of plane waves;
- polarisation of the target;
- shielding of the nuclear charge.

However, it is possible that scaling does account for any other corrections or excluded physical processes inside or near the vicinity of the ion.

It is a well-known fact that the DW approximation often overestimates cross sections for neutral atoms or near-neutral ions. Therefore, the scaling factors were suggested to be used to diminish the DW cross sections for the electron-impact ionisation and excitation processes [53].

The scaled cross sections for electron-impact excitation are expressed by the following equation [36, 53]:

$$\sigma_{ij}^{\mathrm{CE}^*}(\epsilon) = \frac{\epsilon}{\epsilon + \Delta E_{ij} + \epsilon_b}\sigma_{ij}^{\mathrm{CE}}(\epsilon), \tag{45}$$

where ϵ_b is the bounding energy of the electron. The scaling for the direct ionisation cross sections for neutral atoms is expressed by the equation:

$$\sigma_{ij}^{\mathrm{CI}^*}(\epsilon) = \frac{\epsilon}{\epsilon + I + \epsilon_k}\sigma_{ij}^{\mathrm{CI}}(\epsilon), \tag{46}$$

where I is the ionisation energy, and ϵ_k is the kinetic energy of the bound electron. The other scaling factor we used for near neutral ions:

$$\sigma_{ij}^{\mathrm{CI}^*}(\epsilon) = \frac{\epsilon}{\epsilon + I}\sigma_{ij}^{\mathrm{CI}}(\epsilon). \tag{47}$$

Here, the kinetic energy is omitted in the denominator to describe cases where we can neglect bound electron kinetic energy described by $\epsilon_k \ll (\epsilon + I)$.

Correlation Effects

Multi-electron interaction in an atom is an important problem. Understanding and taking into account various correlation effects bring results closer to exact values. The difference between the exact eigenvalue of the Hamiltonian and its value in the Hartree-Fock (HF) approximation for the state under consideration is the correlation energy [54]. Therefore, the correlation energy is defined as:

$$E_{corr} = E_{exact} - E_{HF}. \tag{48}$$

E_{exact} is known exactly or with high accuracy. Basically, it is an experimental value with some theoretical corrections for the relativistic effects and nuclei movements. E_{HF} is energy calculated by the HF method.

The multi-configuration method is fundamental for accounting correlations between electrons. Atomic wave function is considered as an expansion in the basis of the configuration state functions having the

same parity:

$$\Phi(\Gamma J) = \sum_{K'\gamma'} C^{\Gamma}_{K'\gamma' J} \Psi(K'\gamma' J). \tag{49}$$

Here, $C^{\Gamma}_{K'\gamma' J}$ is the expansion coefficient, Ψ is the one configuration function defined in a one or many configuration approximation, Φ is the many configuration function that corresponds to a mixture of configurations.

Moreover, the functions Ψ are calculated in a one-configuration approximation. The expansion coefficients are defined by diagonalising the energy matrix based on these functions, and this method is called configuration interaction (CI). The one-configuration wave functions are calculated separately for each configuration, and they are orthogonal to each other as the same local potential is used for all functions.

Another important property is that the orthonormalised multi-configuration matrix elements have zero values if the configurations differ by the quantum numbers of more than two electrons. These configurations affect one another only through interaction with other configurations. Finding such intermediate configurations is a great challenge, because the scope of calculations with each added configuration increases significantly.

Previously, it was suggested to use CIS to determine a list of admixed configurations having the largest influence on the configuration under consideration. The CIS was defined previously by the equation [48, 55]:

$$T(K, K') = \frac{\sum_{\gamma\gamma'} \langle \Phi(K\gamma)|H|\Phi(K'\gamma')\rangle^2}{\bar{E}(K, K')^2}. \tag{50}$$

This quantity, divided by the statistical weight $g(K)$ of the studied configuration K, has the meaning of the average contribution of the admixed configuration K' to the expansion of the wave function for K. The summation in Eq. (50) is performed over all states γ and γ' of the K and K' configurations, respectively. The quantity $\langle \Phi(K\gamma)|H|\Phi(K'\gamma')\rangle$ is the inter-configuration matrix element of the two-electron electrostatic Hamiltonian and $\bar{E}(K, K')$ is an average energy difference between the

configurations:

$$\bar{E}(K,K') = \frac{\sum_{\gamma\gamma'}[\langle\Phi(K\gamma)|H|\Phi(K\gamma)\rangle - \langle\Phi(K'\gamma')||\Phi(K'\gamma')\rangle]}{\sum_{\gamma\gamma'}\langle\Phi(K\gamma)|H|\Phi(K'\gamma')\rangle^2} \times\langle\Phi(K\gamma)|H|\Phi(K'\gamma')\rangle^2. \tag{51}$$

Theoretical Modeling of Meta-stable Fraction

Since the ions are produced in the ion source plasma, it makes sense to assume statistical populations of levels within each contributing configuration. This kind of assumption has been successfully applied in numerous previous studies of collision processes involving ion beams, and is considered the most realistic approach.

Since the experiment did not directly provide information about the relative fractions of ions in certain electronic levels, an attempt has to be made to model the experimental cross section function $\sigma^{exp}(\epsilon_0)$ by a linear combination of the theoretical cross sections $\sigma_i^{th}(\epsilon_0)$ calculated for ions in initial levels i. The fractions λ_i (with $\sum\lambda_i = 1$) by which the levels i contribute to the model cross section are to be determined by comparison of the weighted sum of the theoretical cross sections with the experimental data. Ideally, the experimental cross section can be expressed by

$$\sigma^{exp}(\epsilon_0) = \sum_{i=1}^{m}\lambda_i\sigma_i^{th}(\epsilon_0) \tag{52}$$

with a suitable set of ion-beam fractions λ_i. Here m is the number of levels contributing to the measurements.

We can modify Eq. 52 by reducing number of fitting parameters:

$$\sigma^{exp}(\epsilon_0) = \sum_k c_k \frac{\sum_i(2\times {}^kJ_i+1)\times {}^k\sigma_i^{th}(\epsilon_0)}{\sum_i(2\times {}^kJ_i+1)}, \tag{53}$$

where c_k are fitting parameters for each of the configurations considered, the fraction with a sum over i in the numerator and in the denominator

is the configuration averaged cross section for the long-lived levels i in configuration k, ${}^kJ_i$ is the total angular momentum quantum number of level i in configuration k and ${}^k\sigma_i^{th}(\epsilon_0)$ is the total single-ionisation cross section for level i in configuration k.

The second model uses only one fitting parameter to determine fraction of metastable ions in beam. With the argument that the ions are primarily produced in a plasma, a Boltzmann distribution for the population of excited levels may be considered. This reduces the problem to fitting the temperature T. Eq. (52) then takes the form

$$\sigma^{exp}(\epsilon_0) = \frac{\sum_{i=1}^{m}(2J_i+1)\exp[-\epsilon_i/(kT)]\sigma_i^{th}(\epsilon_0)}{\sum_{i=1}^{m}(2J_i+1)\exp[-\epsilon_i/(kT)]}. \tag{54}$$

Here, J_i is the total angular momentum quantum number and ϵ_i is the excitation energy of level i.

The third model or variant treats all metastable levels as free fitting parameters. Fitting all experimental data points does not provide any difficulty. However, the model is rooted more in mathematical methods than in the physics of ion sources and ion beams. The fractions λ_i are chosen such that the function

$$f(\lambda_1, \lambda_2, \ldots, \lambda_m) = (\sigma^{exp}(\epsilon_0) - \sum_{i=1}^{m}\lambda_i\sigma_i^{th}(\epsilon_0))^2 \tag{55}$$

reaches a minimum. All three provided cases offer different paths to model metastable fractions in an ion beam. Later, we will present practical applications of these methods.

RESULTS

Convergence of the Excitation Autoionisation Cross Sections

The EA process includes electron impact excitation with subsequent autoionisation. Furthermore, convergence of the excitation cross sections has to be reached in order to provide reliable atomic data. We perform some initial calculations using Unresolved Transition Arrays (UTA) to determine the limit, after which the inclusion of higher-nl shells does not produce a noticeable change to the total ionisation cross section. The descriptions of our findings for each research case and the presentations of several cases, where the importance to reach EA cross section convergence was proved, are provided below.

Tungsten Ions

Previous studies for highly charged tungsten ions W^{18+} [56], W^{25+} [57], W^{26+} [58] and W^{27+} [59, 60] demonstrated the importance of excitations to higher shells (n $>$ 8) which were needed to reach convergence of the EA cross sections.

We studied electron impact single ionisation for the W^{5+}, W^{25+} and W^{26+} ions. The upper limit of n usually depends on whether the EA cross section reaches convergence. We assume that the upper n limit is reached when excitations to the higher shells add less that 5 % of the total ionisation cross section. The study includes subshells with the orbital quantum numbers $l \leqslant 6$.

The presentation of our findings starts with examples where excitation to the higher shells makes obvious difference in the results. Firstly, we

present research results for W^{26+}, then investigation of W^{25+}, and finally results for W^{5+} are provided.

W^{25+} Ion [A1]

The ground configuration of the W^{25+} ion consists of 41 levels. Our analysis of the electron-impact ionisation cross sections is based on the study of the ground level $4f^3_{5/2}$ ($J = 4.5$). The cross sections for the other ground configuration levels have a similar character and are not presented here. Moreover, cross sections from the first level $4f^2_{5/2}(4)5s$ ($J = 3.5$) of the excited configuration are similar to the ones from the ground level, except contribution from the excitations to shells with $n \leqslant 8$ is much more pronounced compared to the excitations to shells with $9 \leqslant n \leqslant 25$. The ionisation energy for the ground state of W^{25+} is calculated to be 781.78 eV, while the CADW one obtained by Loch *et al.* [61] corresponds to 778.04 eV. The NIST recommended value of 784.92 ± 1.9 eV [62] is in quite close agreement with our result.

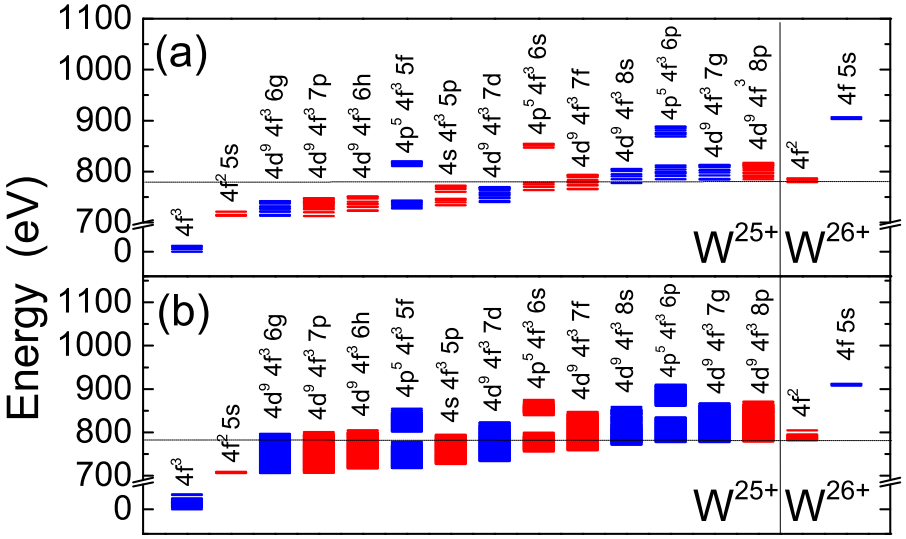

Figure 1: Subconfigurations (a) and energy levels (b) of two lowest configurations, and configurations with the energy levels that straddle the ionisation threshold for the W^{25+} ion. Red colour – even configurations, blue colour – odd configurations.

All the considered levels of configurations lie below the calculated double ionisation threshold of 1612.38 eV. The first two lowest configur-

ations of the W^{25+} and W^{26+} ions, and configurations with the energy levels that straddle the ionisation threshold of W^{25+} are shown in Figure 1. Subconfigurations of the corresponding configurations are displayed in Figure 1 (a). All the presented configurations arise from the same single-electron promotions as for the W^{27+} [59] and W^{26+} [63] ions, except a few cases. The configurations produced by the $4d \rightarrow 6g$, $4d \rightarrow 6h$, $4d \rightarrow 7p$ and $4s \rightarrow 5p$ excitations from the ground configuration are below the ionisation threshold for the W^{26+} and W^{27+} ions. The excitations from the $4d$ subshell to the shells with $6 \leqslant n \leqslant 8$ lead to many configurations with the energy levels that straddle the ionisation threshold of W^{25+} (Figure 1 (b)). In addition, a few configurations formed by promotion from the $4s$ and $4p$ subshells also straddle the ionisation threshold, but in these cases, excitations reach only $n = 5$ and $n = 6$. On other hand, all subconfigurations of the $4s4f^35p$, $4d^94f^36g$, $4d^94f^36h$, $4d^94f^37p$ and $4d^94f^37d$ configurations are below the ionisation threshold (Figure 1 (a)), and corresponding subconfiguration-average DW (SCADW) calculations do not provide contribution to the EA process. Furthermore, the subconfigurations of $4p^54f^36p$ and $4d^94f^38p$ are above the ionisation threshold (Figure 1 (a)).

Contributions of the EA channels originating from the excitations to the higher-nl shells up to $n \leqslant 25$ are shown in Figure 2. These data are obtained using the LLDW approximation without (Figure 2 (a)) and with (Figure 2 (b)) radiative damping. It is evident from the data that the EA channels originating from the excitations to the higher shells increase cross sections approximately by 60 %. The SCADW cross sections have the same tendency. Therefore, they are not presented here. These results demonstrate that the inclusion of the excitations to the higher-nl shells are vital in the EA process for this ion. This conclusion is in agreement with recent findings for W^{26+} [63] and W^{27+} [59]. Furthermore, the radiative damping has a large impact on the ionisation cross sections. The radiative transitions diminish the cross sections for the indirect process by about 25 %.

Figure 3 presents LLDW results for the EA cross sections corresponding to excitations to the various nl shells with radiative damping. It has to be noted that the total contribution of the excitations from the $4s$, $4p$ and $4d$ subshells to the $l = 4$ orbital is the largest compared to the other orbitals. The same tendency was observed in the previous investigations

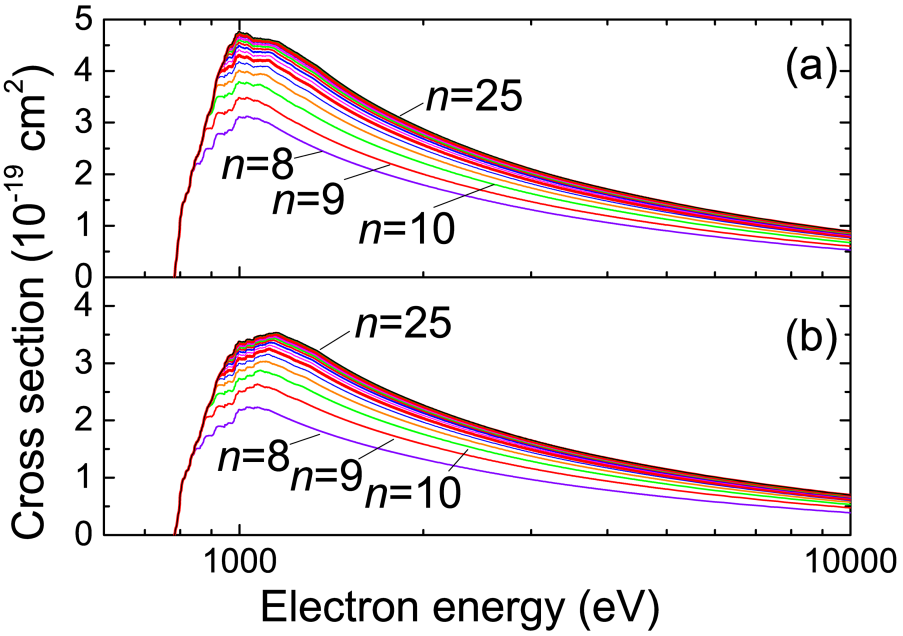

Figure 2: EA channels to the higher-nl shells for the ground level of the W^{25+} ion. LLDW calculations: (a) without radiative damping and (b) with radiative damping.

for the W^{26+} [63] and W^{27+} [59] ions. Likewise, the excitations to the $l = 2$ orbital lead to the strong EA channel. In this case, the relative contribution is stronger for the $n \leqslant 25$ shells (Figure 3 (b)) compared to the excitations to the shells with $n \leqslant 8$ (Figure 3 (a)). This can be explained by the fact that the strongest excitations can be attributed to the $l = 2$ orbital, which produces configurations with energy levels above the ionisation threshold, taking place from the $4d$ subshell to the higher shells ($9 \leqslant n \leqslant 25$). This also proves that our selection of $l \leqslant 6$ is sufficient to include all major contributions. However, main contribution to the EA cross sections arises from $4p$ to the $l = 1$ orbital transitions when $n \leqslant 8$.

Figure 4 shows the EA cross sections obtained in the LLDW approximation with radiative damping for excitations from the $4s$, $4p$ and $4d$ subshells. The EA channel for the excitations from the $4d$ subshell is predicted to produce the largest contribution when $9 \leqslant n \leqslant 25$. Similar results were obtained for the other tungsten ions with the $4f$ electrons in the outermost subshell of the ground configuration [59, 63, 64]. On the

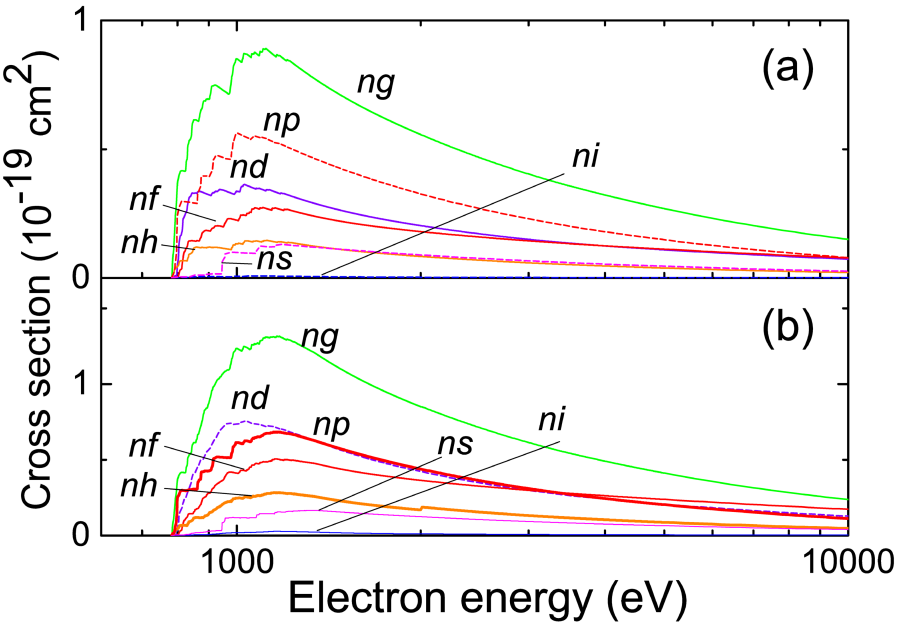

Figure 3: EA cross sections corresponding to excitations to various orbitals for the ground level of the W^{25+} ion: (a) $n \leqslant 8$, (b) $n \leqslant 25$. LLDW calculations with radiative damping.

other hand, the EA channels corresponding to the excitations from $4d$ to subshells with $n \leqslant 8$ are weaker than the ones from the $4p$ subshell (Figure 4). This can be explained by the fact that a large number of configurations produced by the excitations from the $4d$ subshell are below the ionisation threshold. In the meantime, the studied higher-nl shells ($9 \leqslant n \leqslant 25$) have the largest contribution to the excitations from the $4d$ subshell compared to $4p$ and $4s$. The cross sections increase by a factor of 2 for the $4d$ subshell when the higher shells are taken into consideration.

The total theoretical electron-impact single-ionisation cross sections for W^{25+} are presented in Figure 5. The contributions of ionisation from various subshells to the DI and EA processes are highlighted in Figure 5 (a). It can be clearly seen that the weight of the $4d$ subshell dominates for this ion. A large number of electrons and the closeness of the binding energy to the ionisation energy provide the dominant role for the $4d$ subshell. The relative contribution from the $4p$ subshell is much lower for the DI process compared to EA.

Interestingly, the EA process provides about 50 % to the total ionisa-

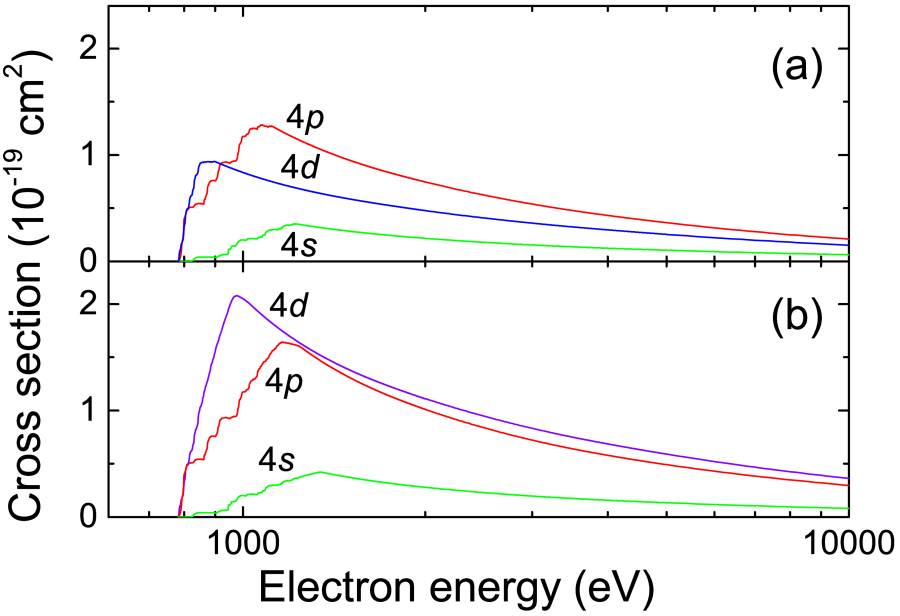

Figure 4: EA cross sections corresponding to excitations from the $4s$, $4p$ and $4d$ subshells for the ground level of the W^{25+} ion: (a) $n \leqslant 8$ and (b) $n \leqslant 25$. LLDW calculations with radiative damping.

tion cross sections. The study based on the CADW calculations obtained a relatively small EA contribution for ions from W^{11+} to W^{27+} [65]. It was suggested [63] that configuration-average approximation can be the cause of the diminished influence of the EA process. On the other hand, the strong excitations to the $l = 4$ orbital were omitted in the CADW calculations [65], as a contribution of this orbital was very small for the lower ionisation stages [32]. Figure 5 (b) clearly demonstrates that even excitations to shells with $n \leqslant 8$ obtained in the LLDW approximation produce a significant contribution to the total ionisation cross sections of the W^{25+} ion. The similar effect has been observed for the others, previously investigated, tungsten ions: W^{26+} [63] and W^{27+} [59].

Summarising this discussion, it can be concluded that excitations to higher-nl shells are important in the study of electron-impact ionisation in W^{25+}. The DI cross sections calculated in the potential of ionising ion are approximately 5 % higher than the current values. The contribution from the excitations to the shells with $n > 25$, which have not been investigated in this work, would be less than 5 %. What is more, additional errors

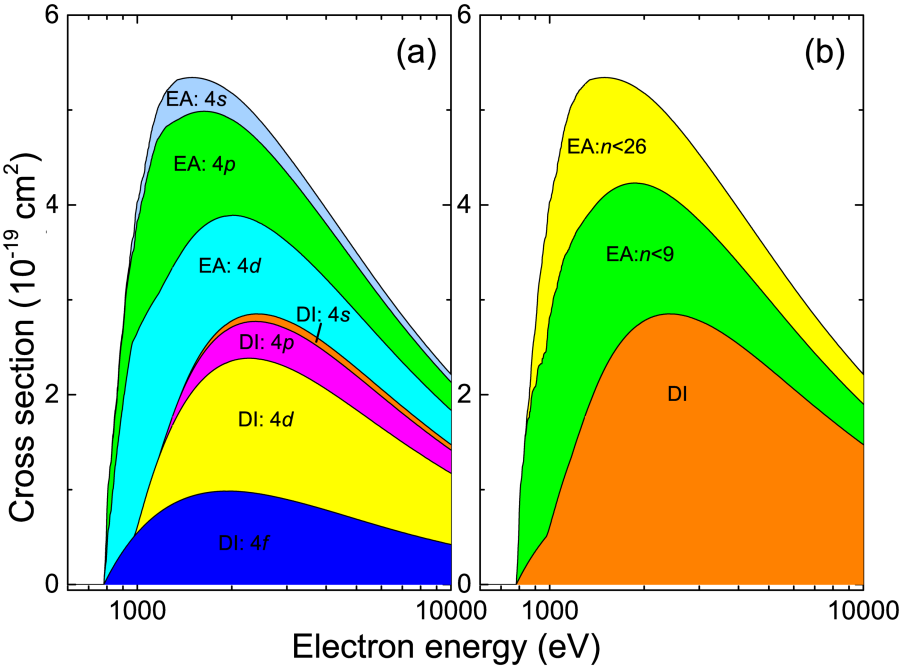

Figure 5: Total LLDW ionisation cross sections for the ground level of the W^{25+} ion. The contributions from different subshells are highlighted by different colours. (a) EA and DI contributions from various subshells as well as (b) EA contributions from the excitations to the lower ($n \leqslant 8$) and higher ($9 \leqslant n \leqslant 25$) shells. LLDW calculations with radiative damping.

can arise from the omitted correlation effects.

W^{26+} Ion [A2]

The ground configuration of the W^{26+} ion is [Ni] $4s^2 4p^6 4d^{10} 4f^2$ and it consists of 13 fine-structure levels. The energies for all ground configuration levels calculated by the DFS method are provided in Table 1.

The splitting of energy levels equals 23.08 eV, while the calculated single ionisation threshold amounts to 830.60 eV. The energy levels of the main configurations producing the largest contribution to the EA cross sections along with the ground configurations for W^{26+} and W^{27+} are presented in Figure 6.

Our obtained energy levels, relative to the ground one, are slightly higher than GRASP2K [66] energy levels [67], except the highest one.

Table 1: Multiconfiguration Dirac-Fock (GRASP2K) [66] and DFS (FAC) energy levels of the ground configuration for W^{26+}. Energies are given relative to the ground level energy and compared with Kramida & Reader [62]. J is the total angular momentum quantum number.

Index	Config.	J	E_{GRASP} (eV)	E_{FAC} (eV)	NIST (eV)
0	$4f^2_{2.5}(4)$	4	−430676.657	−430656.913	−430088.568
1	$4f^2_{2.5}(2)$	2	2.423	2.549	-
2	$4f_{2.5}4f_{3.5}(5)$	5	3.107	3.216	-
3	$4f_{2.5}4f_{3.5}(4)$	4	4.755	4.838	-
4	$4f_{2.5}4f_{3.5}(3)$	3	4.788	4.981	-
5	$4f^2_{3.5}(6)$	6	5.762	5.945	-
6	$4f^2_{3.5}(4)$	4	8.419	8.620	-
7	$4f_{2.5}4f_{3.5}(2)$	2	9.008	9.352	-
8	$4f^2_{2.5}(0)$	0	9.501	9.804	-
9	$4f_{2.5}4f_{3.5}(1)$	1	10.907	11.324	-
10	$4f_{2.5}4f_{3.5}(6)$	6	11.076	11.364	-
11	$4f^2_{3.5}(2)$	2	13.259	13.728	-
12	$4f^2_{3.5}(0)$	0	23.121	23.080	-

The difference can be explained by the correlation effects which were considered in the previous calculations using configuration interaction strength [55, 68–70]. The current work presents the single-configuration study. However, the difference between both sets does not reach more than 0.5 eV. It is worth noting that the energy of the ground level, obtained by Kramida and Reader [62] using a semi-empirical method, which is based on the Hartree-Fock calculations of the electron binding energies, scaled according to experimental results and is higher than GRASP2K as well as our values.

In order to assess the impact of ionisation from the ground configuration levels on the DI and EA cross sections, we have separately studied these processes in the W^{26+} ion for each level. The maximum contribution to the total DI cross section comes from the $4d$ subshell ionisation, while the $4p$ and $4f$ ionisation is approximately equal in parts, has less influence (see Figure 7). As expected, the $4s$ subshell produces the least contribution to the total DI. Our obtained DI rates for all levels of the ground configuration are below the CADW values [65] as has been noticed in the previous studies [63, 64, 71, 72]. The semi-relativistic approximation includes relativistic corrections by taking into account Darwin and

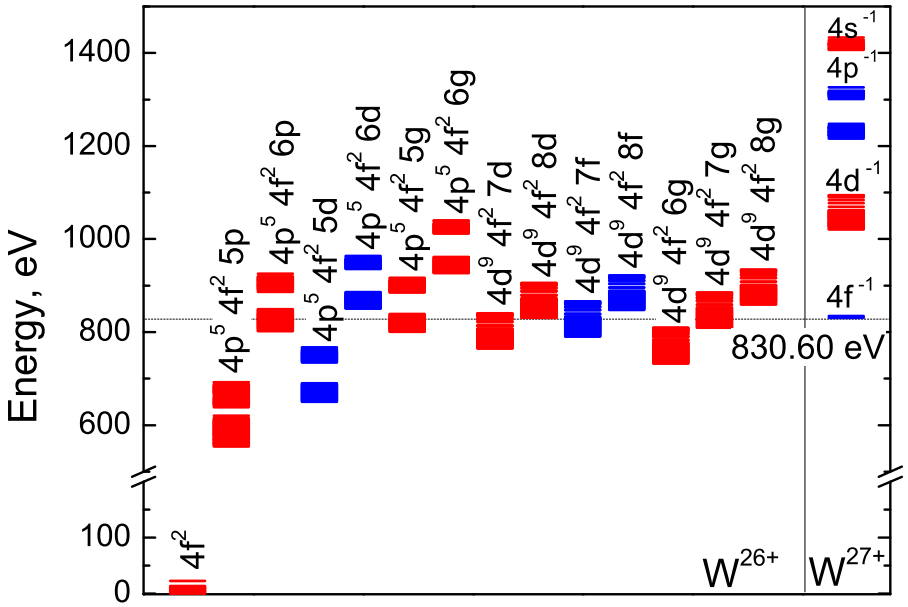

Figure 6: The diagram of energy levels for the W^{26+} and W^{27+} ions. Ground configurations and configurations leading to the strongest EA and DI channels are presented. In addition, configurations corresponding to excitations to the lower principal quantum numbers instead of the ones producing the strongest EA MRC are shown.

mass-velocity operators in the Hartree-Fock equations [73]. This can be explained by different potentials used in the CADW calculations for the ground level. Considering our level-by-level investigation, the DI MRCs calculated for the ground level of the $4f^2$ configuration are more or less the same as they are for the other levels of the ground configuration. Therefore, the MRCs are presented only for the ground level (Figure 7). The difference in the DI rate coefficients for different levels of the ground configuration is only about 1 % and this difference mainly arises from the $4f$ subshell. The same effect has been observed for the W^{17+} ion [64]. The semi-relativistic study did not include ionisation from the $4s$ subshell, the contribution of which is much smaller compared to the other subshells. The largest difference between the DFS and semi-relativistic cross sections of about 40 % is obtained by the ionisation from the $4p$ subshell.

The influence of the EA channels corresponding to the strongest excitations is presented in Figure 8. At the lower temperatures, the largest contribution to the EA process for the ground level comes from

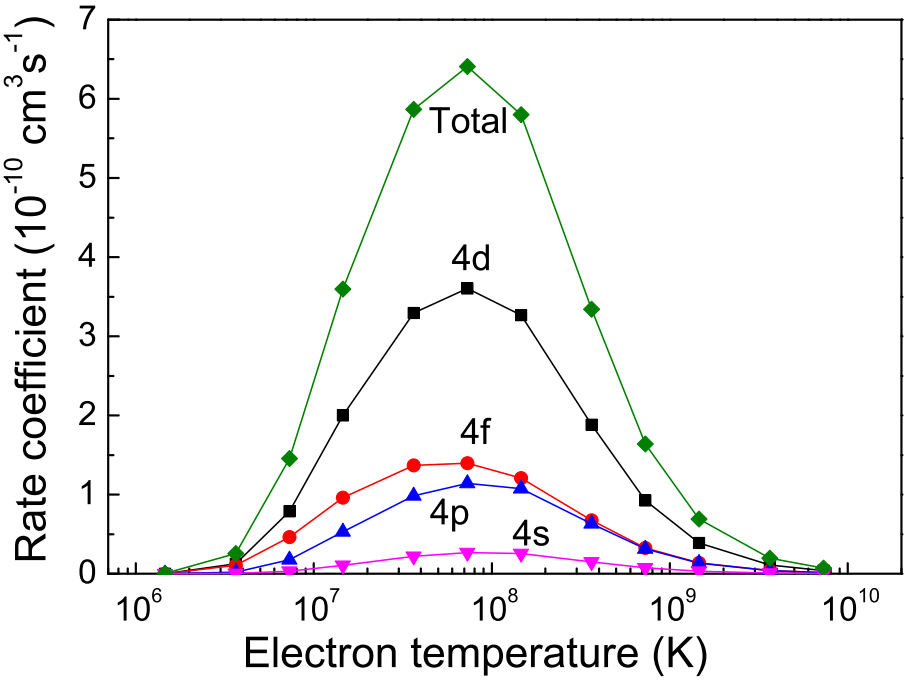

Figure 7: The DI rate coefficients for electron-impact single ionisation from the ground level of the W^{26+} ion.

the $4d^9 4f^2 8d$, $4d^9 4f^2 8g$ and $4p^5 4f^2 6p$ configurations (Figure 8 (a)). At the medium temperatures, the excitations to the $4d^9 4f^2 8d$, $4d^9 4f^2 8f$ and $4d^9 4f^2 8g$ configurations dominate. At the higher temperatures, the excitations to $4d^9 4f^2 8f$, $4p^5 4f^2 6d$ and $4d^9 4f^2 8g$ has the largest influence. Since 56 configurations having energy levels above the ionisation threshold are dealt with, the contribution from weaker excitations for shells with $n \leqslant 8$, not presented in Figure 8 (a). It should be noted that those weaker excitations are equal to about 40 % of total contributions.

The configurations providing the strongest EA channels for the ground level, except for $4p^5 4f^2 6p$ which have energy levels above the single ionisation threshold. The $4d^9 4f^2 7d$, $4d^9 4f^2 7f$ and $4d^9 4f^2 7g$ configurations have energy levels that straddle the ionisation threshold. It is the main reason why the EA rate coefficients for the excitations to energy levels of these configurations are diminished. This explains the large contribution from the $4d^9 4f^2 8d$, $4d^9 4f^2 8f$ and $4d^9 4f^2 8g$ configurations, because these are the lowest configurations having all energy levels above the ionisation threshold.

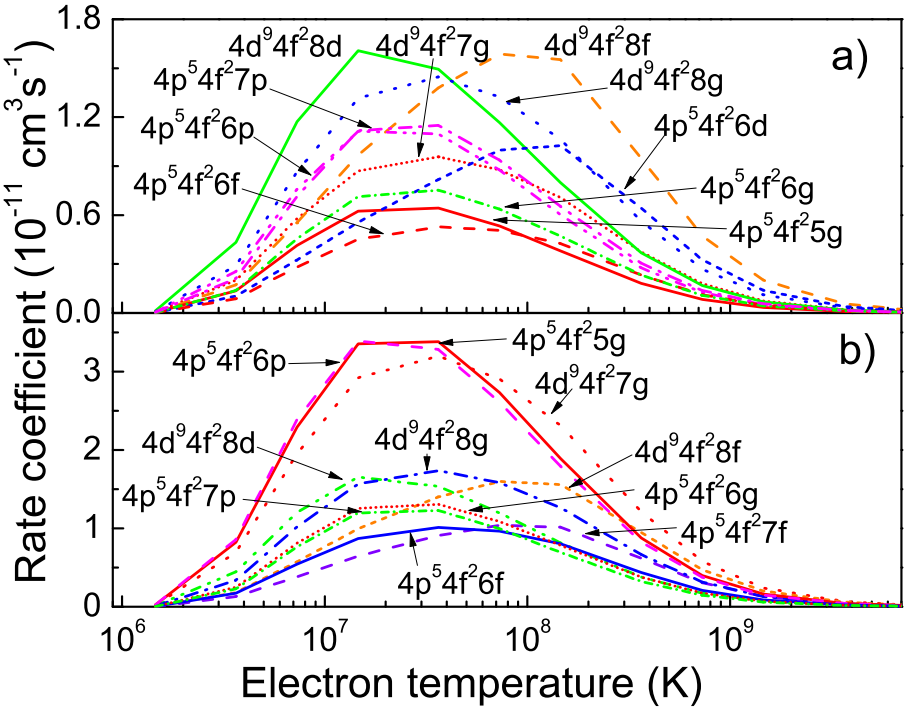

Figure 8: Configurations with the largest contribution to the EA rate coefficients for excitations to shells with $n \leqslant 8$ for (a) the lowest level and (b) the highest level of the ground configuration.

Another important finding is the variation of the EA MRC for excitations from the $4l$ ($l = 0 - 2$) shells up to shells with the principal quantum number $n \leqslant 8$ and the orbital quantum number $l \leqslant 6$ as shown in Figure 9. It can be seen that the rate coefficients for the various ground configuration levels differ approximately by 60 %.

For the highest level of the ground configuration, the largest values for EA MRC arise from $4p^54f^26p$, $4p^54f^25g$ and $4d^94f^27g$ (Figure 8 (b)). The MRC values are approximately 50 % higher compared to the strongest excitations from the lowest level of the ground configuration (Figure 8 (a)).

The contribution of the EA channels to MRC for excitations to the shells with $9 \leqslant n \leqslant 25$ (Figure 10) is lower than for $n \leqslant 8$ (Figure 8). Furthermore, the EA MRC for excitations to the shells with $9 \leqslant n \leqslant 25$ are less dependent on the initial level. This can be explained by the fact that all energy levels of configurations originating from the excitations to

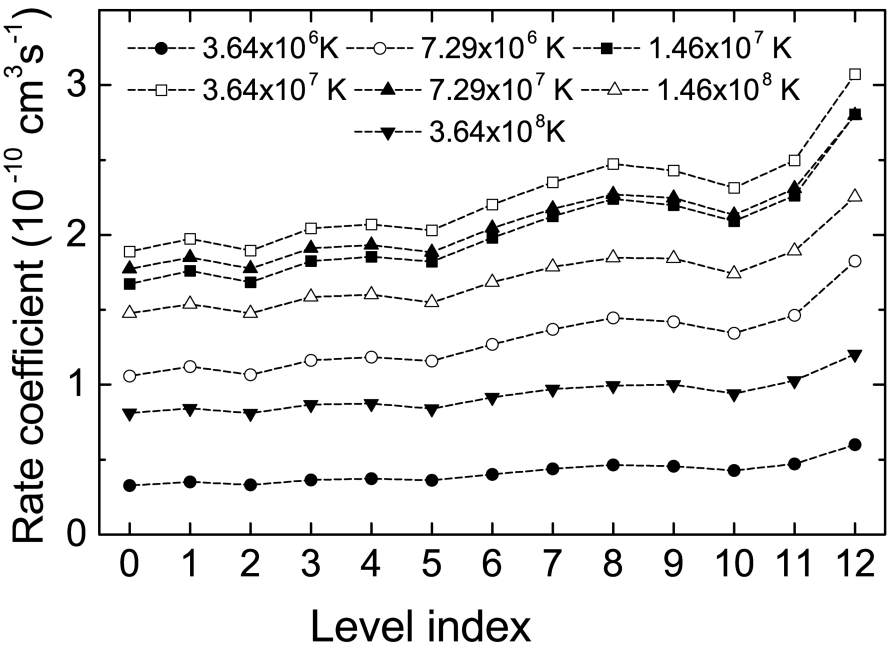

Figure 9: The EA rate coefficients for excitations from the ground configuration levels of the W^{26+} ion up to the shells with $n \leqslant 8$ and $l \leqslant 6$. The lines are guides to the eye only.

the shells with $9 \leqslant n \leqslant 25$ are above the ionisation threshold, and this leads to less prominent variation in MRC compared to the $n \leqslant 8$ case. Nevertheless, the highest level of the ground configuration provides the largest values for MRC.

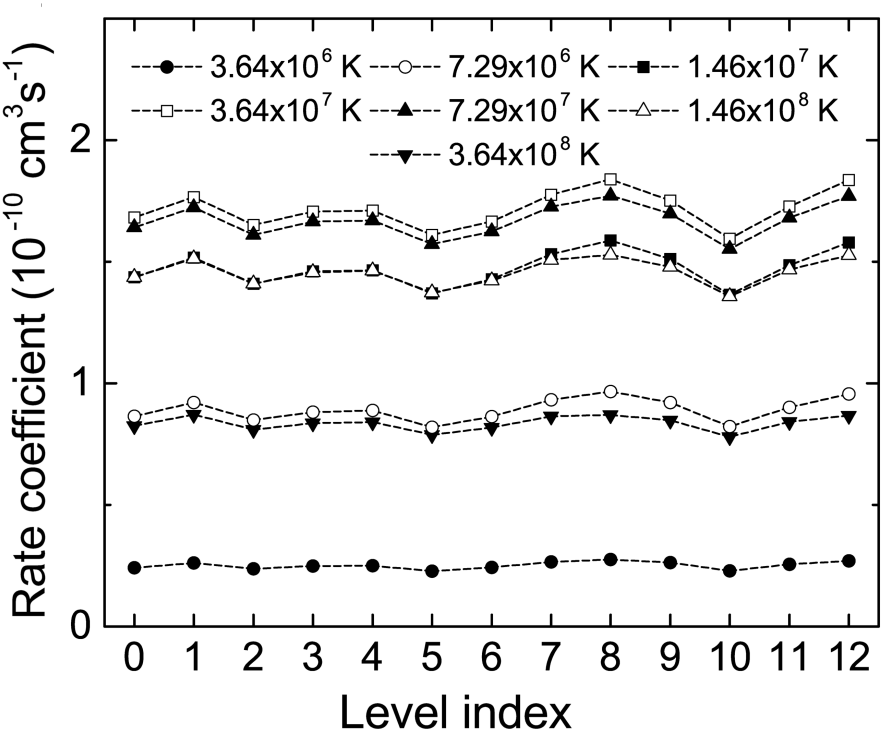

Figure 10: The EA rate coefficients for excitations from the ground configuration levels of the W^{26+} ion up to the shells with $9 \leqslant n \leqslant 25$ and $l \leqslant 6$. The lines are guides to the eye only.

In summary, the excitations to the higher-nl shells in the W^{26+} ion are important for plasma rate coefficients. The excitations to the higher-nl shells ($n > 8$) contribute ∼45 % to the total MRC for the levels of the ground configuration. Moreover, the study has to include level-to-level data since the MRC coefficients for the EA process can differ up to ∼60 %. The plasma modelling parameters have to be adjusted by our MRC values.

W^{5+} Ion [A5]

We calculated W^{5+} ion's energetically lowest configurations level energies and configurations produced by the strongest excitations from the ground configuration. We identified other ionisation paths, such as collisional single-ionisation of W^{5+} to configurations of W^{6+} ions with levels that are below the double-ionisation threshold. Another path is the

reachability of energetically lowest levels of W^{7+} from W^{5+} by the direct double ionisation process. These results are presented in Figure 11.

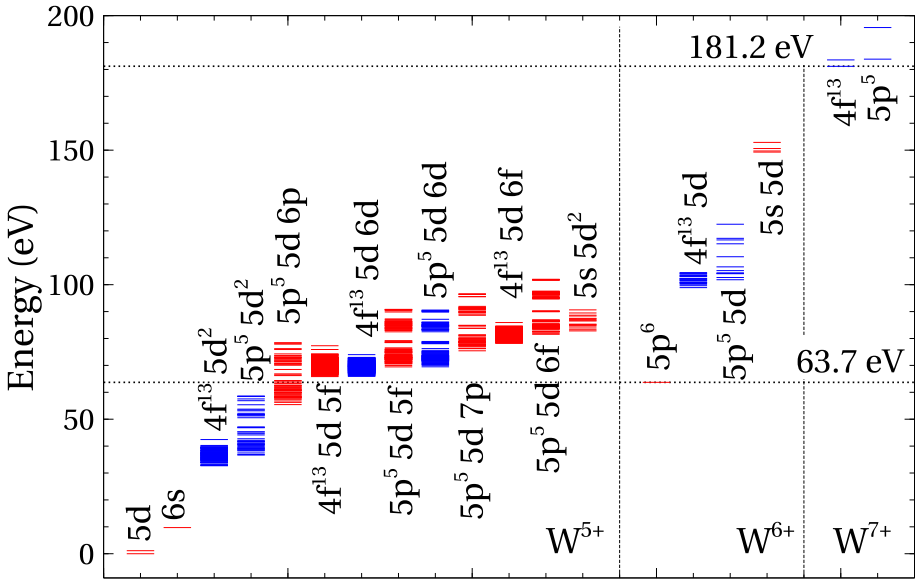

Figure 11: Energy levels of the main configurations of W^{5+}, W^{6+} and W^{7+} ions relevant for the present study. Even configurations are shown in red, odd configurations in blue. Dotted horizontal lines mark the thresholds for single and double ionisation of W^{5+}, respectively.

As it is seen from Figure 11 that energy levels of the $5p^5 5d 6p$ configurations straddle the ground level of the W^{6+} ion. Furthermore, the $5p^5 5d\,6s$ configuration (not shown in the figure) has energy levels surrounding the ionisation threshold. These autoionising configurations can easily provide inaccurate results if contributions to the total single-ionisation cross sections are calculated using the configuration-averaged approach. In such cases, level-to-level calculations are needed. It is interesting to note that DI from the $4d$ subshell in W^{5+} only contributes to indirect processes that end up in double ionisation. The fact is that the energy levels of the $4d^9 5d$ configuration are above the ionisation threshold of the W^{6+} ion, and levels in the $4d^9 5d$ configuration can decay via radiative and Auger transitions. The fluorescence yields were calculated in the single-configuration approximation to estimate this decay path. The yield does not exceed 2×10^{-4} for those levels. Therefore, they primarily produce the final charge state W^{7+}.

There are 29 levels which belong to the $4f^{13}5d^2$ configuration, 8

levels from the $5p^5 5d^2$ configuration and 28 levels of $4f^{13}\,5d\,6s$ configuration with sufficiently long lifetimes. These levels were calculated with consideration of electric dipole, quadrupole and octupole, as well as magnetic dipole and quadrupole transitions from the levels of the $5d$, $6s$, $4f^{13}5d^2$, $5p^5 5d^2$ and $4f^{13}\,5d\,6s$ configurations. Furthermore, the excitation $5d \rightarrow 6s$ from the ground configuration of the W^{5+} ion provides the lowest excited configuration, which can decay via very weak electric quadrupole transitions. The other three configurations have many levels which decay via electric dipole transitions. However, selection rules for the electric dipole transitions limit the possible decay paths for some levels, and they feature long lifetimes.

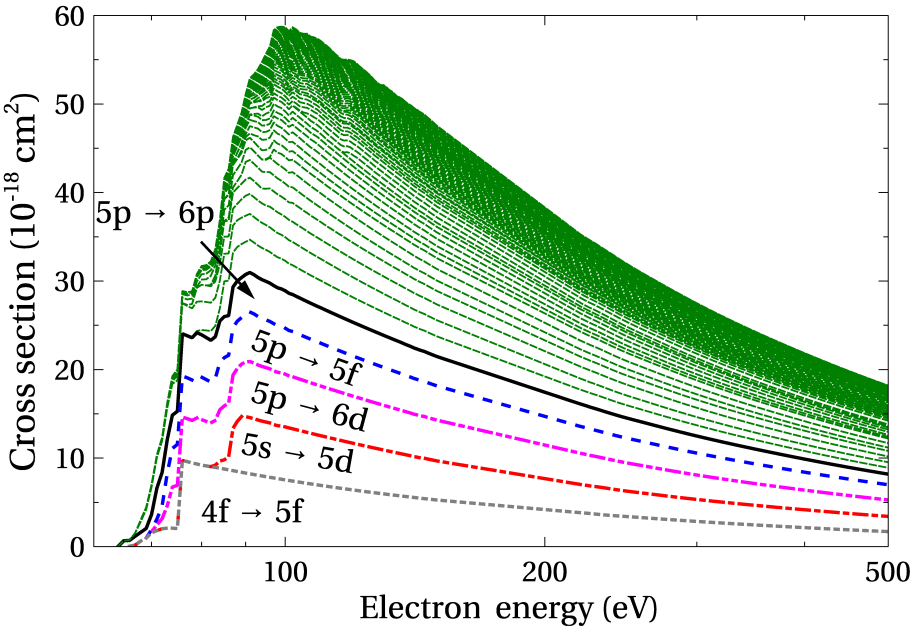

Figure 12: Accumulated cross sections of the EA channels contributing to the ionisation of the ground level of W^{5+}. The strongest EA contributions are individually identified.

The cross sections of the strongest EA channels for the ground level of W^{5+} are shown in Figure 12. Five transitions ($4f \rightarrow 5f$, $5s \rightarrow 5d$, $5p \rightarrow 6d$, $5p \rightarrow 5f$, $5p \rightarrow 6p$) produce approximately half of the total EA cross sections. Only one ($5p \rightarrow 6d$) of the presented excitations leads to an odd-parity configuration. All the final configurations of the strongest excitations have energy levels above the single-ionisation threshold with

the exception of the $5p^5\,5d\,6p$ configuration whose levels are partly below that threshold (Figure 11).

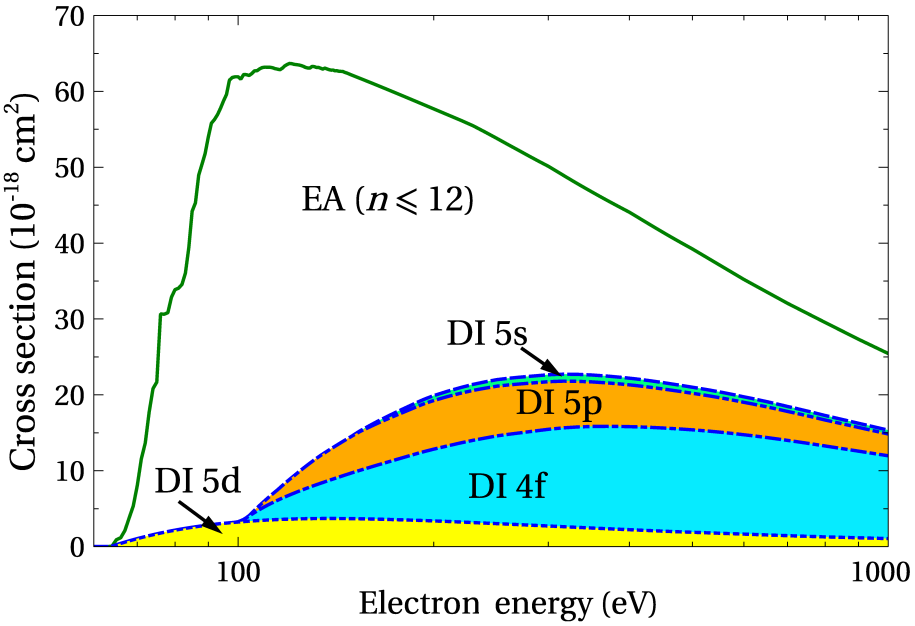

Figure 13: Accumulated electron-impact single-ionisation cross sections for ground-level W^{5+}. The shaded areas show contributions of DI processes from different subshells.

The contributions of direct and indirect processes of ionisation by electron impact from the ground configuration are shown in Figure 13. The strongest DI contribution is associated with the ionisation of the $4f$ subshell, which has the largest number of electrons. Indirect processes dominate over DI at the lower electron energies. It should be noted that EA dominates over DI, particularly for the excited initial configurations. The largest EA contribution originates from the $5p \rightarrow 5d$ promotion. This is true for all the considered initial configurations, except the $5d$ configuration. The reason for this exception becomes obvious when one looks back at Figure 11: all levels of the excited $5p^5 5d^2$ configuration are lower than the ionisation threshold. The $5p \rightarrow 5d$ excitation cross sections are much larger than the DI cross sections, which are very similar for all presented configurations. This confirms the expectations expressed previously by Stenke *et al.*

The present experimental absolute cross sections and the fine-step energy scan are compared to theoretical single-ionisation cross sections

for the two levels of the ground configuration in Figure 14. The calculated

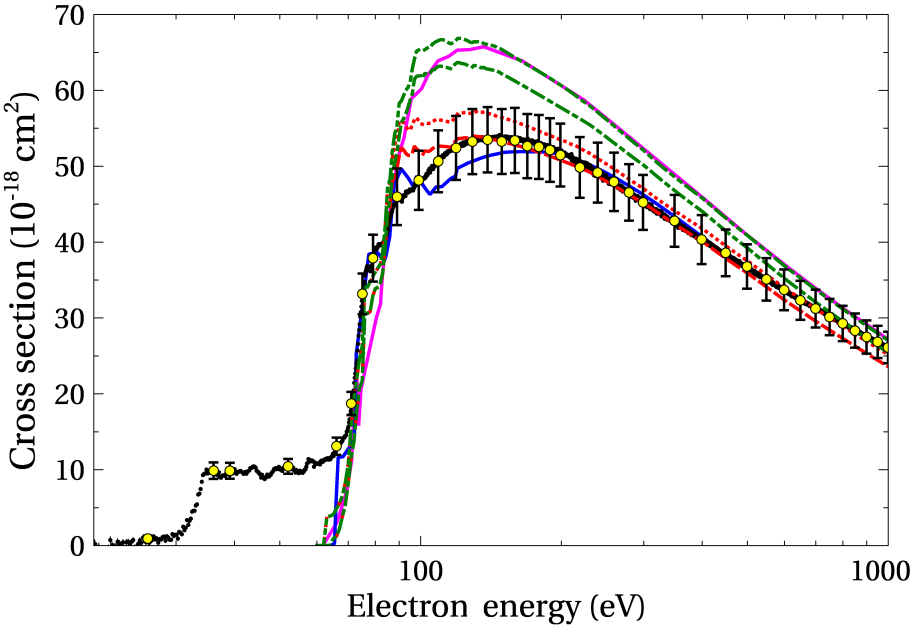

Figure 14: Comparison of the present experimental data [74] to the theoretical calculations for single ionisation from the ground levels of W^{5+}. Circles with light shading (yellow) and associated total error bars represent experimental absolute cross sections. The small black dots with statistical error bars of the size of the symbols are the result of the fine-step energy scan. Present theoretical results including DI and EA for excitations with $n \leqslant 7$ are shown by the dashed (red) line for the $5d^2D_{3/2}$ ground level and by the dotted (red) line for the $5d^2D_{5/2}$ level. The dash-dotted (green) line represents the $5d^2D_{3/2}$ cross section and the dash-dot-dotted (green) line means the $5d^2D_{5/2}$ cross section, both contain EA contributions associated with excitations up to $n = 12$. The upper solid (magenta) line represents the calculation performed by Zhang *et al.* [34] that includes EA contributions up to $n = 10$. The CADW results obtained by Pindzola and Griffin [32] including excitations with $n \leqslant 6$ are represented by the solid (blue) line that is close to the experimental data points.

cross sections for ionisation from the lower and upper levels of the $5d$ ground configuration (levels 0 and 1, respectively, in Table 2) are very similar to one another, with the cross section for the $5d^2D_{5/2}$ excited level slightly higher than that of the $5d^2D_{3/2}$ ground level.

Table 2: Long-lived levels and their lifetimes for W^{5+} ion. Only levels with lifetimes exceeding 10^{-5} s are presented. Note that $a \pm b \equiv a \times 10^{\pm b}$.

Configuration	Index	Level	J	Energy (eV)	Lifetime (s)
$5d$	0	$5d_-$	3/2	0	–
	1	$5d_+$	5/2	1.122	1.25−1
$6s$	2	$6s_+$	1/2	9.681	3.15−4
$4f^{13}5d^2$	6	$4f_+^7\ 5d_-^2\ (2)$	11/2	32.624	6.08+3
	7	$4f_+^7\ 5d_-^2\ (2)$	9/2	32.787	1.49+0
	8	$4f_+^7\ 5d_-\ 2\ 5d_+$	9/2	33.294	1.13−1
	10	$4f_+^7\ 5d_-\ 5\ 5d_+$	13/2	33.479	1.21−1
	14	$4f_+^7\ 5d_-\ 3\ 5d_+$	11/2	33.728	9.14−2
	16	$4f_+^7\ 5d_-\ 5\ 5d_+$	15/2	34.111	4.37−1
	17	$4f_+^7\ 5d_-\ 5\ 5d_+$	9/2	34.225	4.30−2
	19	$4f_+^7\ 5d_-\ 5\ 5d_+$	11/2	34.448	1.27−1
	22	$4f_+^7\ 5d_+^2\ (4)$	13/2	34.519	1.73−1
	26	$4f_-^5\ 5d_-^2\ (2)$	9/2	34.919	1.25−2
	27	$4f_+^7\ 5d_-\ 3\ 5d_+$	9/2	34.985	5.47−2
	31	$4f_+^7\ 5d_+^2\ (4)$	15/2	35.345	5.00−2
	32	$4f_+^7\ 5d_-\ 4\ 5d_+$	11/2	35.368	3.18−2
	35	$4f_+^7\ 5d_-\ 4\ 5d_+$	9/2	35.374	3.95−2
	40	$4f_-^5\ 5d_-\ 4\ 5d_+$	11/2	35.945	8.63−3
	41	$4f_+^7\ 5d_+^2\ (2)$	9/2	35.992	2.82−2
	44	$4f_-^5\ 5d_-\ 2\ 5d_+$	9/2	36.274	9.19−3
	45	$4f_+^7\ 5d_+^2\ (2)$	11/2	36.282	3.54−2
	47	$4f_+^7\ 5d_+^2\ (4)$	13/2	36.424	2.08−2
	51	$4f_-^5\ 5d_-\ 4\ 5d_+$	13/2	36.735	1.07−2
	53	$4f_-^5\ 5d_-\ 2\ 5d_+$	9/2	36.799	1.52−2
	56	$4f_+^7\ 5d_+^2\ (4)$	9/2	36.973	1.51−2
	59	$4f_+^7\ 5d_+^2\ (2)$	11/2	37.226	1.38−2
	62	$4f_-^5\ 5d_+^2\ (4)$	11/2	37.345	1.11−2
	64	$4f_-^5\ 5d_+^2\ (4)$	9/2	37.762	6.77−3
	68	$4f_-^5\ 5d_+^2\ (4)$	13/2	38.022	6.78−3
	75	$4f_-^5\ 5d_+^2\ (2)$	9/2	38.912	7.03−3

Continued on next page

Table 2: (continued)

Configuration	Index	Level	J	Energy (eV)	Lifetime (s)
	79	$4f_-^5\ 5d_+^2$ (4)	11/2	39.166	6.91−3
	81	$4f_-^5\ 5d_+^2$ (4)	9/2	39.552	6.98−3
$5p^5 5d^2$	87	$5p_+^3\ 5d_-\ 1\ 5d_+$	7/2	38.134	7.30−5
	89	$5p_+^3\ 5d_-\ 2\ 5d_+$	9/2	38.712	1.49−1
	91	$5p_+^3\ 5d_+^2$ (4)	11/2	39.034	3.58−1
	98	$5p_+^3\ 5d_+^2$ (4)	9/2	40.760	1.13−2
	99	$5p_+^3\ 5d_-\ 3\ 5d_+$	11/2	41.002	4.76−2
	105	$5p_+^3\ 5d_-\ 2\ 5d_+$	9/2	42.641	1.66−2
	116	$5p_-\ 5d_-\ 2\ 5d_+$	9/2	51.551	6.68−5
	121	$5p_-\ 5d_+^2$ (4)	9/2	53.355	6.57−5
$4f^{13}5d\,6s$	129	$4f_+^7\ 5d_-\ 2\ 6s_+$	5/2	43.657	2.07−4
	131	$4f_+^7\ 5d_-\ 5\ 6s_+$	9/2	44.397	2.02−4
	132	$4f_+^7\ 5d_-\ 5\ 6s_+$	11/2	44.583	1.73−4
	133	$4f_+^7\ 5d_-\ 3\ 6s_+$	7/2	44.859	1.66−4
	134	$4f_+^7\ 5d_-\ 3\ 6s_+$	5/2	45.085	1.73−4
	135	$4f_+^7\ 5d_-\ 4\ 6s_+$	9/2	45.261	1.54−4
	136	$4f_+^7\ 5d_-\ 4\ 6s_+$	7/2	45.315	1.68−4
	137	$4f_+^7\ 5d_+\ 6\ 6s_+$	13/2	45.361	1.70−4
	140	$4f_+^7\ 5d_+\ 2\ 6s_+$	5/2	46.018	1.62−4
	142	$4f_+^7\ 5d_+\ 6\ 6s_+$	11/2	46.246	1.45−4
	143	$4f_+^7\ 5d_+\ 4\ 6s_+$	9/2	46.258	1.56−4
	144	$4f_+^7\ 5d_+\ 3\ 6s_+$	7/2	46.263	1.64−4
	145	$4f_+^7\ 5d_+\ 5\ 6s_+$	11/2	46.583	1.30−4
	146	$4f_-^5\ 5d_-\ 4\ 6s_+$	7/2	46.683	1.79−4
	147	$4f_+^7\ 5d_+\ 3\ 6s_+$	5/2	47.001	1.32−4
	148	$4f_-^5\ 5d_-\ 4\ 6s_+$	9/2	47.034	1.73−4
	150	$4f_-^5\ 5d_-\ 2\ 6s_+$	5/2	47.231	1.78−4
	151	$4f_+^7\ 5d_+\ 4\ 6s_+$	7/2	47.269	1.30−4
	153	$4f_+^7\ 5d_+\ 5\ 6s_+$	9/2	47.455	1.30−4
	154	$4f_-^5\ 5d_-\ 3\ 6s_+$	5/2	47.781	1.49−4
	156	$4f_-^5\ 5d_-\ 3\ 6s_+$	7/2	47.945	1.59−4
	158	$4f_-^5\ 5d_+\ 5\ 6s_+$	11/2	48. 060	1.73−4

Continued on next page

Table 2: (continued)

Configuration	Index	Level	J	Energy (eV)	Lifetime (s)
	159	$4f_-^5\ 5d_+\ 2\ 6s_+$	5/2	48.377	1.56−4
	160	$4f_-^5\ 5d_+\ 3\ 6s_+$	7/2	48.713	1.52−4
	161	$4f_-^5\ 5d_+\ 4\ 6s_+$	9/2	48.727	1.41−4
	163	$4f_-^5\ 5d_+\ 5\ 6s_+$	9/2	49.089	1.36−4
	165	$4f_-^5\ 5d_+\ 3\ 6s_+$	5/2	49.605	1.27−4
	167	$4f_-^5\ 5d_+\ 4\ 6s_+$	7/2	49.851	1.29−4

Theoretical cross sections corresponding to excitations to shells with principal quantum numbers up to $n = 7$ and $n = 12$, respectively, are shown for comparison. It is evident from the data that there is a difference of ∼20 % between the $n = 7$ and the $n = 12$ results at the peak of the cross section. Previous studies for much more highly charged tungsten ions W^{18+} [64], W^{25+} [72], W^{26+} [63] and W^{27+} [59,60] demonstrated the importance of excitations to higher shells ($n > 12$), which were needed to reach convergence of the EA cross sections, while contributions with $n > 12$ are found to be negligible for the ionisation of W^{5+}. The deeper reason for the different levels of importance of high-n contributions to the ionisation cross sections of W^{5+} and W^{q+} with $q \geq 18$ is not known. The effect is probably associated with the very different charge states and the resulting different electronic structures of these ions.

The comparisons of theory and the experiment [74], similar to the one in Figure 14, have been presented previously [32–34]. The calculations were restricted to the ground configuration and ground level, respectively. In spite of this restriction, the agreement with the experimental cross section at energies beyond about 70 eV was interpreted, although the experimental data are not for the ground level or ground configuration, but for a mixture of ions in the ground state and in metastable levels. The pioneering CADW calculations by Pindzola and Griffin [32], with excitations up to shells with $n = 7$ and orbital quantum numbers $l = 4$ for indirect ionisation processes, showed very good agreement with the measurements reported by Stenke *et al.* [30] at energies beyond the ground-state ionisation potential. These data are slightly below our results for the $n \leqslant 7$ case. It should be noted that our study also includes excitations

to shells with $l = 5$ and $l = 6$, but their contribution is negligible. It is known that the CADW approach can lead to inaccurate probabilities of Auger transitions for overlapping initial and final configurations [75, 76]. Moreover, the pseudo-relativistic approach has been used by Pindzola and Griffin to obtain wave functions for the structure and scattering calculations, while our calculations employ the DFS method. Furthermore, our study includes radiative damping of the autoionising states. This leads to the diminishing of the total ionisation cross sections by ∼14 % at the peak. Instead, the previous CADW treatment found that the branching ratio for autoionisation is approximately equal to one [32].

In Figure 14 we also compare our data with the recent LLDW calculations by Zhang *et al.* [34]. The minor deviations of the results of Zhang *et al.* from our theoretical cross section can be explained by slight differences between both theoretical approaches. In their calculations of EA cross sections, Zhang *et al.* [34] considered excitations into levels with $n \leq 10$. In addition, in the present work, slightly higher principal quantum numbers of up to $n = 12$ are taken into account. The treatment of DI cross sections differs in that Zhang *et al.* optimised their continuum wave functions on the primary ion while, here, we used the potential of the product ion.

In summary, the EA channels corresponding to excitations to the higher-nl shells ($n < 7$) adds ∼15 % to the total single ionisation cross sections. The contribution from the excitations to the shells with orbital quantum numbers $l = 5$ and $l = 6$ is negligible. The main EA channels correspond to excitations to the shells with $l = 2$. Furthermore, the second strongest EA channel corresponds to the excitations to the shells with $l = 3$.

Fe^{3+} Ion [A4]

Recent calculations for the ground configuration of the Fe^{3+} ion [77] using the CADW approximation provided overestimated data compared to the measurements [78]. These calculations included excitations from the $3s$ and $3p$ subshells up to shells with the principal quantum number $n \leqslant 12$. The discrepancy of ∼25 % was obtained for the peak value. What is more, the previous level-to-level DW (LLDW) calculations [79] using the Dirac-Fock-Slater (DFS) approach demonstrated quite good

agreement with the CADW data [77, 80, 81].

The ground [Ne] $3s^2 3p^6 3d^5$ configuration has 37 energy levels, while the first excited [Ne] $3s^2 3p^6 3d^4 4s$ configuration corresponds to 62 energy levels (Table 3).

Table 3: Lifetimes of the energy levels of the Fe^{3+} $3p^6 4d^5$ and $3p^6 4d^4 4s$ configurations. Closed inner subshells are omitted in the notations of the levels. The levels are identified by the largest weight in the expansion of wave function. Energies are given relative to the ground level energy. J is the total angular momentum quantum number. Note that $a \pm b = a \times 10^{\pm b}$.

Configuration	Index	Level	J	Energy (eV)	Lifetime (s)
$3p^6 4d^5$	0	$3d_-^2(2)3d_+^3(9/2)$	5/2	0.000	∞
	1	$3d_-^2(2)3d_+^3(9/2)$	11/2	4.202	∞
	2	$3d_-^2(2)3d_+^3(3/2)$	5/2	4.205	1.849+5
	3	$3d_-^2(2)3d_+^3(9/2)$	9/2	4.206	5.714+6
	4	$3d_-^2(2)3d_+^3(9/2)$	7/2	4.207	7.901+6
	5	$3d_+(5/2)$	5/2	4.834	5.517–1
	6	$3d_-^2(2)3d_+^3(5/2)$	3/2	4.844	8.460–1
	7	$3d_-^2(2)3d_+^3(5/2)$	1/2	4.856	6.533+3
	8	$3d_-^2(2)3d_+^3(9/2)$	7/2	5.248	1.920+1
	9	$3d_-^2(2)3d_+^3(3/2)$	1/2	5.262	8.743+0
	10	$3d_-(3/2)3d_+^4(2)$	3/2	5.269	8.284+0
	11	$3d_-(3/2)3d_+^4(2)$	5/2	5.271	7.709+0
	12	$3d_-^2(2)3d_+^3(9/2)$	11/2	5.980	1.372+2
	13	$3d_-^2(2)3d_+^3(9/2)$	13/2	5.983	4.373+3
	14	$3d_+(5/2)$	5/2	6.724	7.919–1
	15	$3d_-^2(2)3d_+^3(3/2)$	3/2	6.806	1.812+0
	16	$3d_-^2(2)3d_+^3(5/2)$	7/2	6.941	9.821–1
	17	$3d_-^2(2)3d_+^3(5/2)$	5/2	7.042	9.014–1
	18	$3d_-^2(0)3d_+^3(9/2)$	9/2	7.076	8.056–1
	19	$3d_-(3/2)3d_+^4(4)$	7/2	7.084	8.331–1
	20	$3d_-^2(2)3d_+^3(5/2)$	3/2	7.106	7.323–1
	21	$3d_+^5(5/2)$	5/2	7.109	6.846–1
	22	$3d_-^2(2)3d_+^3(5/2)$	9/2	7.361	1.591+0

Continued on next page

Table 3: continued.

Configuration	Index	Level	J	Energy (eV)	Lifetime (s)
	23	$3d_-(3/2)3d_+^4(4)$	11/2	7.392	7.797–1
	24	$3d_-^2(2)3d_+^3(3/2)$	7/2	7.632	8.911+0
	25	$3d_-(3/2)3d_+^4(4)$	9/2	7.664	4.628+0
	26	$3d_-^2(2)3d_+^3(3/2)$	5/2	8.229	3.273+0
	27	$3d_-^2(2)3d_+^3(3/2)$	7/2	8.229	3.234+0
	28	$3d_-^3(3/2)3d_+^2(2)$	1/2	9.121	8.949–1
	29	$3d_-^2(0)3d_+^3(3/2)$	3/2	10.067	4.713–1
	30	$3d_-^2(2)3d_+^3(5/2)$	5/2	10.067	3.778–1
	31	$3d_-^2(2)3d_+^3(5/2)$	7/2	11.097	5.783–2
	32	$3d_-^2(0)3d_+^3(9/2)$	9/2	11.099	5.866–2
	33	$3d_-^2(2)3d_+^3(5/2)$	1/2	13.626	1.930–2
	34	$3d_-^2(0)3d_+^3(3/2)$	3/2	13.626	1.946–2
	35	$3d_-(3/2)3d_+^4(0)$	3/2	14.689	2.186–2
	36	$3d_-^2(0)3d_+^3(5/2)$	5/2	14.694	2.191–2
$3p^6 3d^4 4s$	37	$3d_-^2(2)3d_+^2(2)4s_+(1/2)$	1/2	14.648	5.247–4
	38	$3d_-^3(3/2)3d_+(5/2)4s_+(1/2)$	3/2	14.675	5.209–4
	39	$3d_-^2(2)3d_+^2(4)4s_+(1/2)$	5/2	14.716	5.157–4
	40	$3d_-^2(2)3d_+^2(4)4s_+(1/2)$	7/2	14.765	5.099–4
	41	$3d_-(3/2)3d_+^3(9/2)4s_+(1/2)$	9/2	14.816	5.043–4
	42	$3d_-^3(3/2)3d_+(5/2)4s_+(1/2)$	1/2	16.502	3.024–4
	43	$3d_-^2(2)3d_+^2(4)4s_+(1/2)$	3/2	16.544	3.004–4
	44	$3d_-^2(2)3d_+^2(4)4s_+(1/2)$	5/2	16.601	2.979–4
	45	$3d_-(3/2)3d_+^3(9/2)4s_+(1/2)$	7/2	16.663	2.957–4
	46	$3d_-^3(3/2)3d_+(5/2)4s_+(1/2)$	7/2	17.846	4.565–4
	47	$3d_-^2(2)3d_+^2(4)4s_+(1/2)$	9/2	17.870	4.525–4
	48	$3d_-^2(2)3d_+^2(4)4s_+(1/2)$	11/2	17.899	4.483–4
	49	$3d_-(3/2)3d_+^3(9/2)4s_+(1/2)$	13/2	17.926	4.441–4
	50	$4s_+(1/2)$	1/2	18.021	4.655–4
	51	$3d_-^3(3/2)3d_+(5/2)4s_+(1/2)$	3/2	18.154	4.552–4
	52	$3d_-^2(2)3d_+^2(2)4s_+(1/2)$	3/2	18.289	3.865–4
	53	$3d_-^2(2)3d_+^2(2)4s_+(1/2)$	5/2	18.293	3.871–4
	54	$3d_-^2(2)3d_+^2(2)4s_+(1/2)$	7/2	18.301	3.835–4

Continued on next page

Table 3: continued.

Configuration	Index	Level	J	Energy (eV)	Lifetime (s)
	55	$3d_-^3(3/2)3d_+(5/2)4s_+(1/2)$	9/2	18.304	3.806–4
	56	$3d_+^4(2)4s_+(1/2)$	5/2	18.316	4.466–4
	57	$3d_-^2(2)3d_+^2(2)4s_+(1/2)$	5/2	18.603	3.984–4
	58	$3d_-^2(2)3d_+^2(2)4s_+(1/2)$	7/2	18.635	3.954–4
	59	$3d_-(3/2)3d_+^3(9/2)4s_+(1/2)$	9/2	18.662	3.924–4
	60	$3d_-(3/2)3d_+^3(9/2)4s_+(1/2)$	11/2	18.686	3.887–4
	61	$3d_-^2(2)3d_+^2(4)4s_+(1/2)$	9/2	18.972	2.643–4
	62	$3d_-^2(2)3d_+9+^2(4)4s_+(1/2)$	11/2	19.032	2.637–4
	63	$3d_-^3(3/2)3d_+(5/2)4s_+(1/2)$	1/2	19.186	2.748–4
	64	$3d_-(3/2)3d_+^3(5/2)4s_+(1/2)$	3/2	19.398	2.702–4
	65	$3d_-^3(3/2)3d_+(5/2)4s_+(1/2)$	7/2	19.402	2.959–4
	66	$3d_-^2(2)3d_+^2(2)4s_+(1/2)$	5/2	19.414	2.988–4
	67	$3d_-^2(2)3d_+^2(4)4s_+(1/2)$	13/2	19.658	3.314–4
	68	$3d_-(3/2)3d_+^3(9/2)4s_+(1/2)$	11/2	19.667	3.345–4
	69	$3d_-(3/2)3d_+^3(9/2)4s_+(1/2)$	7/2	19.673	2.597–4
	70	$3d_-^3(3/2)3d_+(5/2)4s_+(1/2)$	5/2	19.679	2.602–4
	71	$3d_-^2(2)3d_+^2(2)4s_+(1/2)$	3/2	19.699	2.593–4
	72	$3d_-(3/2)3d_+^3(3/2)4s_+(1/2)$	1/2	19.717	2.579–4
	73	$3d_-^2(2)3d_+^2(2)4s_+(1/2)$	7/2	19.733	2.597–4
	74	$3d_-(3/2)3d_+^3(9/2)4s_+(1/2)$	9/2	19.788	2.278–4
	75	$3d_+^4(4)4s_+(1/2)$	9/2	19.899	3.657–4
	76	$3d_+^4(4)4s_+(1/2)$	7/2	19.913	3.234–4
	77	$3d_-(3/2)3d_+^3(3/2)4s_+(1/2)$	1/2	20.630	2.962–4
	78	$3d_-(3/2)3d_+^3(9/2)4s_+(1/2)$	5/2	20.779	2.523–4
	79	$3d_-(3/2)3d_+^3(3/2)4s_+(1/2)$	3/2	20.794	3.223–4
	80	$3d_+^4(2)4s_+(1/2)$	5/2	21.008	3.178–4
	81	$3d_+^4(2)4s_+(1/2)$	3/2	21.018	2.510–4
	82	$3d_-(3/2)3d_+^3(3/2)4s_+(1/2)$	7/2	21.882	2.395–4
	83	$3d_-(3/2)3d_+^3(3/2)4s_+(1/2)$	5/2	21.888	2.502–4
	84	$3d_-^2(0)3d_+^2(4)4s_+(1/2)$	9/2	22.691	1.577–4
	85	$3d_-^2(2)3d_+^2(0)4s_+(1/2)$	3/2	22.698	1.588–4
	86	$3d_-(3/2)3d_+^3(5/2)4s_+(1/2)$	7/2	22.701	1.587–4

Continued on next page

Table 3: continued.

Configuration Index	Level	J	Energy (eV)	Lifetime (s)
87	$3d_-(3/2)3d_+^3(5/2)4s_+(1/2)$	5/2	22.701	1.589–4
88	$3d_-^2(0)3d_+^2(2)4s_+(1/2)$	5/2	22.731	1.403–4
89	$3d_-(3/2)3d_+^3(5/2)4s_+(1/2)$	3/2	22.838	1.398–4
90	$3d_+^4(0)4s_+(1/2)$	1/2	22.891	1.401–4
91	$3d_-^2(0)3d_+^2(4)4s_+(1/2)$	7/2	23.800	1.693–4
92	$3d_-^2(2)3d_+^2(0)4s_+(1/2)$	5/2	23.808	1.657–4
93	$3d_-^2(0)3d_+^2(2)4s_+(1/2)$	3/2	23.867	1.843–4
94	$3d_-(3/2)3d_+^3(5/2)4s_+(1/2)$	1/2	23.988	1.844–4
95	$3d_-(3/2)3d_+^3(5/2)4s_+(1/2)$	9/2	24.049	1.614–4
96	$3d_-(3/2)3d_+^3(5/2)4s_+(1/2)$	7/2	24.058	1.606–4
97	$3d_-^2(0)3d_+^2(2)4s_+(1/2)$	5/2	27.098	1.234–4
98	$3d_-^2(0)3d_+^2(2)4s_+(1/2)$	3/2	27.099	1.232–4
99	$3d_-^2(0)3d_+^2(0)4s_+(1/2)$	1/2	30.504	9.564–5

The energy levels of the ground configuration calculated in the single-configuration approximation span the range of 14.69 eV. In comparison, the energy interval of 15.86 eV is occupied by the first excited configuration. The widths of energy levels provided by the NIST [82] correspond to 13.42 eV and 11.79 eV for the ground and first excited configurations, respectively. The obtained differences among our and NIST values can be explained by correlation effects, which are not considered in this case. The lowest level of the $3d^4 4s$ configuration is above the ground level by 14.61 eV. What is more, the single ionisation threshold is equal to 52.78 eV. The NIST recommended value for the single ionisation equals 54.91 $\pm$ 0.04eV, which is slightly above our value.

The energy levels and their lifetimes for the ground and first excited configurations are shown in Table 3. The probabilities of electric quadrupole and magnetic dipole transitions are calculated from these levels to determine the lifetimes. All these levels have lifetimes exceeding 10^{-5} s – amount of time that ions need to reach interaction region with electrons [83].

The EA process includes excitations from the $3s$, $3p$ and $3d$ subshells of the ground configuration where $n \leqslant 8$ and $l \leqslant 6$. For the ground

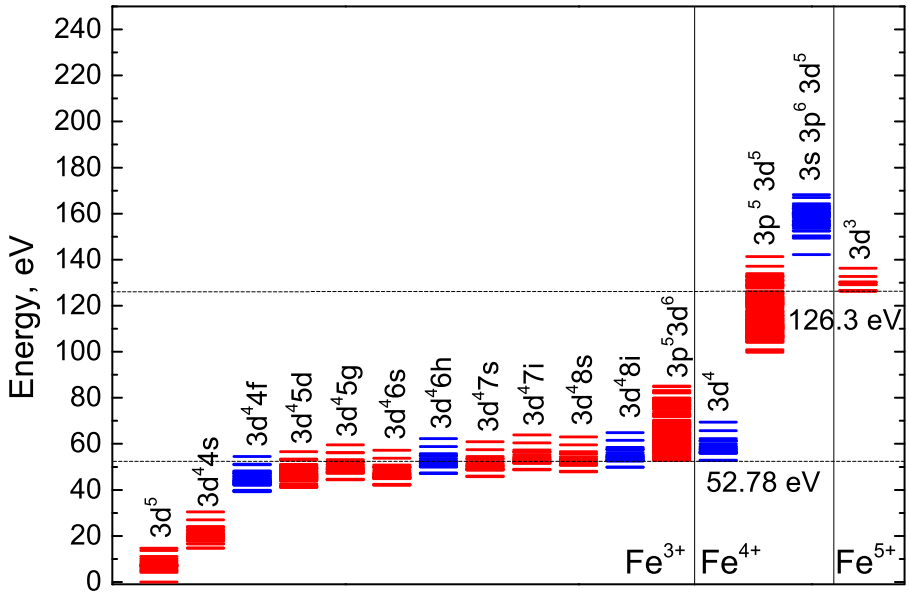

Figure 15: Energy levels of the ground configurations for the Fe^{3+}, Fe^{4+}, Fe^{5+} ions in addition to energy levels that straddle the single ionisation threshold. The first excited configuration of Fe^{3+} as well as $3p^5 3d^5$ and $3s\,3d^5$ of Fe^{4+} are also presented. For the Fe^{3+} $3d^4nl$ ($n = 5 - 8$) configurations, only the configurations with the lowest orbital quantum number l and the largest one are shown. Red – even configurations, blue – odd configurations.

configuration, the 89 excited configurations are produced to investigate radiative and Auger decay processes. It should be noted that not all generated configurations are autoionising.

Many configurations have energy levels that straddle the ionisation threshold (Figure 15). All of them correspond to excitations from the outer shell of the ground and the first excited configuration. The cross sections obtained from the lowest and highest levels of the ground configuration are compared to measurements in Figure 16. The theoretical values overestimate the experimental data at the peak of the cross sections. The overestimated values are also obtained for the highest level of the ground configuration at the lower energies of the impacting electron. The cross sections produced by ionisation from the ground level are below the single ionisation threshold's vicinity measurements. As it was noticed before [78], the onset of the experimental cross sections at ∼35 eV indicates the presence of metastable ions in the ion beam. What is

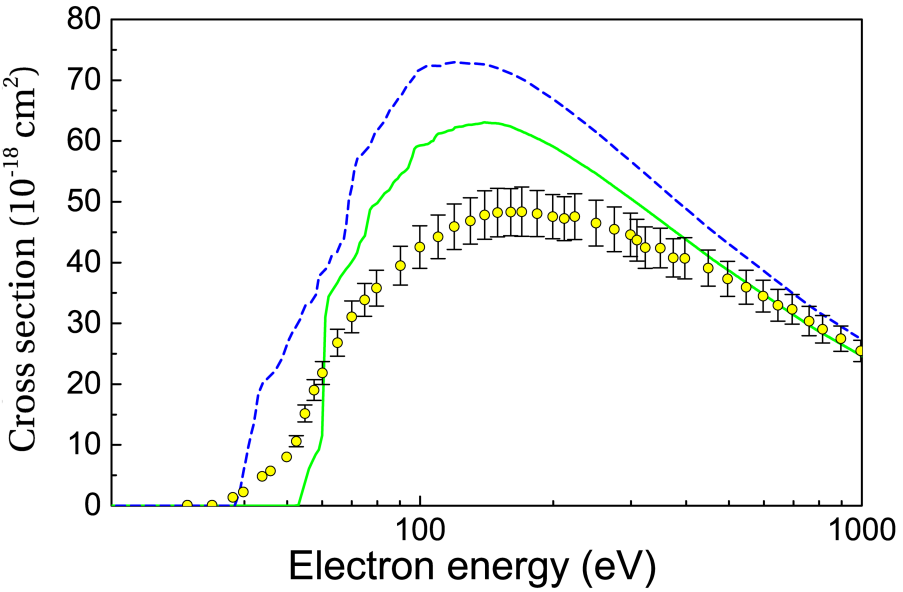

Figure 16: Single ionisation cross sections for the ground configuration levels: solid (green) line corresponds to level with index 0 (Table 3), dashed (blue) line - level 36. Experiment: open circles with error bars [78]. Logarithmic scale is used for electron energies.

interesting in this case, the theoretical cross sections are within the error bars for the higher energies of the electron.

Theoretical cross sections calculated for the lowest and highest levels of the $3d^4 4s$ configuration are compared to measurements in Figure 17. All theoretical data are above the experimental values. The largest difference is obtained for the lower energies of impacting electron. The similar situation was also obtained for single ionisation cross section of neutral carbon and C^{1+} ion [53]. It was suggested that other physical mechanisms appear on the scene for ionisation process in these charge states.

The strongest EA channels for the ground level are shown in Figure 18. The $3p \rightarrow 3d$ excitation produces ~70 % of the total EA cross sections. The second highest cross section corresponds to the $3p \rightarrow 4p$ excitation, which leads to the same parity configuration as the ground one.

More complex situation regarding the strongest EA channels is obtained for the $3d^4 4s$ configuration (Figure 19). The $3p \rightarrow 3d$ excitation dominates over the other channels as in the case of the ground configura-

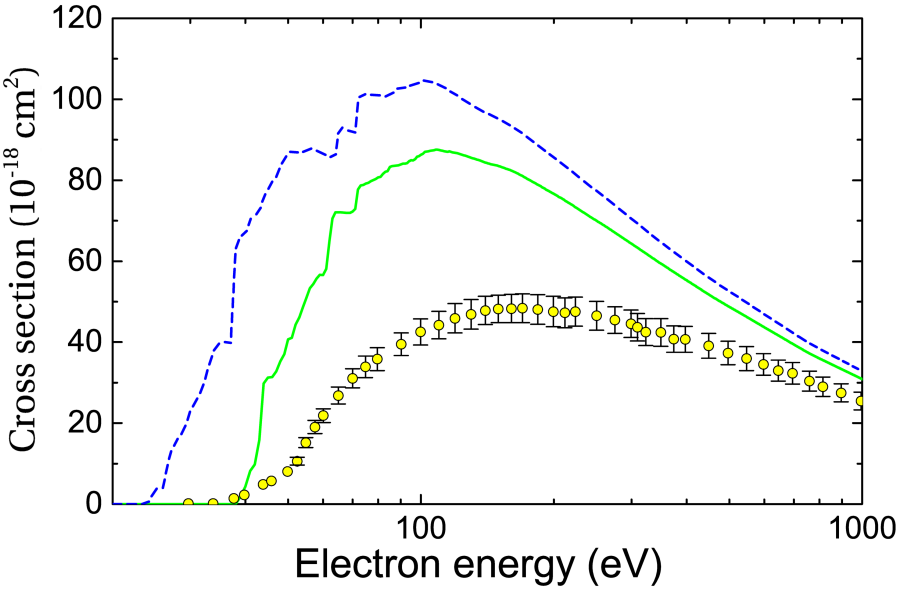

Figure 17: Single ionisation cross sections for the ground configuration levels: solid (green) line corresponds to level with index 37 (Table 3), dashed (blue) line - level 99. Experiment: open circles with error bars [78]. Logarithmic scale is used for electron energies.

tion (Figure 18). However, the excitations from the $3d$ subshell produce the strongest contribution at the lower energies of an electron. As was mentioned above, the excitations from the $3d$ subshell produce a small contribution to the EA cross sections for the ground configuration. The $3d \rightarrow 4d$, $3d \rightarrow 5d$ and $3p \rightarrow 4p$ excitations out of five strongest EA channels lead to the same parity configurations as the initial one.

The contributions of the direct and indirect processes for the ground level and the lowest level of the $3d^4 4s$ configuration are shown in Figure 20. The EA channels corresponding to excitations up to shells with the principal quantum number $n = 8$ are considered in the study, since the excitations to the higher shells give a negligible contribution. Furthermore, the direct process produces a slightly higher contribution for the ground level compared to the lowest level of the $3d^4 4s$ configuration. This can be explained by a smaller number of electrons in the $3d$ subshell of the $3d^4 4s$ configuration compared to the ground configuration. The DI cross sections for the $4s$ subshell do not compensate for the smaller number of electrons in the $3d$ subshell of the first excited configuration. In addtition,

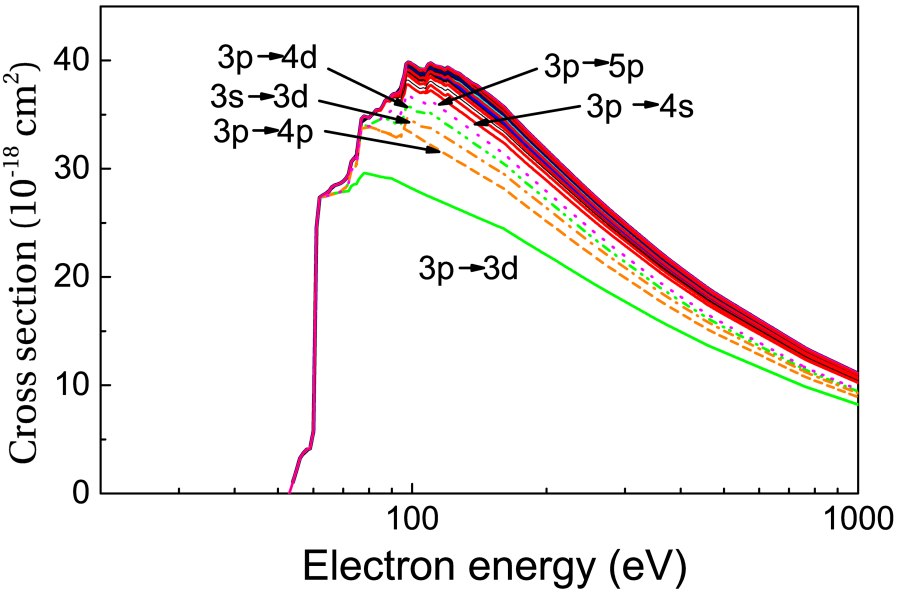

Figure 18: Accumulated cross sections of the EA channels contributing to the ionisation of the ground level of Fe^{3+}. The strongest EA contributions are individually identified. Logarithmic scale is used for electron energies.

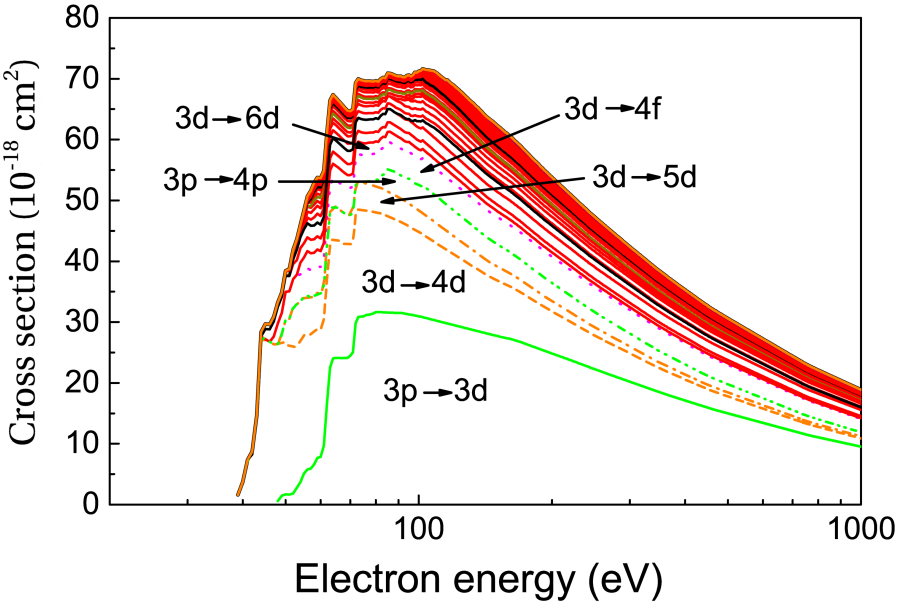

Figure 19: The same as Figure 18 but for the lowest level of the $3d^4 4s$ configuration.

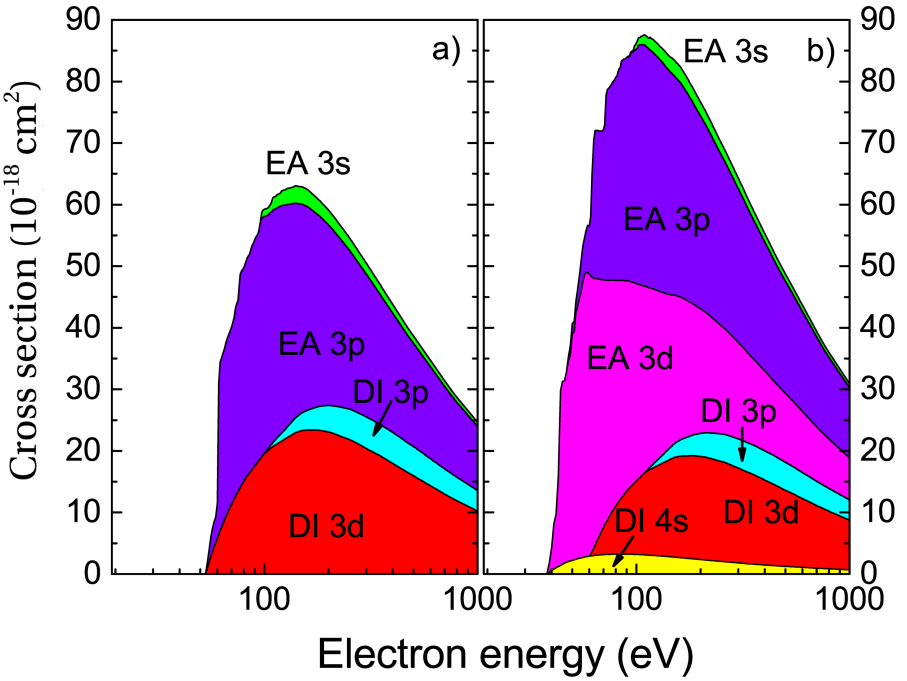

Figure 20: Comparison of contribution from the DI and EA channels for single ionisation of Fe^{3+}: (a) ground configuration, (b) the lowest level of the $3d^4 4s$ configuration. A logarithmic scale is used for electron energies.

the EA cross sections for the $3d^4 4s$ configuration are higher than for the ground configuration, since excitations from the $3d$ subshell of the first excited configuration produce autoionising states which decay to Fe^{4+}. The $3d$ subshell is the outermost one for the ground configuration and, therefore, only a small contribution is provided to the EA process. For both configurations, the EA channels corresponding to excitations from the $3p$ subshell dominate starting from $\sim$100 eV.

In summary, the EA channels corresponding to excitations to the higher-nl shells ($n > 8$) do not provide an essential contribution for the energy levels of the ground and the first excited configurations of the Fe^{3+} ion. The convergence of the EA cross sections is reached for the excitation up to shells with $n = 8$. The excitations from the $3p$ subshell dominate over the other EA channels. The excitations to orbital quantum numbers $l = 1$ and $l = 2$ produce the main contribution to the cross sections of the indirect process.

Correlation Effects

The influence of correlation effects is studied for Fe^{3+} and W^{5+}. We use the CIS [48, 84] method to select configurations that can affect ionisation cross sections. Below it is shown the importance of correlation effects by discussing two selected cases from our researches.

W^{5+} Ion Case [A5]

The influence of correlation effects on direct and indirect processes of ionisation have been studied for the $5d$ configuration using the CI method. A list of admixed configurations having the largest effect for the considered configuration was generated using the CIS concept [see Eq. (51)]. The same approach was applied previously to electric [85] and magnetic dipole transitions [28, 86], Auger cascades [69, 70, 87] and electron-impact ionisation [21, 22]. For excitations to levels with the same parity as the initial level, interacting configurations has to include the initial configuration. It is found that CI has a crucial effect on the results.

A comparison of cross sections obtained in the single- configuration approximation and by using the CI method is presented in Figure 21. It can be seen that correlation effects diminish the cross sections by ∼20 % at the maximum. The CI cross sections are within the experimental cross sections error bars at the maximum and at higher energies. We note that the CI largest effect is obtained for the $4f \rightarrow 5f$ excitations. The CI effects reduce the associated cross sections by ∼8 Mb (corresponding to ∼80 %) at maximum value.

In order to reproduce the experimental cross section [74] and test the theoretical approach validity, it is necessary to consider not only the ground state of the W^{5+} ion, but also include all possible (long-lived) excited levels of the W^{5+} ions that have been present in the parent ion beam used during the measurements. The levels which have to be taken into account are listed in Table 2. Moreover, total single-ionisation cross sections, including the DI and EA contributions, have been calculated for each level listed in the table. For the excited configurations, the inclusion of CI effects would have made the calculations too large. Therefore, CI was only taken into account for the ground configuration.

For comparing the calculated cross sections with the experimental

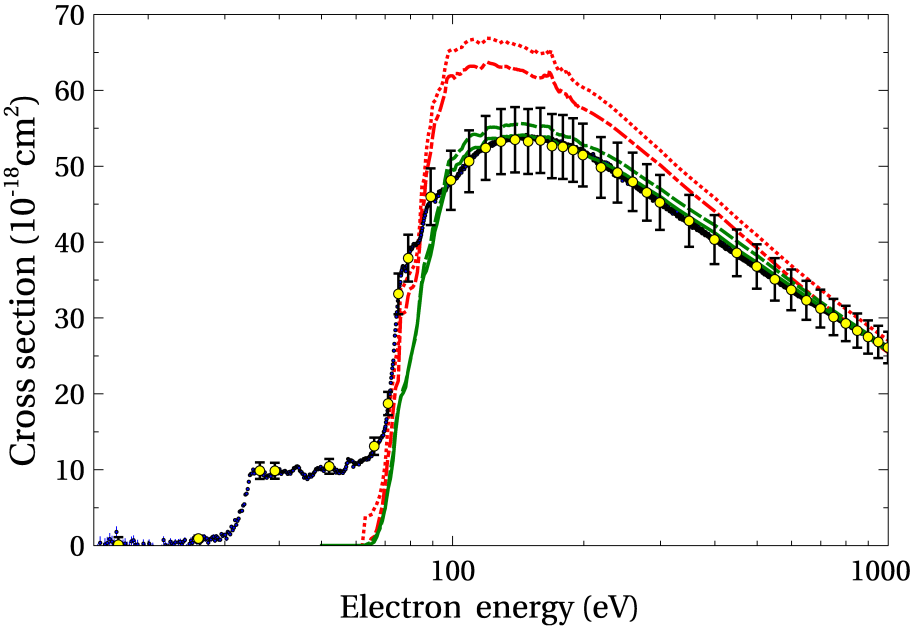

Figure 21: Comparison of electron-impact ionisation cross sections for W^{5+} obtained in the single-configuration approximation (upper pair of red lines) and by using a basis of interacting configurations (lower pair of green lines). The solid (green) and the long-dash-short-dashed (red) lines represent the cross sections of the $5d\,^2D_{3/2}$ ground level. The long-dashed (green) and the dotted (red) lines represent the cross section of the $5d\,^2D_{5/2}$ excited level. Experimental electron-impact ionisation cross section of W^{5+} ions (circles with (yellow) shading with total error bars: absolute cross sections [74]; black dots with statistical error bars: results of the fine-step energy scan normalised to the absolute data points) compared to the previous measurements.

results also shown in Figure 21. It is necessary to know the fractions λ_i of ions in all possible levels (index i, see Table 2, page 52) that contributed to the measured single-ionisation spectrum (see Eq. 52, page 33). These fractions are not *a priori* known from the experiment. This problem has been addressed previously in the context of storage-ring electron-ion recombination measurements with tungsten ions [88, 89]. In these investigations, the temporal evolutions of level populations were calculated. Maxwell distribution was used to describe the population of excited levels when the fast parent ions pass a stripper foil. Then rate equations were used to describe the radiative decays of these levels [90],

until the ions interact with the target electrons. The time for the ions to relax in these experiments was in the order of seconds. Quite different from the ~ 15 microsecond time-of-flight in the present experiment for which three different approaches have been applied. The model is based on the calculated cross sections of the experimental data and assesses all λ_i.

Since the W^{5+} ions are produced in the ion source plasma it makes sense to assume statistical populations of levels within each of the contributing configurations, in the present case $5d$, $6s$, $4f^{13}5d^2$, $5p^5 5d^2$ and $4f^{13}5d\,6s$. This kind of assumption has been successfully applied in numerous previous studies of collision processes involving ion beams, and is considered to be the most realistic approach also to the present problem. With this starting condition Eq. (52) is modified to Eq. (53) where c_k are fitting parameters for each of the five configurations considered (see Table 2).

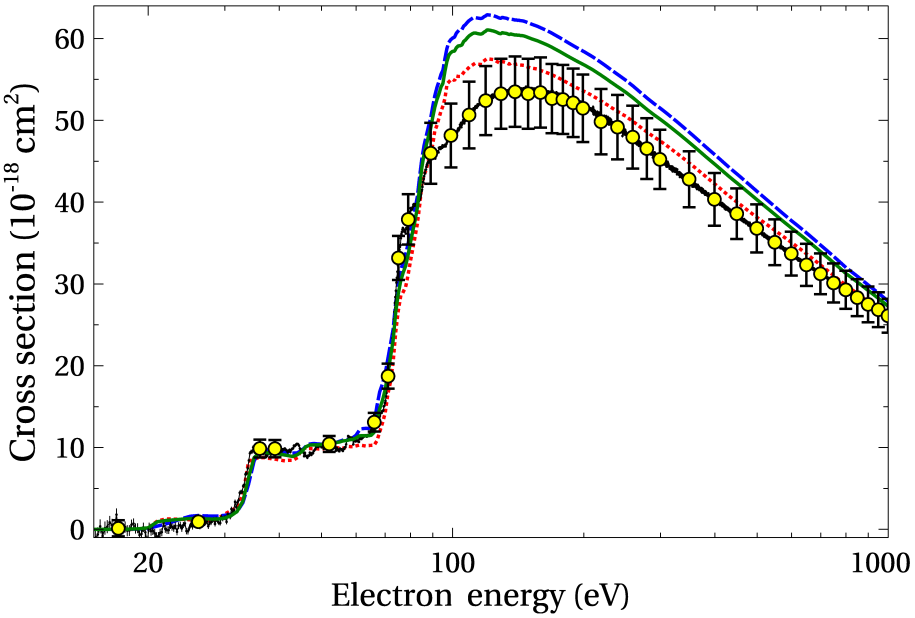

Figure 22: Electron-impact ionisation cross sections for the W^{5+} ion. Circles with error bars and (yellow) shading: experimental absolute cross sections, solid black noisy line: fine-step energy-scan data [74]. The (green) solid line is the result of model 1 (see Eq. 53 and text), the dashed (blue) line corresponds to model 2 (see Eq. 54 and text). The dotted (red) line is obtained from model 3 (see Eqs. 52, 55 and text).

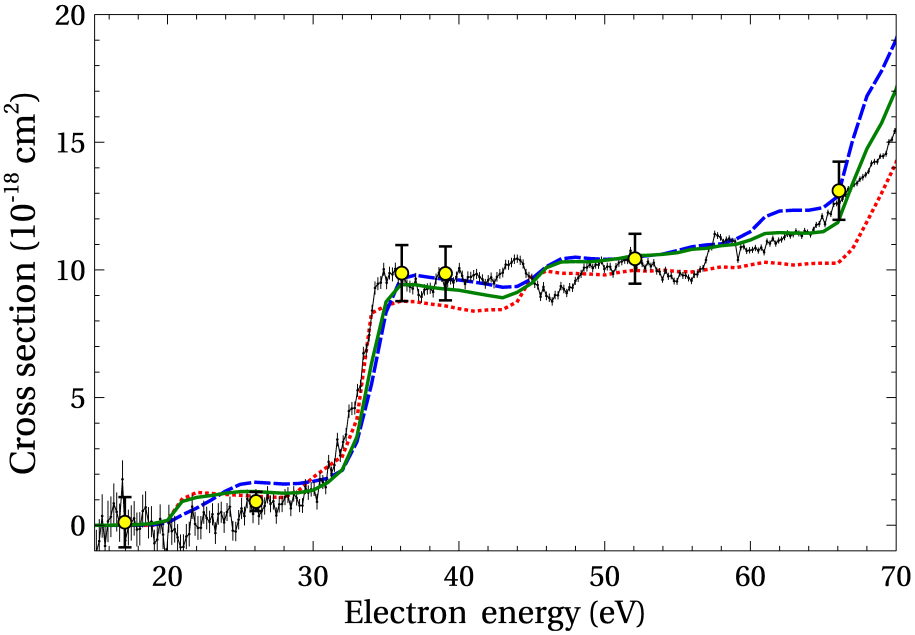

Figure 23: Same as Figure 22 in the energy range where only metastable levels contribute to the total single-ionisation cross section.

The study for photo-ionisation in W^{5+} suggested that the ECR ion source employed in both experiments produced 2.5 % of ions in the metastable $6s$ configuration [91]. This knowledge reduces the number of free fitting parameters c_k to four. The remaining fitting parameters in this model, apart from $c_2 = 0.025$ for the $6s$ configuration were determined to be $c_1 = 0.85$ for the $5d$ ground configuration, $c_3 = 0.082$ for $4f^{13}5d^2$, $c_4 = 0.036$ for $5p^5 5d^2$ and $c_5 = 0.007$ for $4f^{13}5d\,6s$. The energy range from 20 eV to 70 eV was used to determine the theoretical models best agreement with the measurements. It is noted that a fit over a wider energy range leads to lower cross sections for the contribution of metastable ions at energies below the ground-state ionisation threshold. This corresponds to the lower metastable fraction of the ion beam in the theoretical model. Therefore, the highest limit for the metastable fraction is approximately determined using the energy range of 20–70 eV in the modelling. The solid green line represents the theoretical model cross section resulting from the fit over the 20 to 70 eV range in Figure 23. This line is in very good agreement with the cross section below the ground-state ionisation threshold. It is slightly above the experimental

cross section [74], particularly at energies around 100 eV. This may be a consequence of the known overestimation of ionisation cross sections by the DW approximation when applied to neutral atoms or ions in low charge states. Correlation effects were not considered for the ionisation from the excited configurations can be a reason for the disagreement. It may also be due to the model chosen for reproducing the experimental cross section.

The second model reduces the number of fitting parameters to one. With the argument that the ions are primarily produced in a plasma one may assume a Boltzmann distribution for the population of excited levels. This reduces the problem to fitting the temperature T. Eq. (52) then takes the form of Eq. (54). In this case, J_i is the total angular momentum quantum number and E_i the excitation energy of level i. A temperature $T = 78,000$ K brings this model into the best agreement with the experiment. A temperature of 78,000 K is of the right size for producing moderately low charge states of tungsten ions such as W^{4+} and W^{5+} in a plasma [92].

The third model treats all 68 fractions λ_i in Eq. (52) as free fitting parameters. Since the measured electron-impact ionisation cross sections, obtained in the present energy scan, comprise more than 5000 data points with a very specific energy dependence, such a fit with so many parameters is less ambiguous than one might think. However, the model is rooted more in mathematical methods than in the physics of ion sources and ion beams. The fractions λ_i are chosen such that the function reaches a minimum.

The minimum is obtained when only four levels are assumed to contribute to the sum in Eq. (55), the ground level with ∼93.5 %, the level with index 35 belonging to the $4f^{13}5d^2$ configuration contributing 1.2 % and two levels of the $5p^5 5d^2$ configuration with indices 105 and 116 contributing 4.1 % and 1.2 %, respectively. This model gives the best agreement with the measured cross section function. However, it is highly doubtful that only four levels out of 68 should be present in the ion beam.

The model cross sections, shown in Figure 22 as a long-dashed (blue) line, describes the measured data below the ground-state ionisation threshold very well. At energies above approximately 100 eV, it is even higher than the cross section resulting from the first model. However, the

difference is relatively small. The corresponding fractions of ions in the relevant configurations are 78.8 % for the $5d$ configuration, 4.1 % for $6s$, 13.7 % for $4f^{13}5d^2$, 1.4 % for $5p^5 5d^2$ and 2.0 % for $4f^{13}5d\,6s$. With 4.1 %, the $6s$ fraction is overestimated in comparison with the photoionisation experiment where 2.5 % have been found. The maximum deviation of the Boltzmann model from the experiment is about 20 % near 100 eV. It is about 10 % above the experimental error bars.

Table 4: Fractions of ions in different initial configurations present in the parent ion beam that was used in the experiments. The numbers obtained depend on the model assumptions (see main text).

model	$5d$	$6s$	$4f^{13}5d^2$	$5p^5 5d^2$	$4f^{13}5d6s$
1	0.85	0.025	0.082	0.036	0.007
2	0.788	0.041	0.137	0.014	0.020
3	0.935	0	0.012	0.053	0

All three models give a very good representation of the cross section contributions observed in the experiment below the ground-state ionisation threshold as emphasised in Figure 23. The comparison of the three models in Table 4 elucidates the uncertainty of the fractions of ions in different levels that contributed to the measured cross section. The fraction of ions in the ground configuration is most likely $c_1 = 0.85$ for which a 10 % relative-uncertainty margin seems realistic. Hence, the metastable fractions derived from the comparisons of theory and experiment have very substantial relative uncertainties.

Therefore, it may be concluded that the experimental data for electron impaction ionisation cross sections in W^{5+} are explained by including the correlation effects in the study. These effects are studied for the ionisation from the levels of the ground configuration. The correlation effects diminishes the cross sections by ∼20 % at the peak value. Further studies of the correlation effects for the metastable levels are required to confirm current findings.

Fe^{3+} Ion [A4]

The influence of correlation effects is investigated for the direct ionisation and strongest excitations from levels of the ground and $3d^4 4s$

configurations. A list of admixed configurations having the largest influence on the considered configuration is generated by using configuration interaction strength (CIS), the same as in the case of W^{5+} ion. Additionally, the list of admixed configurations is built by considering single and double excitations from the shells with the principal quantum number $n \geqslant 3$ up to shells with $n = 8$.

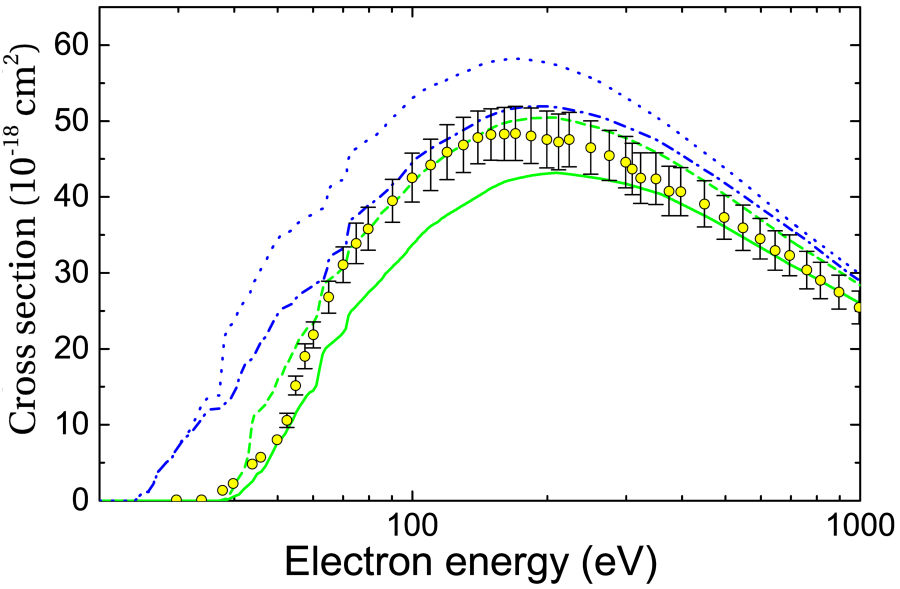

Figure 24: Comparison of influence of CI effects to single ionisation cross sections for the levels of the $3d^4 4s$ configuration: solid (green) line - scaled DW cross sections with CI for level with index 37 (Table 3), dashed (green) line - scaled DW cross sections for level 37, dashed-dotted (blue) line - scaled DW cross sections with CI for level 99, dotted (blue) line - scaled DW cross sections for level 99. Experiment: open circles with error bars [78]. Logarithmic scale is used for electron energies. For further details see the main text.

It should be noted that the correlation effects have a small effect on the cross sections of the direct process. However, a different situation is observed for EA. The study included the $3p \rightarrow 3d$ and $3p \rightarrow 4p$ excitations for the ground configuration and $3p \rightarrow 3d$, $3d \rightarrow 4d$, $3d \rightarrow 5d$ and $3p \rightarrow 4p$ for the $3d^4 4s$ configuration. Nevertheless, only a negligible influence of the correlation effects to the EA cross sections is found for the ground configuration, even though the correlation effects diminish the scaled cross sections by approximately 20 % for the levels of the

first-excited configuration (Figure 24). The correlation effects diminish the scaled DW cross sections by ∼20 % for the lowest and the highest levels of the $3d^4 4s$ configuration. Comparison among the cross sections calculated without scaling and the ones with scaling as well as the correlation effects brings the difference of ∼50 %. The correlation effects for the scaled cross sections of the lowest level of the excited configuration lead to values below the threshold energy measurements up to 200 eV and within the error bars for the higher energies. On the other hand, the cross sections for the highest level of the $3d^4 4s$ configuration are above measurements from the threshold energy up to 70 eV and starting from ∼200 eV.

To summarise, it was shown that correlation effects play an important role and lead to a substantial reduction of cross sections for the $3d^4 4s$ configuration of the Fe^{3+} ion. Correlation effects reduce the theoretical cross sections obtained for the ground configuration by ∼20 % for the Fe^{3+} ion. The disagreement among theoretical and experimental values can be related to the correlation effects that are not accounted for in the calculations for the excited configurations due to limitations in the computing resources.

Resonant Excitation-Double Autoionisation Process [A3]

The REDA process produces resonant structure in the single ionisation cross sections. The more elaborated studies are required, since the Auger cascade from the formed states leading to single ionisation has to be considered. It is estimated from data that the REDA process can contribute about 20-30 % to the ionisation rate. Often, theoretical cross sections cannot reproduce accurately experimental cross sections without accounting for the REDA processes [93]. Furthermore, DC to many autoionising states has to be included in the analysis. Here, the REDA process is studied for the ground configuration of the Se^{3+} ion.

The obtained theoretical single ionisation threshold of Se^{3+} is 42.35 eV. Energy of 108.21 eV is needed to remove two outer electrons from the ground [Ar]$3d^{10}4s^24p^1$ configuration and reach ground configuration of the Se^{5+} ion. The single ionisation threshold is in good agreement with a value of 42.2 ± 1.8 eV determined from the experiment [13] and the NIST reference value of 42.95 eV [94]. The ground configuration of the Se^{3+} ion has only two levels. Energy of the fine splitting is 0.5668 eV (Table 5) as NIST provides slightly lower value of 0.5426 eV. The difference of about 4 % between these two values can be attributed to correlation effects which are not considered in this work.

Table 5: The energy levels and lifetimes of the five lowest configurations for Se^{3+}. The lifetimes include the electric dipole, quadrupole, octupole and magnetic dipole and quadrupole transitions. Closed subshells are omitted in the notation of levels.

Index	Configuration	Level	J	Energy (eV)	τ (s)
0	$4s^24p^o$	$4p_{1/2}$	1/2	0.000	—
1	$4s^24p^o$	$4p_{3/2}$	3/2	0.567	1.16E+0
2	$4s4p^2$	$4s$	1/2	8.316	5.06E−7
3	$4s4p^2$	$4s\ 4p_{1/2}[0]4p_{3/2}$	3/2	8.531	1.86E−6
4	$4s4p^2$	$4s\ 4p^2_{3/2}(2)$	5/2	8.852	4.77E−7
5	$4s4p^2$	$4s\ 4p_{1/2}[0]4p_{3/2}$	3/2	13.273	4.00E−10

Continued on next page

Table 5: (continued)

Index	Configuration	Level	J	Energy (eV)	τ (s)
6	$4s4p^2$	$4s\ 4p_{1/2}[2]4p_{3/2}$	5/2	13.344	4.48E−10
7	$4s4p^2$	$4s\ 4p^2_{3/2}(0)$	1/2	15.710	2.39E−10
8	$4s4p^2$	$4s\ 4p_{1/2}[1]4p_{3/2}$	1/2	17.558	6.08E−11
9	$4s4p^2$	$4s\ 4p^2_{3/2}(2)$	3/2	17.893	5.89E−11
10	$4s^24d$	$4d_{3/2}$	3/2	18.374	9.95E−11
11	$4s^24d$	$4d_{5/2}$	5/2	18.417	1.04E−10
12	$4p^{3o}$	$4p_{1/2}4p^2_{3/2}(2)$	3/2	24.917	7.23E−11
13	$4s4p4d^o$	$4s\ 4p_{1/2}[0]4d_{3/2}$	3/2	26.069	1.66E−8
14	$4s4p4d^o$	$4s\ 4p_{1/2}[1]4d_{3/2}$	5/2	26.209	9.85E−9
15	$4s4p4d^o$	$4s\ 4p_{1/2}[1]4d_{5/2}$	7/2	26.396	9.02E−9
16	$4s4p4d^o$	$4s\ 4p_{3/2}[2]4d_{5/2}$	9/2	26.618	8.95E−1
17	$4p^{3o}$	$4p_{1/2}4p^2_{3/2}(2)$	3/2	27.273	1.71E−10
18	$4p^{3o}$	$4p_{1/2}4p^2_{3/2}(2)$	5/2	27.368	1.68E−10
19	$4s4p4d^o$	$4s\ 4p_{1/2}[0]4d_{5/2}$	5/2	27.733	1.66E−10
20	$4s4p4d^o$	$4s\ 4p_{1/2}[1]4d_{5/2}$	3/2	27.779	2.97E−10
21	$4s4p4d^o$	$4s\ 4p_{3/2}[2]4d_{5/2}$	3/2	28.014	7.34E−11
22	$4s4p4d^o$	$4s\ 4p_{3/2}[2]4d_{5/2}$	5/2	28.048	1.12E−10
23	$4s4p4d^o$	$4s\ 4p_{1/2}[1]4d_{3/2}$	1/2	28.074	5.86E−11
24	$4s4p4d^o$	$4s\ 4p_{3/2}[2]4d_{3/2}$	1/2	28.338	7.87E−11
25	$4s4p4d^o$	$4s\ 4p_{3/2}[2]4d_{5/2}$	7/2	28.380	5.34E−11
26	$4s4p4d^o$	$4s\ 4p_{3/2}[2]4d_{3/2}$	3/2	28.382	6.61E−11
27	$4s4p4d^o$	$4s\ 4p_{3/2}[2]4d_{3/2}$	5/2	28.403	5.95E−11
28	$4p^{3o}$	$4p_{1/2}4p^2_{3/2}(0)$	1/2	28.972	1.35E−10
29	$4p^{3o}$	$4p_{3/2}$	3/2	29.126	1.33E−10
30	$4s4p4d^o$	$4s\ 4p_{1/2}[1]4d_{5/2}$	5/2	30.142	1.49E−10
31	$4s4p4d^o$	$4s\ 4p_{3/2}[2]4d_{3/2}$	7/2	30.578	1.36E−10
32	$4s4p4d^o$	$4s\ 4p_{3/2}[2]4d_{5/2}$	3/2	30.939	1.71E−10
33	$4s4p4d^o$	$4s\ 4p_{3/2}[2]4d_{5/2}$	1/2	31.188	1.70E−10
34	$4s4p4d^o$	$4s\ 4p_{3/2}[1]4d_{5/2}$	7/2	34.456	3.76E−11
35	$4s4p4d^o$	$4s\ 4p_{3/2}[1]4d_{3/2}$	5/2	34.528	3.92E−11
36	$4s4p4d^o$	$4s\ 4p_{3/2}[1]4d_{3/2}$	3/2	34.537	4.90E−11
37	$4s4p4d^o$	$4s\ 4p_{3/2}[1]4d_{5/2}$	5/2	34.631	4.52E−11
38	$4s4p4d^o$	$4s\ 4p_{3/2}[1]4d_{3/2}$	1/2	35.180	4.94E−11

Continued on next page

Table 5: (continued)

Index	Configuration	Level	J	Energy (eV)	τ (s)
39	$4s4p4d^o$	$4s\ 4p_{3/2}[1]4d_{5/2}$	3/2	35.252	4.99E−11

Contributions from long-lived levels are often seen in experiments for ionisation cross sections [29, 95]. The first two excited configurations $4s4p^2$ and $4s^24d$ of the Se^{2+} ion do not contain long-lived levels (Table 5). The first long-lived level which cannot decay through strong electric dipole (E1) transitions belongs to the $4s4p4d$ configuration. The decay of $4s4p_{3/2}$ ($J = 2$) $4d$ $J = 9/2$ level (index 16) to the lower levels of $4s4p^2$ or $4s^24d$ configurations by the E1 transitions is restricted by the $\triangle J = \pm 1$ selection rule.

Our calculations show that electron-impact ionisation cross sections for the long-lived $4s4p_{3/2}$ ($J = 2$) $4d$ $J = 9/2$ level are about three times higher than experimental values. Also, the cross sections start at about 17 eV, while experimental single ionisation threshold corresponds to 42.2 ± 1.8 [13]. This demonstrates that contribution from this level was not observed in the experiment.

Figure 25 shows configurations in which energy levels straddle the single ionisation threshold. All four configurations of the Se^{3+} ion correspond to the $4s$ subshell excitations. Only one of four configurations has subconfigurations with average energies above the ionisation threshold. The configurations produced by excitations from the $3d$ subshell are above the single ionisation threshold. Besides, the energy levels of the ground and the first excited configurations for the Se^{3+} and Se^{4+} ions are presented in Figure 25.

Our obtained electron-impact ionisation cross sections for the ground level corresponding to the DI, EA and REDA processes are compared with experimental values in Figure 26. The DI cross sections are obtained in the potential of the ionised ion. The contribution of the radiative damping to the cross sections of the indirect process is negligible. The indirect EA process, compared to the direct one, dominates at the incident electron's lower and intermediate energies. However, EA influence diminishes at the higher energies, especially when ionisation from the $3d$ subshell appears on the scene. It has to be noted that ionisation from the $3d$ subshell has the largest contribution to the total cross sections compared to the

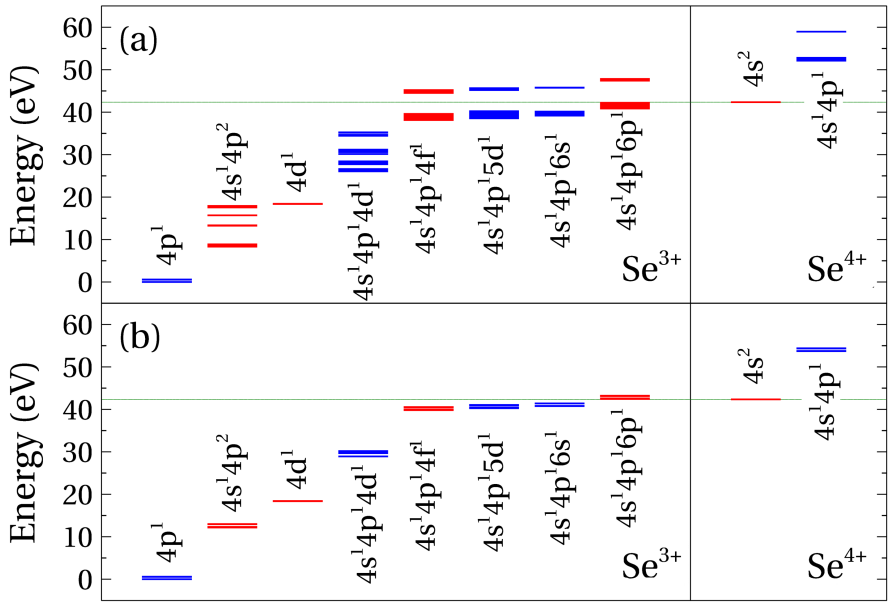

Figure 25: Energy levels (a) and subconfigurations (b) of four lowest configurations and configurations that straddle the ionisation threshold for the Se^{3+} ion. The ground and first excited configurations of Se^{4+} are also presented. Red – even configurations, blue – odd configurations.

ionisation from the valence 4*s* and 4*p* subshells. Previous calculations for Se^{3+} have been performed using the CADW method [19]. Thus, we also investigated the ionisation process using the subconfiguration-averaged DW method and found good agreement among both our values for all energies of the incident electron.

Comparison of our LLDW results to the previous CADW [19] and LLDW [20] calculations is presented in Figure 27.

The CADW cross sections are mainly below our data obtained in the ionising ion's potential at the incident electron's lower and medium energies. Surprisingly, good agreement between the CADW and our cross sections is observed at the higher energies. It should be noted that the incident and scattered electrons are studied in the potential of the ionising ion, and the ejected electrons are calculated in the potential of the ionised ion for the CADW data [19]. This can be the reason for a difference among the DI values obtained from CADW [19] and our LLDW

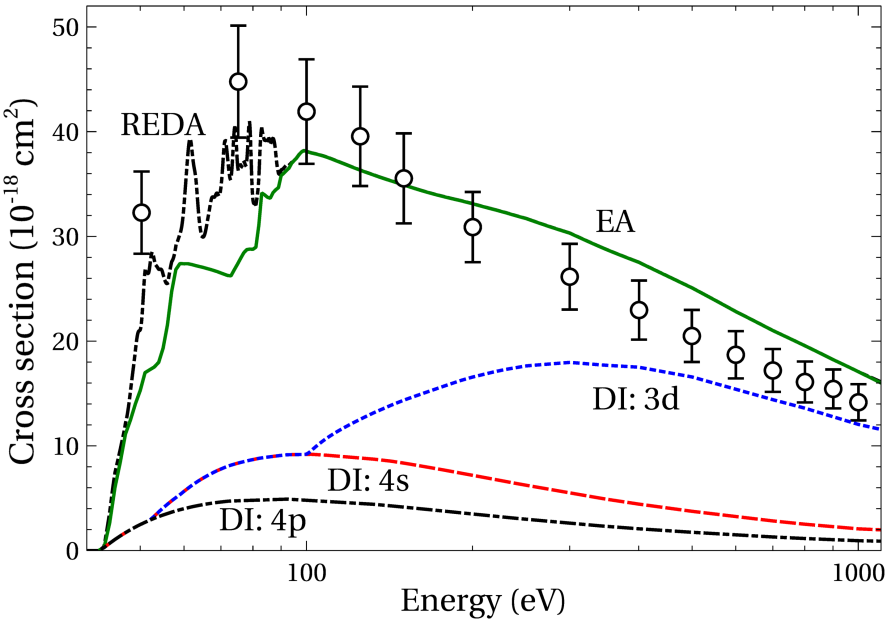

Figure 26: Single ionisation cross sections for the DI, EA and REDA processes. Experiment: open circles with error bars [14]. Logarithmic scale is used for electron energies.

calculations. CADW values are higher by about 40 % compared to our data calculated in ionised ion potential. The difference of about 15 % from the CADW calculations is obtained for cross sections studied in the ionising ion's potential. A similar effect for the DI process has been observed in the study of the tungsten ions [59, 63]. What is more, our EA data include excitations up to shells with $n = 25$, while the CADW values correspond to the excitations up to $n \leqslant 8$ [19]. Therefore, the lower contribution of the EA data to the total ionisation cross sections is compensated by the bigger influence of the DI process in the CADW calculations.

The difference among our LLDW values and results presented in [20] is also observed in Figure 27. This difference is more expressed at the higher energies of the incident electron. This can be explained by the fact that ionisation from the $3d$ subshell was not included in the previous calculations. It was stated that produced configuration decays to Se^{5+}. However, the $3d^9 4p$ configuration is below the double ionisation

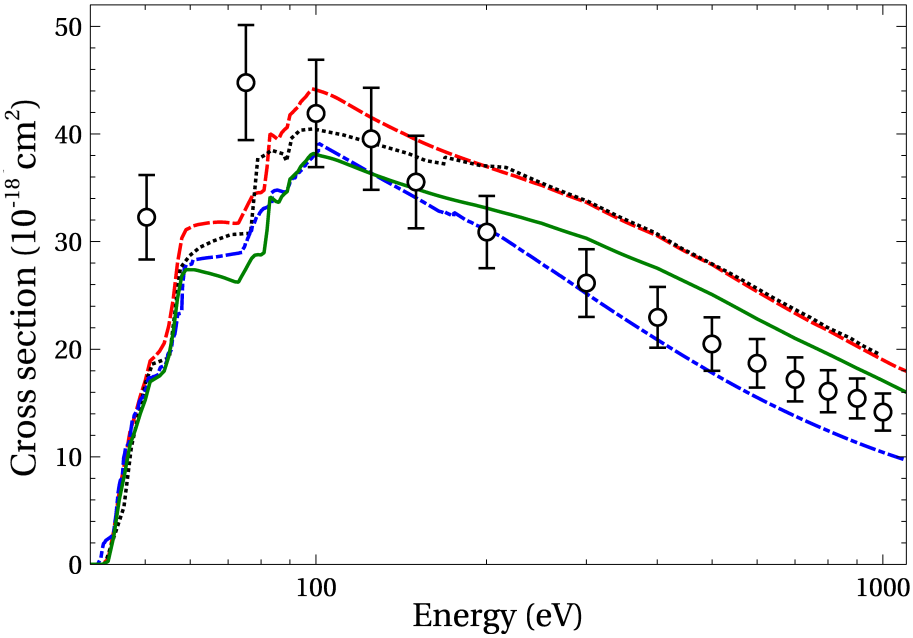

Figure 27: Comparison of the total single ionisation cross sections. Our LLDW data are obtained in the potential of the ionised (green solid) and ionising (red dashed) ions; dashed-dotted line (blue) represents CADW values [19], dotted line (black) - LLDW [20]. Experiment: open circles with error bars [14]. Logarithmic scale is used for electron energies.

threshold [19] and, thus, direct ionisation results in Se^{4+}. The main reason for the difference is that the main configuration is generated by the ground configurations of Se^{3+} and Se^{4+} to obtain the bound and continuum potential electrons in their calculations. This leads to much higher DI cross sections in their calculations. For example, DI $4s$ cross sections are higher about 40 % than our values calculated in ionised ion potential.

Figure 28 shows the main contributions of the EA channels compared to DI. The strongest EA channels correspond to $3d \rightarrow 4p$ and $3d \rightarrow 4d$ excitations. These two excitations make just slightly less than half of the total ionisation cross sections for the indirect process. The other EA channels separately provide a much smaller contribution compared to the strongest ones. However, a large number of the weaker channels accounts for a significant part of the indirect process.

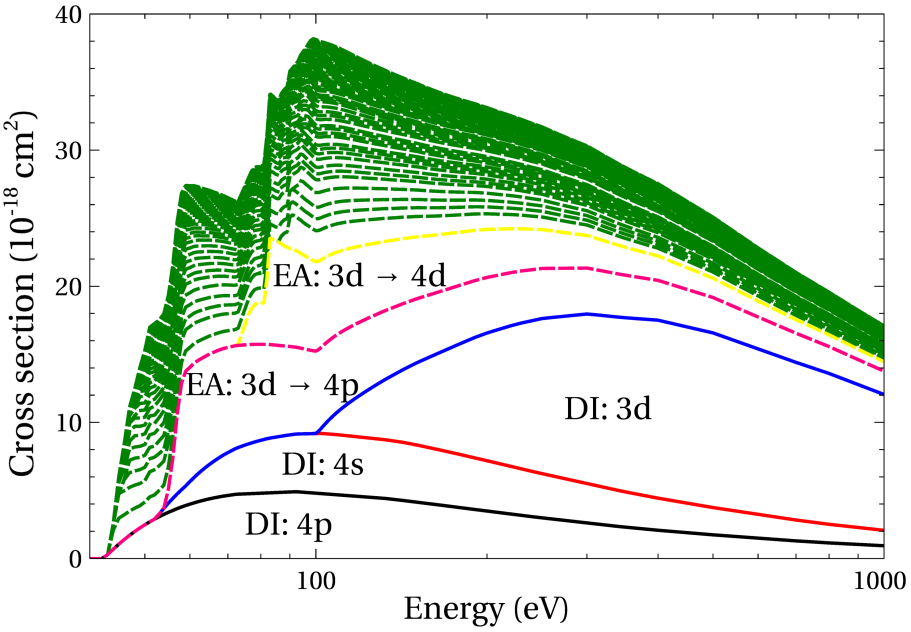

Figure 28: Comparison of contribution from the DI and EA channels for single ionisation of Se^{3+}. Logarithmic scale is used for electron energies.

It can be concluded, that the single ionisation cross sections for the Se^{4+} ion are explained by considering the REDA process. In addition to DI and EA, the REDA cross sections are important from the ionisation threshold up to ∼90 eV. The resonant structure is seen in the cross sections.

Scaled Distorted Wave Cross Sections [A4]

In this section, we present our work related to scaling the theoretical cross section to match experimental data. This approach gives some clues about whether we should search for additional processes or phenomena in ionisation cross section modelling.

There are multiple attempts to use scaling functions to produce an experimental cross section from a defined parameter list. Previously, the scaled plane-wave Born (PWB) cross sections for electron-impact excitation were used to mimic the effects related to the polarisability

of the atomic system [36]. Moreover, it was suggested that electron exchange, distortion and polarisation effects, missing in the first-order PWB approximation, are included in the calculations using the scaling functions. The studies of electron impact ionisation process for neutral atoms and near-neutral ions using binary-encounter-dipole (BED) or binary-encountered-Bethe (BEB) models [35] with the scaled PWB cross sections [36] demonstrated a good agreement with experimental data [36, 38, 39, 96]. Recently, it was shown that the scaled DW cross sections could be used to explain experimental data for neutral carbon and C^+ ion [53]. The scaled DW cross sections corresponding to ionisation from the ground and first excited configurations of the Fe^{3+} ion are used to explain measurements [78]. The scaled DW cross sections for the lowest and excited levels of the ground configuration are shown in Figure 29. Besides, the single-configuration DW data along with the measurements [78] are presented for comparison. The largest effect of scaling is obtained for the lower energies of impacting electron. It can be seen that all theoretical data for the ground level are below the experimental errors. On the other hand, the highest level of the ground configuration demonstrates good agreement with higher energies measurements. However, these cross sections are below the error bars for the lower electron energies except in the region from 40 to 50 eV, where the theoretical values are slightly above the measurements.

The scaled DW cross sections for the lowest and highest levels of the first excited $3d^4 4s$ configuration are shown in Figure 30. Single-configuration DW cross sections and experimental values are presented for comparison. The cross sections for the lowest level of the configuration are in quite good agreement with measurements for electron energies starting from 60 eV. On the other hand, the theoretical cross sections are above experimental error bars in the 40 – 60 eV region. The theoretical cross sections obtained for the highest level of the configuration overestimate the measurements.

The underestimated scaled DW cross sections, concerning the measurements for the levels of the ground configuration (Figure 19, page 63), suggest that the levels of the excited $3d^4 4s$ configuration are present in the ion beam. Nevertheless, the theoretical values for the levels of the $3d^4 4s$ configuration are above the error bars in the range of 40 – 60 eV. This demonstrates that some additional effects have to be considered to

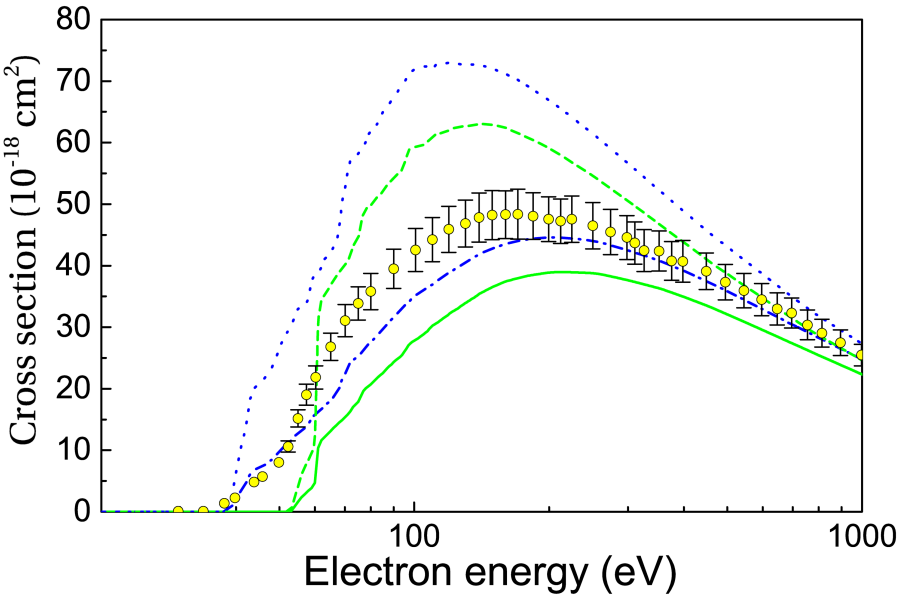

Figure 29: Single ionisation cross sections obtained with and without the scaling functions [Eqs. (53) and (54)] for the levels of the ground configuration: solid (green) line - scaled DW cross sections for level with index 0 (Table 3), dashed (green) line - DW cross sections for level 0, dashed-dotted (blue) line - scaled DW cross sections for level 36, dotted (blue) line - DW cross sections for level 36. Experiment: open circles with error bars [78]. Logarithmic scale is used for electron energies.

explain the observed data.

The comparison with measurements for the level with index 67 is presented in Figure 31. This level, together with level 49 (Table 3), have the largest values of the total angular momentum quantum number J for the $3d^4 4s$ configuration. The levels with the largest statistical weights would be populated with the largest probability in the ion beam. On the other hand, the Boltzmann distribution or even collisional radiative modelling with subsequent radiative cascade may have to be used to determine the level population. However, these modellings would require a separate study. It can seen that the theoretical cross sections are still below experimental values in the energy range from approximately 50 to 150 eV. This difference can be explained by the resonant excitation double autoionisation process, which is not investigated in this work.

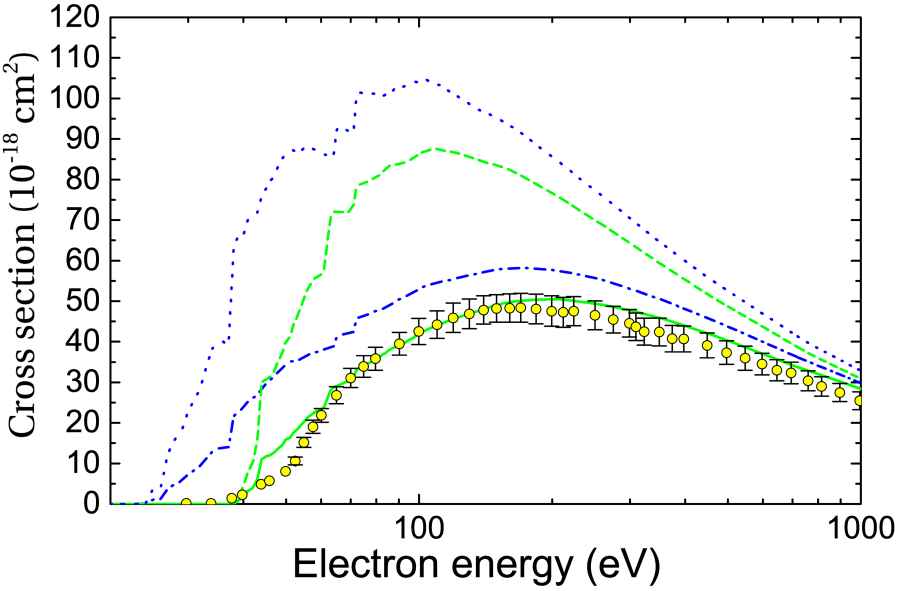

Figure 30: Single ionisation cross sections obtained without and with the scaling functions [Eqs. (53) and (54)] for the levels of the $3d^4 4s$ configuration: solid (green) line - scaled DW cross sections for level with index 37 (Table 3), dashed (green) line - DW cross sections for level 37, dashed-dotted (blue) line - scaled DW cross sections for level 99, dotted (blue) line - DW cross sections for level 99. Experiment: open circles with error bars [78]. Logarithmic scale is used for electron energies.

In summary, the scaled DW cross sections are used to explain measurements for the Fe^{3+} ion. The energy levels of the ground $3d^5$ and excited $3d^4 4s$ configurations are analysed. The scaling leads to the diminished DW cross sections by $\sim$40 %. The peaks of the scaled cross sections shifts to the higher energies what corresponds to the experimental data.

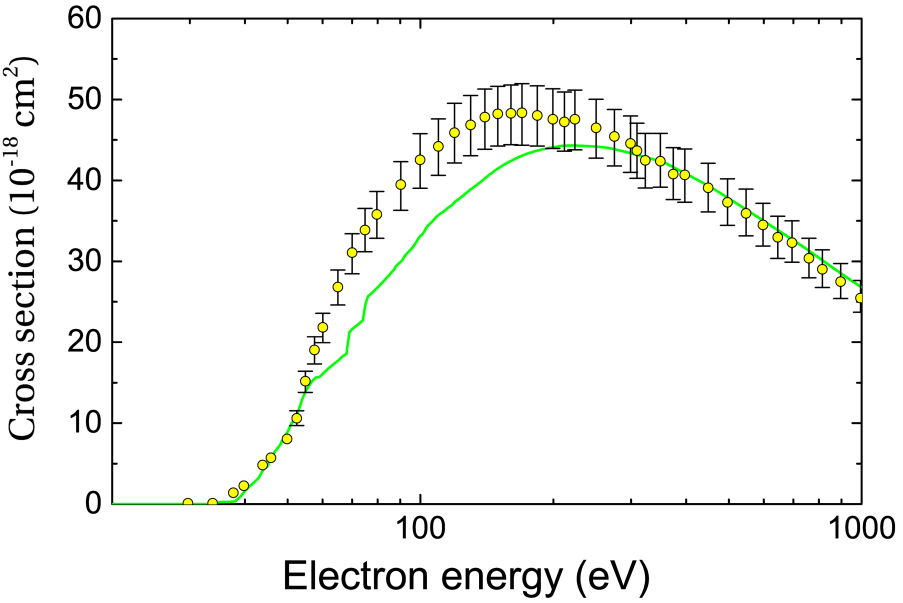

Figure 31: Single ionisation cross sections obtained for the level with index 67 ($J = 13/2$). Experiment: open circles with error bars [14]. Logarithmic scale is used for electron energies.

Influence of Direct Double Ionisation on the Single Ionisation Cross Sections [A3]

The DDI process presented as a sequence of the subsequent ionisation processes means that part of the population for an atomic system, produced in the singly ionised charge state, is transferred to the next charge state. It can be seen from Figure 32 the theoretical single ionisation cross sections for the Se^{3+} ion are below experimental error bars at the lower energies of the incident electron. The study which involves the DI cross sections obtained in the potential of the ionised ion demonstrates good agreement with experiment for this energy range (Figure 32). Unfortunately, both calculations are above the experimental values on the high energy side. This can be explained by the fact that part of the produced Se^{4+} ions manage to reach a higher ionisation stage, for example, due to knocking off of additional electron by the scattered or ejected electrons [97–99]. This process diminishes single ionisation cross sections. The current study does not include a direct double ionisation

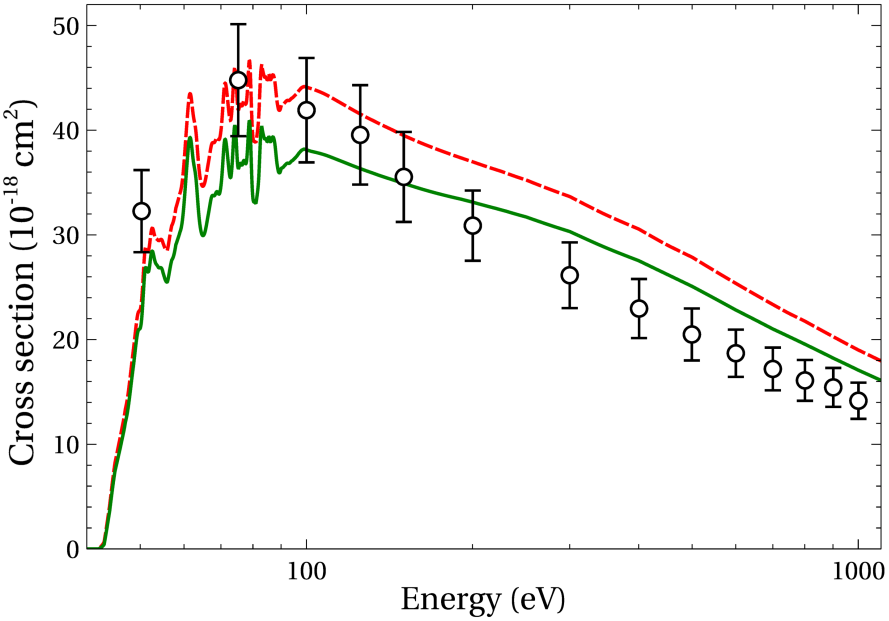

Figure 32: Single ionisation cross sections obtained in the potential of ionised (green solid) and ionizing (red dashed) ion. Experiment: open circles with error bars [14]. Logarithmic scale is used for electron energies.

process when an additional electron is removed from the system due to additional ionisation by the scattered or ejected electrons. In order to approximately estimate this situation, theoretical cross sections for the single ionisation process are subtracted by theoretical ones for the direct double ionisation process, taken from [19] (Figure 33) the values obtained in the potential of the ionised ion. In this case, theoretical cross sections are within the experimental error bars except at 500 eV. The remaining difference among theoretical and experimental values can be explained by the decay of the $3d^9 4s^2 4p$ configuration to the next ionisation stage due to correlation effects.

What is more, the theoretical values for direct double ionisation were obtained for this case when one of the electrons after the first ionisation process takes all the excess energy [19]. Previous studies showed that better agreement with measurements at the higher energies provides a situation when ejected and scattered electrons share equally the excess energy [98]. However, the direct double ionisation process contribution

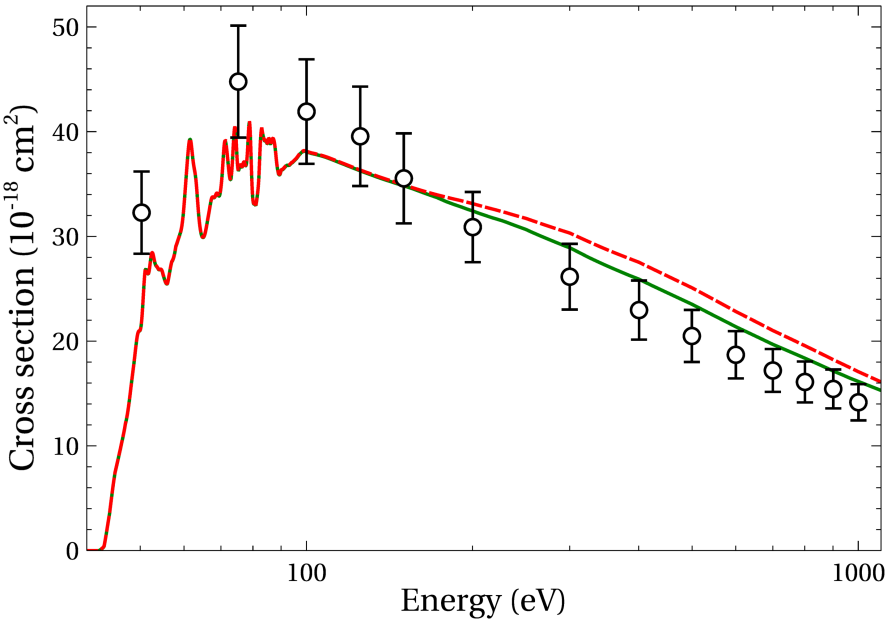

Figure 33: Single ionisation cross sections obtained in the potential of ionised ion (red dashed) with subtracted experimental cross sections from double ionisation process (green solid). Experiment: open circles with error bars [14]. Logarithmic scale is used for electron energies.

to the double ionisation increases by a few times compared to the first scenario. Therefore, in this case, the lower cross sections would be obtained.

The theoretical cross sections are just above experimental error bars at the higher energies when contributing the ionisation-ionisation processes are subtracted. This suggests an idea that the double ionisation of the Se^{3+} ion is mainly determined by the ionisation-ionisation and ionisation-excitation-ionisation processes.

Therefore, it can be concluded that the diminishing contribution from the DDI process is evaluated in the study of the single-ionisation cross sections for the Se^{3+} ion. The single-ionisation cross sections are diminished by $\sim$1 Mb (4 %) at electron energy of 500 eV. This leads to good agreement with measurements starting from 300 eV energy for the single-ionisation cross sections, obtained in the potential of the ionised

ion.

MAIN CONCLUSIONS

Electron-impact single-ionisation cross sections are studied using the DFS approach implemented in the FAC. The direct and indirect ionisation processes are evaluated. The excitation and ionisation by electron impact are investigated in the DW approximation.

1. The study for convergence of the cross sections of the EA channels shows importance of the excitations to the higher-nl shells ($n > 8$, $l > 3$). These excitations are especially pronounced for the tungsten ions with an open $4f$ subshell in the ground configuration.

    1.1. The excitations to the higher shells ($n > 8$) increase the EA cross sections up to ∼60 % for the ground level of the W^{25+} ion. The excitations to the shells with the orbital quantum number $l = 4$ produce ∼40 % of the total EA cross sections. Even the excitations to $l = 5$ contribute ∼7 % to the total EA cross sections.

    1.2. The excitations to the higher shells ($n > 8$) contribute ∼45 % to the total MRC for the levels of the ground configuration of the W^{26+} ion.

    1.3. The contribution of the excitations to the higher shells ($n > 8$) is less important for the W^{5+} ion compared to W^{25+} and W^{26+}. The excitations add ∼15 % of the total cross sections for the ground configuration of the W^{5+} ion.

    1.4. The study demonstrates that the excitations to shells with $n \leqslant 12$ has to be analysed to provide reliable data for the EA cross sections in W^{5+}. The excitations to the higher shells ($n > 12$) produce less than 5 % to the total cross sections.

    1.5. The contribution of the excitations to shells with $n > 8$ for the Fe^{3+} is negligible.

2. The EA MRC for the levels of the ground configuration differs approximately by 60 % for the W^{26+} ion. The EA MRC values for the highest level are ∼40 % higher compared to the excitations from the lowest level of the ground configuration. The excitations to the shells with $9 \leqslant n \leqslant 25$ are less dependent on the initial level. This can be explained by the fact that many important configurations originating from the excitations to the shells with $n \leqslant 8$ have energy levels that straddle the single ionisation threshold.

3. Analysis of the correlation effects for electron-impact ionisation in the W^{5+} and Fe^{3+} ions shows the diminishing effect on the cross sections. The correlation effects reduce the cross sections by ∼20 % at the peak value for the levels of the ground configuration of the W^{5+} ion. The same result is obtained for the levels of the excited $3d^4 4s$ configuration of the Fe^{3+} ion.

4. The scaled DW cross sections are used to explain measurements for the Fe^{3+} ion. The scaling diminishes the DW cross sections by ∼40 % for the levels of the ground and excited $3d^4 4s$ configurations of Fe^{3+}. What is more, the peaks of the cross sections shift to the higher energies by $50 - 100$ eV. The largest effect of scaling is obtained for the lower energies of the impacting electron.

5. Analysis of the single-ionisation cross sections for the Se^{3+} ion demonstrates that the study has to incorporate the diminishing contribution of the DDI process. The single ionisation cross sections are diminished by ∼1 Mb (1×10^{-18}cm^2), by about 4 % at electron energy of 500 eV. This leads to a better agreement with measurements for single-ionisation cross sections of Se^{3+}, starting from 300 eV electron energy.

6. The REDA process plays an important role for single-ionisation cross sections of the Se^{3+} ion at the lower energies of the incident electron. The single-ionisation cross sections are increased up to ∼14 Mb (14×10^{-18}cm^2) at the lower energies. This provides good agreement with measurements for the ground configuration of the Se^{3+} ion.

Bibliography

[1] T. J. M. Boyd and J. J. Sanderson, *The Physics of Plasmas*. Cambridge University Press, 2005.

[2] F. F. Chen, *Introduction to Plasma Physics and Controlled Fusion*. Cham: Springer International Publishing, 2016.

[3] P. M. Bellan, *Fundamentals of Plasma Physics*. Cambridge University Press, 2004.

[4] A. L. Peratt, *Physics of the plasma universe, second edition*. Springer Science+Business Media, 2015.

[5] M. Ossiander, F. Siegrist, V. Shirvanyan, R. Pazourek, A. Sommer, T. Latka, A. Guggenmos, S. Nagele, J. Feist, J. Burgdörfer, R. Kienberger, and M. Schultze, "Attosecond correlation dynamics," *Nature Physics*, vol. 13, no. 3, pp. 280–285, 2017.

[6] K. Hütten, M. Mittermair, S. O. Stock, R. Beerwerth, V. Shirvanyan, J. Riemensberger, A. Duensing, R. Heider, M. S. Wagner, A. Guggenmos, S. Fritzsche, N. Kabachnik, R. Kienberger, and B. Bernhardt, "Ultrafast quantum control of ionization dynamics in krypton," *Nature Communications*, vol. 9, no. 1, p. 719, 2018.

[7] A. Müller, "Electron–ion collisions: Fundamental processes in the focus of applied research," in *Advances in Atomic, Molecular and Optical Physics*, vol. 55, pp. 293–417, 2008.

[8] I. Roederer, "Germanium, arsenic, and selenium abundances in metal-poor stars," *The Astrophysical Journal*, vol. 756, no. 1, p. 36, 2012.

[9] I. U. Roederer, J. J. Cowan, G. W. Preston, S. A. Shectman, C. Sneden, and I. B. Thompson, "Nine new metal-poor stars on the

subgiant and red horizontal branches with high levels of r-process enhancement," *Monthly Notices of the Royal Astronomical Society*, vol. 445, no. 3, pp. 2946–2960, 2014.

[10] N. C. Sterling and H. L. Dinerstein, "The Abundances of Light Neutron-Capture Elements in Planetary Nebulae. II. s -Process Enrichments and Interpretation," *The Astrophysical Journal Supplement Series*, vol. 174, no. 1, pp. 158–201, 2008.

[11] R. D. Blum and P. J. McGregor, "The ionizing stars of the galactic ultra-compact H_{II} region G45.45+0.06," *Astronomical Journal*, vol. 135, no. 5, pp. 1708–1717, 2008.

[12] J. García-Rojas, S. Madonna, V. Luridiana, N. C. Sterling, C. Morisset, G. Delgado-Inglada, and L. Toribio San Cipriano, "s-process enrichment in the planetary nebula NGC 3918. Results from deep echelle spectrophotometry," *Monthly Notices of the Royal Astronomical Society*, vol. 452, no. 3, pp. 2606–2640, 2015.

[13] G. A. Alna'washi, N. B. Aryal, K. K. Baral, D. A. Esteves, A. Aguilar, R. C. Bilodeau, A. Borovik Jr, C. Brandau, J. Jacobi, J. Rausch, A. Becker, K. Spruck, K. Aichele, M. Steidl, U. Hartenfeller, C. M. Thomas, and R. A. Phaneuf, "Electron-impact ionization of Se^{3+}," *Journal of Physics B: Atomic, Molecular and Optical Physics*, vol. 47, no. 47, pp. 105201–7, 2014.

[14] G. A. Alna'washi, N. B. Aryal, K. K. Baral, C. M. Thomas, and R. A. Phaneuf, "Electron-impact ionization of Se^{2+}," *Journal of Physics B: Atomic, Molecular and Optical Physics*, vol. 47, no. 13, p. 135203, 2014.

[15] D. A. Esteves, R. C. Bilodeau, N. C. Sterling, R. A. Phaneuf, A. L. D. Kilcoyne, E. C. Red, and A. Aguilar, "Absolute high-resolution Se^{+} photoionization cross-section measurements with Rydberg-series analysis," *Physical Review A*, vol. 84, no. 1, p. 013406, 2011.

[16] N. C. Sterling, D. A. Esteves, R. C. Bilodeau, A. L. D. Kilcoyne, E. C. Red, R. A. Phaneuf, and A. Aguilar, "Experimental photoionization cross-section measurements in the ground and metastable state threshold region of Se^{+}," *Journal of Physics B: Atomic, Molecular and Optical Physics*, vol. 44, no. 2, p. 025701, 2011.

[17] D. A. Esteves, A. Aguilar, R. C. Bilodeau, R. A. Phaneuf, A. L. D. Kilcoyne, E. C. Red, and N. C. Sterling, "Absolute single photoionization cross-section measurements of Se^{3+} and Se^{5+}," *Journal of Physics B: Atomic, Molecular and Optical Physics*, vol. 45, no. 11, p. 115201, 2012.

[18] D. A. Macaluso, A. Aguilar, A. L. D. Kilcoyne, E. C. Red, R. C. Bilodeau, R. A. Phaneuf, N. C. Sterling, and B. M. McLaughlin, "Absolute single-photoionization cross sections of Se^{2+}: Experiment and theory," *Physical Review A*, vol. 92, no. 6, p. 063424, 2015.

[19] M. S. Pindzola and S. D. Loch, "Electron-impact ionization of Se^{2+} and Se^{3+}," *Journal of Physics B: Atomic, Molecular and Optical Physics*, vol. 49, no. 12, 2016.

[20] L. Liu, P. Liu, and J. Zeng, "Electron impact ionization cross sections of the ground and excited levels of Se^{3+}," *Journal of Electron Spectroscopy and Related Phenomena*, vol. 209, pp. 9–13, 2016.

[21] J. Koncevičiutė, S. Kučas, Š. Masys, A. Kynienė, and V. Jonauskas, "Electron-impact triple ionization of Se^{2+}," *Physical Review A*, vol. 97, no. 1, pp. 1–6, 2018.

[22] J. Koncevičiutė, S. Kučas, A. Kynienė, Š. Masys, and V. Jonauskas, "Electron-impact double and triple ionization of Se^{3+}," *Journal of Physics B: Atomic, Molecular and Optical Physics*, vol. 52, no. 2, p. 025203, 2019.

[23] D. C. Griffin, C. Bottcher, and M. S. Pindzola, "Theoretical calculations of the contributions of excitation autoionization to electron-impact ionization in ions of the transition series of elements," *Physical Review A*, vol. 25, no. 3, pp. 1374–1382, 1982.

[24] A. Müller, K. Tinschert, C. Achenbach, E. Salzborn, and R. Becker, "A new technique for the measurement of ionization cross sections with crossed electron and ion beams," *Nuclear Inst. and Methods in Physics Research, B*, vol. 10-11, pp. 204–206, 1985.

[25] M. S. Pindzola, D. C. Griffin, C. Bottcher, S. M. Younger, and H. T. Hunter, "Electron impact ionization data for the iron isonuclear sequence," *Nuclear Fusion*, vol. 27, pp. 21–41, 1987.

[26] R. Montague and M. Harrison, "A measurement of the cross section for electron impact ionisation of singly charged tungsten ions," *Journal of Physics B: Atomic and Molecular Physics*, vol. 17, no. 13, pp. 2707–2711, 1984.

[27] R. Neu, *Tungsten as a Plasma-Facing Material in Fusion Devices*. PhD thesis, Max-Planck-Institut fur Plasmaphysik, 2003.

[28] V. Jonauskas, G. Gaigalas, and S. Kučas, "Relativistic calculations for M1-type transitions in 4dN configurations of W^{29+}-W^{37+} ions," *Atomic Data and Nuclear Data Tables*, vol. 98, no. 1, pp. 19–42, 2012.

[29] A. Müller, "Fusion-Related Ionization and Recombination Data for Tungsten Ions in Low to Moderately High Charge States," *Atoms*, vol. 3, no. 2, pp. 120–161, 2015.

[30] M. Stenke, K. Aichele, D. Harthiramani, G. Hofmann, M. Steidl, R. Völpel, and E. Salzborn, "Electron-impact single-ionization of singly and multiply charged tungsten ions," *Journal of Physics B: Atomic, Molecular and Optical Physics*, vol. 28, no. 13, pp. 2711–2721, 1995.

[31] W. Lotz, "Electron-impact ionization cross-sections and ionization rate coefficients for atoms and ions from hydrogen to calcium," *Zeitschrift für Physik*, vol. 216, no. 3, pp. 241–247, 1968.

[32] M. S. Pindzola and D. C. Griffin, "Electron-impact ionization of tungsten ions in the configuration-average distorted-wave approximation," *Physical Review A*, vol. 56, no. 2, pp. 1654–1657, 1997.

[33] A. V. Demura, M. B. Kadomtsev, V. S. Lisitsa, and V. A. Shurygin, "Electron impact ionization of tungsten ions in a statistical model," *JETP Letters*, vol. 101, no. 2, pp. 85–88, 2015.

[34] D. Zhang, L. Xie, J. Jiang, Z. Wu, C. Dong, Y. Shi, and Y. Qu, "Electron-impact single ionization for W^{4+} and W^{5+}," *Chinese Physics B*, vol. 27, no. 5, 2018.

[35] Y. K. Kim and M. E. Rudd, "Binary-encounter-dipole model for electron-impact ionization," *Physical Review A*, vol. 50, no. 5, pp. 3954–3967, 1994.

[36] Y. K. Kim, "Scaling of plane-wave Born cross sections for electron-impact excitation of neutral atoms," *Physical Review A*, vol. 64, no. 3, p. 10, 2001.

[37] Y. K. Kim and P. M. Stone, "Ionization of boron, aluminum, gallium, and indium by electron impact," *Physical Review A*, vol. 64, no. 5, p. 11, 2001.

[38] Y. K. Kim and J. Desclaux, "Ionization of carbon, nitrogen, and oxygen by electron impact," *Physical Review A*, vol. 66, no. 1, pp. 127081–1270812, 2002.

[39] D. H. Kwon, Y. J. Rhee, and Y. K. Kim, "Ionization of W and W^+ by electron impact," *International Journal of Mass Spectrometry*, vol. 252, no. 3, pp. 213–221, 2006.

[40] L. Vainshtein, I. Beigman, P. Mertens, S. Brezinsek, A. Pospieszczyk, and D. Borodin, "Ionization of W atoms and W^+ ions by electrons," *Journal of Physics B: Atomic, Molecular and Optical Physics*, vol. 44, no. 12, 2011.

[41] D. Kwon, Y. Cho, and Y. Lee, "Electron-impact ionization of W^+ forming W^{2+}," *International Journal of Mass Spectrometry*, vol. 356, pp. 7–13, 2013.

[42] M. Gu, "The flexible atomic code," *Canadian Journal of Physics*, vol. 86, no. 5, pp. 675–689, 2008.

[43] C. Ballance, S. D. Loch, M. S. Pindzola, and D. C. Griffin, "Electron-impact excitation and ionization of W^{3+} for the determination of tungsten influx in a fusion plasma," *Journal of Physics B: Atomic, Molecular and Optical Physics*, vol. 46, no. 5, p. 055202, 2013.

[44] D. H. Sampson, H. L. Zhang, A. K. Mohanty, and R. E. Clark, "A Dirac-Fock-Slater approach to atomic structure for highly charged ions," *Physical Review A*, vol. 40, no. 2, pp. 604–615, 1989.

[45] I. P. Grant, B. J. McKenzie, P. H. Norrington, D. F. Mayers, and N. C. Pyper, "An atomic multiconfigurational Dirac-Fock package," *Computer Physics Communications*, vol. 21, no. 2, pp. 207–231, 1980.

[46] J. C. Slater, "A simplification of the Hartree-Fock method," *Physical Review*, 1951.

[47] A. K. Pradhan and S. N. Nahar, "Atomic Spectroscopy and Astrophysics," *Physics Today*, vol. 41, no. 8, pp. 38–45, 1988.

[48] R. Karazija, *Introduction to the Theory of X-Ray and Electronic Spectra of Free Atoms*. Springer Science+Business Media, 1996.

[49] H. S. Massey and C. B. Mohr, "The collision of slow electrons with atoms. II.—General theory and inelastic collisions," *Proceedings of the Royal Society of London. Series A, Containing Papers of a Mathematical and Physical Character*, vol. 139, no. 837, pp. 187–201, 1933.

[50] D. H. Madison and W. N. Shelton, "Distorted-wave approximation and its application to the differential and integrated cross sections for electron-impact excitation of the 2P1 state of helium," *Physical Review A*, vol. 7, no. 2, pp. 499–513, 1973.

[51] K. Aichele, U. Hartenfeller, D. Hathiramani, G. Hofmann, F. Melchert, V. Schäfer, M. Steidl, M. Stenke, R. Völpel, and E. Salzborn, "Electron impact ionization of the hydrogen-like ions: B^{4+}, C^{5+}, N^{6+} and O^{7+}," *Physica Scripta T*, vol. 73, pp. 125–126, 1997.

[52] M. Hahn, A. Müller, and D. W. Savin, "Electron-impact Multiple-ionization Cross Sections for Atoms and Ions of Helium through Zinc," *The Astrophysical Journal*, vol. 850, no. 2, p. 122, 2017.

[53] V. Jonauskas, "Electron-impact double ionization of the carbon atom," *Astronomy and Astrophysics*, vol. 620, pp. 4–9, 2018.

[54] H. Yoshizumi, *Advances in Chemical Physics*, vol. II of *Advances in Chemical Physics*. Hoboken, NJ, USA: John Wiley and Sons, Inc., 1958.

[55] R. Karazija and S. Kučas, "Average characteristics of the configuration interaction in atoms and their applications," *Journal of Quantitative Spectroscopy and Radiative Transfer*, vol. 129, no. 6, pp. 131–144, 2013.

[56] D. Zhang and D. H. Kwon, "Theoretical electron-impact ionization of W^{17+} forming W^{18+}," *Journal of Physics B: Atomic, Molecular and Optical Physics*, vol. 47, no. 7, 2014.

[57] A. Kynienė, G. Merkelis, A. Šukys, Š. Masys, S. Pakalka, R. Kisielius, and V. Jonauskas, "Maxwellian rate coefficients for electron-impact ionization of W^{26+}," *Journal of Physics B: Atomic, Molecular and Optical Physics*, vol. 51, no. 15, p. 155202, 2018.

[58] A. Kynienė, Š. Masys, and V. Jonauskas, "Influence of excitations to high-*nl* shells for the ionization process in the W^{26+} ion," *Physical Review A*, vol. 91, no. 6, p. 062707, 2015.

[59] V. Jonauskas, A. Kynienė, G. Merkelis, G. Gaigalas, R. Kisielius, S. Kučas, Š. Masys, L. Radžiūtė, and P. Rynkun, "Contribution of high- nl shells to electron-impact ionization processes," *Physical Review A*, vol. 91, no. 1, p. 012715, 2015.

[60] M. S. Pindzola and S. D. Loch, "Electron-impact ionization of W^{27+}," *Physical Review A*, vol. 93, no. 6, pp. 1–5, 2016.

[61] "Controlled Fusion Atomic Data Center." [Online:]. Available: https://www.phy.ornl.gov/groups/atomic/atomic.html, 2018.

[62] A. E. Kramida and J. Reader, "Ionization energies of tungsten ions: W^{2+} through W^{71+}," *Atomic Data and Nuclear Data Tables*, vol. 92, no. 4, pp. 457–479, 2006.

[63] A. Kynienė, Š. Masys, and V. Jonauskas, "Influence of excitations to high-*nl* shells for the ionization process in the W^{26+} ion," *Physical Review A*, vol. 91, no. 6, p. 062707, 2015.

[64] D. Zhang and D. H. Kwon, "Theoretical electron-impact ionization of W^{17+} forming W^{18+}," *Journal of Physics B: Atomic, Molecular and Optical Physics*, vol. 47, no. 7, 2014.

[65] S. Loch, J. Ludlow, M. Pindzola, A. Whiteford, and D. Griffin, "Electron-impact ionization of atomic ions in the W isonuclear sequence," *Phys. Rev. A*, vol. 72, no. 5, p. 052716, 2005.

[66] P. Jönsson, G. Gaigalas, J. Bieroń, C. Froese Fischer, and I. Grant, "New version: Grasp2k relativistic atomic structure package," *Computer Physics Communications*, vol. 184, no. 9, pp. 2197 – 2203, 2013.

[67] V. Jonauskas, A. Kynienė, P. Rynkun, S. Kučas, G. Gaigalas, R. Kisielius, Š. Masys, G. Merkelis, and L. Radžiūtė, "Theoretical investigation of spectroscopic properties of W^{26+} in EBIT plasma," *Journal of Physics B: Atomic, Molecular and Optical Physics*, vol. 48, no. 13, p. 135003, 2015.

[68] S. Kučas, V. Jonauskas, and R. Karazija, "Global characteristics of atomic spectra and their use for the analysis of spectra. IV. Configuration interaction effects," *Physica Scripta*, vol. 55, no. 6, pp. 667–675, 1997.

[69] V. Jonauskas, R. Karazija, and S. Kučas, "The essential role of many-electron Auger transitions in the cascades following the photoionization of 3p and 3d shells of Kr," *Journal of Physics B: Atomic, Molecular and Optical Physics*, vol. 41, no. 21, 2008.

[70] V. Jonauskas, S. Kučas, and R. Karazija, "Auger decay of 3p-ionized krypton," *Physical Review A*, vol. 84, no. 5, 2011.

[71] A. Borovik, B. Ebinger, D. Schury, S. Schippers, and A. Müller, "Electron-impact single ionization of W^{19+} ions," *Phys. Rev. A*, vol. 93, p. 012708, 2016.

[72] A. Kynienė, S. Pakalka, Š. Masys, and V. Jonauskas, "Electron-impact ionization of W^{25+}," *Journal of Physics B: Atomic, Molecular and Optical Physics*, vol. 49, no. 18, p. 185001, 2016.

[73] R. Cowan, *The theory of atomic structure and spectra.* 1981.

[74] V. Jonauskas, A. Kynienė, S. Kučas, S. Pakalka, Š. Masys, A. Prancikevičius, A. Borovik, M. F. Gharaibeh, S. Schippers, and A. Müller, "Electron-impact ionization of W^{5+}," *Physical Review A*, vol. 100, no. 6, pp. 1–12, 2019.

[75] V. Jonauskas, R. Karazija, and S. Kučas, "Theoretical investigation of the Auger and photoion-yield spectra resulting from 3d photoionization or 3d→4f excitation of atomic Eu," *Journal of Electron*

Spectroscopy and Related Phenomena, vol. 107, no. 2, pp. 147–154, 2000.

[76] V. Jonauskas, L. Partanen, S. Kučas, R. Karazija, M. Huttula, S. Aksela, and H. Aksela, "Auger cascade satellites following 3d ionization in xenon," *Journal of Physics B: Atomic, Molecular and Optical Physics*, vol. 36, no. 22, pp. 4403–4416, 2003.

[77] M. S. Pindzola and S. D. Loch, "Electron-impact single and double ionization of the Fe atom and Fe^{q+} (q=1–4) atomic ions," *Journal of Physics B: Atomic, Molecular and Optical Physics*, vol. 51, no. 1, p. 015202, 2018.

[78] M. Stenke, U. Hartenfeller, K. Aichele, D. Hathiramani, M. Steidl, and E. Salzborn, "Electron impact double ionization of multiply charged iron ions," *Journal of Physics B: Atomic, Molecular and Optical Physics*, vol. 32, pp. 3641–3649, 1999.

[79] K. P. Dere, "Ionization rate coefficients for the elements hydrogen through zinc," *Astronomy and Astrophysics*, vol. 466, no. 2, pp. 771–792, 2007.

[80] D. C. Griffin, C. Bottcher, and M. S. Pindzola, "Theoretical calculations of the contributions of excitation autoionization to electron-impact ionizatino in ions of the transitin series of elements," *Physical Review A*, vol. 25, no. 3, 1982.

[81] M. S. Pindzola, D. C. Griffin, C. Bottcher, S. M. Younger, and H. T. Hunter, "Electron impact ionization data for the iron isonuclear sequence," *Nuclear Fusion*, vol. 27, pp. 21–41, 1987.

[82] A. Kramida, Y. , J. Reader, and NIST ASD Team, "NIST atomic spectra database," 2019.

[83] A. Borovik, C. Brandau, J. Jacobi, S. Schippers, and A. Müller, "Electron-impact single ionization of Xe^{10+} ions," *Journal of Physics B: Atomic, Molecular and Optical Physics*, vol. 44, no. 20, p. 205205, 2011.

[84] R. Karazija and S. Kučas, "Average characteristics of the configuration interaction in atoms and their applications," *Journal of*

Quantitative Spectroscopy and Radiative Transfer, vol. 129, pp. 131–144, 2013.

[85] A. Kynienė, V. Jonauskas, S. Kučas, and R. Karazija, "On the existence of dipole satellites in the region of $M_{2,3}$-$L_{2,3}$ non-dipole emission lines for transition elements ," *Lithuanian Journal of Physics*, vol. 48, p. 219, 2008.

[86] V. Jonauskas, R. Kisielius, A. Kynienė, S. Kučas, and P. H. Norrington, "Magnetic dipole transitions in $4d^N$ configurations of tungsten ions," *Physical Review A*, vol. 81, no. 1, pp. 1–9, 2010.

[87] J. Palaudoux, P. Lablanquie, L. Andric, K. Ito, E. Shigemasa, J. H. Eland, V. Jonauskas, S. Kučas, R. Karazija, and F. Penent, "Multielectron spectroscopy: Auger decays of the krypton 3d hole," *Physical Review A*, vol. 82, no. 4, 2010.

[88] K. Spruck, N. R. Badnell, C. Krantz, O. Novotný, A. Becker, D. Bernhardt, M. Grieser, M. Hahn, R. Repnow, D. W. Savin, A. Wolf, A. Müller, and S. Schippers, "Recombination of W^{18+} ions with electrons: Absolute rate coefficients from a storage-ring experiment and from theoretical calculations," *Physical Review A*, vol. 90, no. 3, p. 032715, 2014.

[89] N. R. Badnell, K. Spruck, C. Krantz, O. Novotný, A. Becker, D. Bernhardt, M. Grieser, M. Hahn, R. Repnow, D. W. Savin, A. Wolf, A. Müller, and S. Schippers, "Recombination of W^{19+} ions with electrons: Absolute rate coefficients from a storage-ring experiment and from theoretical calculations," *Physical Review A*, vol. 93, no. 5, pp. 1–6, 2016.

[90] M. Lestinsky, N. R. Badnell, D. Bernhardt, D. Bing, M. Grieser, M. Hahn, J. Hoffmann, B. Jordon-Thaden, C. Krantz, O. Novotný, D. A. Orlov, R. Repnow, A. Shornikov, A. Müller, S. Schippers, A. Wolf, and D. W. Savin, "Electron-ion recombination of Mg^{6+} forming Mg^{5+} and of Mg^{7+} forming Mg^{6+}: Laboratory measurements and theoretical calculations," *Astrophysical Journal*, vol. 758, no. 1, 2012.

[91] A. Müller, S. Schippers, J. Hellhund, A. L. Kilcoyne, R. A. Phaneuf, and B. M. Mclaughlin, "Photoionization of tungsten ions: Experiment

and theory for W^{5+}," *Journal of Physics B: Atomic, Molecular and Optical Physics*, vol. 52, no. 19, 2019.

[92] S. P. Preval, N. R. Badnell, and M. G. O'Mullane, "Dielectronic recombination of lanthanide and low ionization state tungsten ions: W^{13+} -W^{1+}," *Journal of Physics B: Atomic, Molecular and Optical Physics*, vol. 52, no. 2, 2019.

[93] T. R. Kallman and P. Palmeri, "Atomic data for x-ray astrophysics," *Reviews of Modern Physics*, vol. 79, no. 1, pp. 79–133, 2007.

[94] A. Kramida, Y. Ralchenko, J. Reader, and NIST ASD Team. NIST Atomic Spectra Database (ver. 5.8), [Online]. Available: https://physics.nist.gov/asd [2021, January 2021].National Institute of Standards and Technology, Gaithersburg, MD., 2021.

[95] A. Borovik Jr, M. F. Gharaibeh, S. Schippers, and A. Müller, "Plasma rate coefficients for electron-impact ionization of Xe^{q+} ions (q = 8, . . . , 17)," *Journal of Physics B: Atomic, Molecular and Optical Physics*, vol. 48, no. 3, p. 035203, 2015.

[96] D. H. Kwon, Y. J. Rhee, and Y. K. Kim, "Cross sections for ionization of Mo and Mo^+ by electron impact," *International Journal of Mass Spectrometry*, vol. 245, no. 1-3, pp. 26–35, 2005.

[97] M. Gryziński, "Classical theory of atomic collisions. I. Theory of inelastic collisions," *Physical Review*, vol. 138, no. 2A, 1965.

[98] V. Jonauskas, A. Prancikevičius, Š. Masys, and A. Kynienė, "Electron-impact direct double ionization as a sequence of processes," *Physical Review A*, vol. 89, no. 5, pp. 1–5, 2014.

[99] J. Koncevičiutė and V. Jonauskas, "Electron-impact double ionization of Li^+," *Physical Review A*, vol. 93, no. 2, pp. 1–5, 2016.

ADDENDUM

Cross Section Calculation Workflow

This section overviews steps that are required to get results similar to the ones in this thesis.

The package used in my study to calculate energy levels, radiative and Auger transition probabilities, electron impact excitation and ionisation cross sections is Flexible Atomic Code (FAC). It is available at GitHub.com[1].

The direct and indirect ionisation processes are studied to calculate the single ionisation cross sections. The direct ionisation cross sections are calculated from the single ionisation threshold up to the $\sim 10^5$ eV. The cross sections for the initial and final states are calculated at ~ 20 energy points. Thus, the cross sections are summed up over the final states to obtain the cross sections corresponding to the initial state. The same procedure is repeated for the excitation cross sections. However, there are many more excited states to be investigated. For example, the number of the excited states reached $\sim 10^7$ for the W^{25+} ion. Furthermore, all radiative and Auger transitions are calculated from the excited states above the single ionisation threshold. For the W^{25+}, the number of the radiative and Auger transitions amounts to $\sim 10^9$. These calculations are divided to decrease the calculation time.

The number of such transitions is especially large for (W^{25+}, W^{26+}) tungsten ions with an open $4f$ subshell. What is more, the extended basis of interacting configurations used in the study of the ionisation process in the W^{5+} ion requires dealing with an even larger number of transitions.

[1] https://github.com/flexible-atomic-code/fac

The lifetimes of the excited states are determined and branching ratios calculated. In addition, the REDA study requires estimating the cross sections for the electron capture. The branching ratios are calculated for the energy levels of the produced ion with the captured electron and initial ion that decay further leading to a single ionisation process. What is more, the number of energy levels increases even more in this case, since the capture of the initial electron can produce configurations with up to four open subshells.

Since we have to deal with a large number of states there were developed programs using C, SQL, Python programming languages to calculate lifetimes and branching ratios of the excited levels. Those programs also allowed us to utilize effectively computation resources and to monitor the whole calculations process with verification of the output files. We used HPC servers that were located at the Institute of Theoretical Physics and Astronomy. Part of the calculations was performed using resources of the High Performance Computing Center "HPC Sauletekis" in Vilnius University Faculty of Physics.

For some ions, the solution to use MySQL[2] database with developed stored procedures was enough to complete calculations. We used available hardware, a single HPC server (64 CPU threads, 768 GB RAM, 5 TB storage). FAC output files were loaded as tables into the database and calculations were made. The whole calculation process was split into batches and managed by stored procedures, which submitted new work based on server load. Logging was implemented to trace errors or skipped calculation tasks.

As W^{5+} study has to deal with the huge number of transitions, Apache Hadoop[3] cluster with two nodes was set up (total available resources: 72 CPU threads, 596GB RAM, 64TB storage). Apache Spark[4] was used as a computation engine to process this kind of data. Key features of this computation engine are that it tends to optimize calculations and data file reading operations. Also, data is partitioned into pieces of the specified size and this feature also improves computational performance. We used Python language to program processing of FAC output files and providing radiative and Auger transitions, branching ratios and EA cross

[2]https://www.mysql.com/
[3]https://hadoop.apache.org/
[4]https://spark.apache.org/

section calculation results by the same calculation run.

After all calculations are completed, modelling and scientific analysis tasks led to the results that were presented in this thesis.

Vilnius University Press
9 Saulėtekio Ave., Building III, LT-10222 Vilnius
Email: info@leidykla.vu.lt, www.leidykla.vu.lt
Print run copies 15